Foreword

This thesis has been prepared in fulfilment of the requirements for a Ph.D. at the University of Sultan Moulay Slimane, Beni Mellal, Morocco, under the supervision of Professor Dr. Khalil El-Hami.

Dedication

I dedicate my dissertation Work

To my family,

to my friends

And to all the hard working and respected teachers

Prof. Dr. Khalil El-Hami

Acknowledgements

I would like to thank my university supervisor, Dr. Khalil El-Hami, for supporting me at every point along the way, including reading over all my work and providing valuable insight and feedback, and sharing his academic experiences. I would like to thank him for sharing his knowledge, and for always being positive and showing interest to my work.

I thank the members of the Jury for agreeing to judge my work,

I also thank all the members of the Laboratory and in particular the doctoral students M. Eddya, Z. Kbiri, B. Tbib, H. Belbsiri, and A. Abouharim for their help.

I also would like to thank the entire educational team of Hassan 1 University, in particular the manager of the characterization center. And also like to thank the entire educational team of Sultan Moulay Slimane University, in particular the manager of the characterization center.

I also want to thank my friend Y. Lahyani who helped me to correct the spelling mistakes.

I thank my wife M. Addali, for the patience and the support she showed during all the duration of this thesis and all my family especially my parents.

I would like to express my gratitude to all the researchers and specialists, too numerous to mention, who took the time to discuss my subject. Each of these discussions helped me to advance my analysis.

General introduction

Nanoparticles today represent a major technological and economic challenge. They allow very promising innovations in many fundamental areas such as: health, energy or industry.

In this work we are interested in the potential contribution of nanoparticles in the field of heat transfers. A more systematic use of inexhaustible sources of energy (solar, wind, geothermal..) Is not sufficient to meet the energy challenge of the future generations. All solutions must be explored namely the path of energy savings which is an important contribution to be developed.

Heat transfer, which is very common in the industrial and technological world (engine coolant, lubricating oils, coolants for solar panels and heat exchangers,) Often uses liquids that do not conduct much heat (table 0.1). Metals for their part have the greatest thermal conductivities available but do not allow easy thermal contacts.

Table 0. 1:Thermal conductivities λ of some common materials (ambient temperature)

Liquids conductivity (λ (W/m°K))		Metals conductivity (λ (W/m°K))			
Water	Glycerol	Iron	Cooper	Silver	CNT
0,56	0,29	80	400	450	2500

One possible answer to the question of improving heat transfer is to use both the flow properties of liquids and the high thermal conductivity of solid metals. The use of nanofluids based on metallic particles or carbon nanotubes is certainly the most promising solution in this direction. It was Choi who first introduced the concept of nanofluid in 1995, a stable suspension in liquid of nanoparticles smaller than 200 nm.

Since 1995 many studies have been carried out on various nanofluids, among which Al_2O_3/Water, CuO/water and CNT/water are the most frequently encountered.

Unfortunately, this multitude of studies is also accompanied by a multiple contradictory result both at the experimental and theoretical level. This wide dispersion of results shows that the nature of the nanofluid and its method of synthesis are of the utmost importance. We have therefore tried to

identify some key physical parameters allowing to better describe or better predict the results obtained or expected.

One of the first physical parameters to consider is the size of the nanoparticles used. Thus, the copper or silver nanoparticles currently sold on the market have a large dispersion of sizes and morphologies within the same batch, as shown in Figure 1.

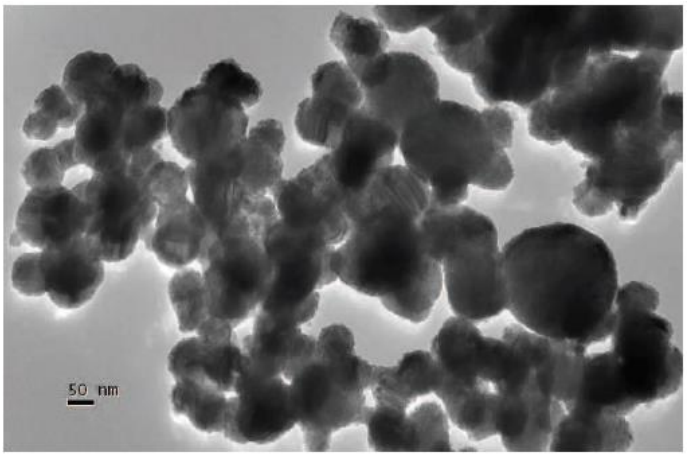

Figure 1:Cuprite nanoparticles with a mean radius of 150 nm, purchased from Aldrich.

The commercial batches do not allow a precise study of the influence of the size and the morphology of the nanoparticles on the macroscopic physical properties of the nanofluids.

We therefore sought to synthesize ourselves metal nanoparticles of given sizes and morphologies.

For this, we used and improved the method of synthesis by microwave irradiation, the presentation which is the subject of the chapter II after starting with a bibliographic study of nanoparticles synthesis methods introduced in chapter I.

This work focuses mainly on the study of the real effects of concentration of silver nanoparticles on the thermal and rheological properties of nanofluids. The study of the rheological properties of nanofluids is the subject of the chapter IV.

The study of the thermal properties of nanofluids generate a delicate problem of the influence of convection on the determination of the effective thermal conductivity of the liquid. In order to determine the real properties of the system, we adapted to the case of liquids the hot wire thermal characterization method frequently used with insulating solids. This method has the advantage of allowing sufficiently weak thermal excitations to make the influence of convection almost

negligible. The detailed description of this method and the evaluation of its main limitations are presented in Chapter III.

The study of the thermal conductivity of nanofluids is presented in same chapter. The remarkable values obtained for the Silver/Glycerol nanofluid show the harmful influence of the interfacial thermal resistance that can be introduced by the surface treatment of nanoparticles or chemical additives. We suggested in this part a simple model which allows us to take this influence into account.

In this work we also dedicate a part for the simulation (Chapter VI), in which we take advantage of programming one of the properties of silver nanoparticles namely surface plasmon resonance (SPR) using the FDTD method, and also the programming of the method of hot wire for determining the thermal conductivity of liquids.

Teflon and doped Teflon have been studied to measure optical and electrical quantities. Various concentrations of Erbium (Er) gave a change in these properties such as gap energy, Urbach energy and micro-strain. Comparison of the absorbance and adjusted absorbance of Teflon and doped Teflon suggests that the extrinsic absorbers may represent a slight increase in absorbance over what the intrinsic absorbance of the Teflon polymer might be. X-ray diffraction line broadening analysis was used to measure Teflon and doped Teflon microstructure parameters. FT-IR spectroscopy is a powerful tool for the analysis of polymers, and the determination of the stability of our material.

Teflon and doped Teflon have been studied to investigate the effect of gadolinium (Gd) on micro-morphology. X-ray diffraction line broadening analysis was used to measure Teflon and doped Teflon microstructure parameters discussed in Chapters VII.

Résumé de la thèse de doctorat

Les matériaux de taille très fine (nanoparticules métalliques ou oxydes métalliques) interviennent pour améliorer quelques propriétés physiques des matériaux, comme la diminution de l'énergie de gap optique. D'autre part, les lubrifiants à base de Glycérol remplaceront progressivement les matériaux lubrifiants à base d'huile dans certaines applications spécifiques à savoir, les fluides caloporteurs, les fluides hydrauliques. L'avantage de ces lubrifiants à base de Glycérol c'est qu'ils disposent d'excellentes propriétés telle que, la rapidité des suspensions des nanoparticules, l'amélioration de la conductivité thermique.

Dans ce contexte, les travaux de cette thèse, réalisés à l'Université de Sultan Molay Slimane, Laboratoire des Nanosciences et Modélisation (LNM) Faculté Polydisciplinaire de Khouribga (FPK) sous la direction de Professeur Dr Khalil EL-HAMI où l'objectif de l'étude est de proposer des matériaux innovants : Nano-composites à base des nanoparticules d'Argent / Glycérol pour les nano fluides potentiellement intéressants en termes d'amélioration de la conductivité thermique et électrique, et Nano-composites à base des nanoparticules (d'Erbium et de Gadolinium) /PTFE, pour les semi-conducteurs dans les applications industrielles.

Pour cela, nous avons utilisé et amélioré la méthode de synthèse par irradiation micro-ondes et qui fait l'objet du chapitre II. Mais avant l'introduction nous avons commencé par une étude bibliographique des méthodes de synthèse des nanoparticules (Chapitre I).

Dans les chapitres III et IV nous avons étudié les effets réels de la concentration des nanoparticules d'Argent sur les propriétés thermiques et rhéologiques des nanofluides (Argent/Glycérol).

L'étude des propriétés thermiques des nano fluides pose un problème délicat de l'influence de la convection sur la détermination de la conductivité thermique effective du liquide. Afin de déterminer les propriétés réelles du système, nous avons adapté dans le cas des liquides la méthode de caractérisation thermique au fil chaud fréquemment utilisée avec les solides isolants. Cette méthode a l'avantage de permettre des excitations thermiques suffisamment faibles pour rendre l'influence de la convection presque négligeable. La description détaillée de cette méthode et l'évaluation de ses principales limites sont présentées dans le chapitre III.

Dans ce travail, nous dédions également une partie pour la simulation (Chapitre V), dans laquelle nous profitons de la programmation d'une des propriétés des nanoparticules d'argent à savoir la

résonance plasmonique de surface (SPR) en utilisant la méthode FDTD, ainsi que la programmation de la méthode de fil chaud pour déterminer la conductivité thermique des liquides.

Le Téflon et le Téflon dopé ont été étudiés pour mesurer les grandeurs optiques et électriques. Le dopage du Téflon par diverses concentrations d'Erbium (Er) a donné un changement dans ces propriétés, telle que l'énergie de gap, l'énergie d'Urbach et la microdéformation. L'analyse par diffraction des rayons X (RDX) est utilisée pour mesurer les paramètres de microstructure du Téflon et du Téflon dopé. La spectroscopie FT-IR est un outil puissant pour l'analyse des polymères, et la détermination de la stabilité de notre matériau (Chapitre VI).

Dans le dernier chapitre nous avons étudié l'effet du Gadolinium (Gd) sur la micromorphologie du Téflon en la comparant avec l'effet de l'Erbium (Er) sur le Téflon.

Table of contents

List of figures

List of tables

CHAPTER I :

OVERVIEW ON NANOFLUIDS AND POLYTETRAFLUOROETHYLEN (PTFE)

INTRODUCTION

In this chapter we focused on some bibliography of our study namely the physical properties, thermophysical properties of Nano fluids from the synthesis of nanoparticles to the synthesis of fluids containing these nanoparticles, study of electrical conductivity, thermal conductivity and the viscosity. Also some optical and electrical properties of Teflon in the context of helping the doping of this material by transition elements at the nanometric scale also some application of this material. Then a little research on the notion of energy bands of some polymers because these polymers are similar to our basic material which is Teflon.

We also represented the techniques of characterization of materials namely (XRD, FT-IR, SEM, TEM) for the morphology of our materials and UV-visible the study of gap energy also the methods of thermal characterization and rheological.

We will end this chapter with a look at the FDTD simulation method for surface plasmon (SPR) and the THW method simulation for the thermal conductivity of fluids.

1. Generality on nanofluids

1. 1. Definition

Nanofluids are dispersions of nanoscale particles (typically less than 100 nm in diameter), called nanoparticles, in a base fluid to improve certain properties. This type of solution has aroused great interest since the discovery of their particular thermal properties. In the case of heat transfer fluids, one of the first parameters to take into account in order to assess the heat exchange potential is thermal conductivity. Indeed, the base fluids often used in cooling or heating applications have very low thermal conductivities which limit their heat transfer capacity. The idea is then to insert very high conductivity nanoparticles into the base liquids, in order to increase the effective thermal conductivity of the mixture and thus improve its thermal performance.

1. 2. Nanoparticles and carrier fluids

The nanoparticle is an assembly of a few hundred to a few thousand atoms, resulting in an object of which at least one of the dimensions is of nanometric size (1 to 100 nm). Nanoparticles are located at the border between the microscopic scale and the atomic or molecular scale. They have a fundamental interest, and are very studied nowadays. Many physicists and chemists synthesize them, other physicists study them in order to understand the physics of these nanometric objects and biologists use them as cell markers.

The base liquids generally used in the preparation of nanofluids are those commonly used in heat transfer applications such as water, ethylene glycol, motor oil etc ...; Nanoparticles can be based on metals, oxides, carbides, nitrides or carbon.

Table I.1 gathers a non-exhaustive list of combinations of nanoparticles and base fluids prepared by different research groups.

Table I. 1:Nanoparticle / base fluid combinations (Ribeiro and Gruss 2009)

	Acétone	Eau	Ethylène glycol	Huile	Toluène	Décène	éthanol
Ag		×		×			
AIN							×
Au		×			×		
$Al_{70}Cu_{30}$			×				
Al_2O_3		×	×	×			
Bi_2Te_3							
C (diamant)		×					
C (graphite)		×		×			
C (NTC)		×		×		×	
C (fulleréne)				×	×		
Cu	×	×	×	×			
CuO		×	×				
Fe			×				
SiC		×					
SiO_2		×	×				
TiO_2		×	×				
WO_3			×				
ZrO_2		×					

1. 3. Types of nanoparticles

The production of new nanomaterials (nanoparticles) is a rapidly expanding field of research, so only the nanoparticles most commonly used in heat transfer applications are briefly mentioned here.

In general, nanoparticles can be classified according to their shape into two broad categories (Figure 2):

- Spherical nanoparticles for which several types of materials can be used for their manufacture. These spherical nanoparticles can thus be based on metals (Aluminum Al,

Copper Cu, Iron Fe, Gold Au, Silver Ag, etc.) or metallic oxides (Aluminum oxide Al2O3, Copper oxide CuO, Titanium oxide TiO2, etc.)).

- Nanotubes (CNT Carbon nanotubes, titanium TiO_2 nanotubes, Silicon nanotube, etc.)

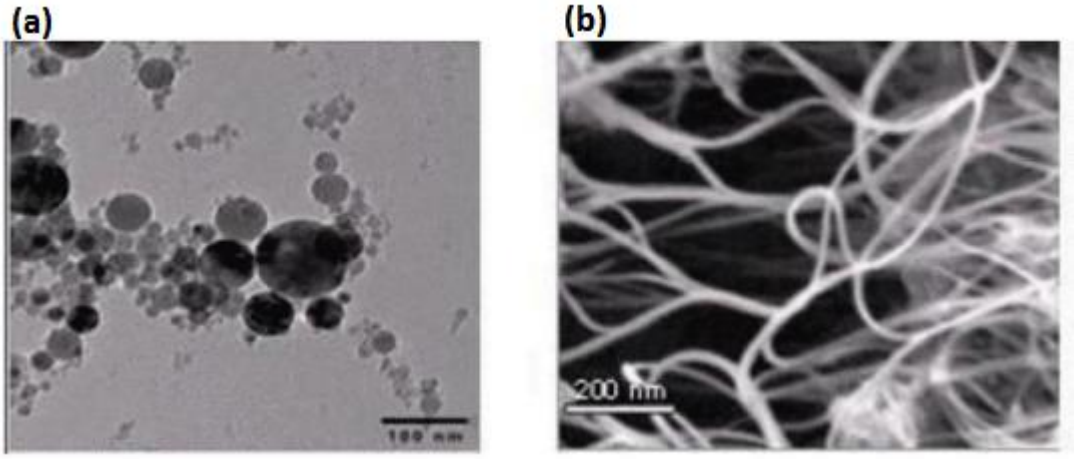

Figure 2:(a) Spherical nanoparticles; (b) Carbon nanotubes (Bang and Chang, 2005).

1. 4. Manufacture and preparation of nanofluids

The delicate point is the manufacture of these small pieces of material more or less well calibrated. No need to try to make it at home by sanding a piece of copper to turn it into dust for example. It will only make particles of micrometric size at best, which will foul the circuit. There are many manufacturing processes for nanoparticles. They can be classified into two categories:

- Physical processes, such as mechanical grinding.
- Chemical processes, such as laser pyrolysis or chemical precipitation

In general, the nanoparticles used for the synthesis of nanofluids are based on oxides, nitrides, carbides, pure metals or alloys, carbon nanotubes (CNTs). Composite particles can also be found which can use polymers.

There are two main methods to obtain a nanofluid:

-**The one-step method** consists of producing the nanoparticles in the base fluid. Less industrial, it can only be used for certain nanofluids, but helps prevent the agglomeration and oxidation of nanoparticles. An example of a process consists in condensing a metallic vapor in the form of nanoparticles in a reactor on a film of liquid at low vapor pressure.

-The two-step method consists of first producing the nanoparticles, then dispersing them in the base fluid. To allow good dispersion, strong mechanical action using a rotary stirrer or ultrasound is often necessary to break up the agglomerates. In addition, to avoid agglomeration due to attractive forces between particles, electrostatic repulsive forces are used by charging the surface of the particles by adjusting the pH.

Steric repellant forces can also be used with molecules adsorbed or grafted onto the surface.

The manufacturing processes are physical or chemical in nature. They are the subject of much research to improve the production cost which sometimes remains high given the difficulties of implementation and to obtain particles of the desired size. Each method has its drawbacks and some are not suitable for producing large quantities of nanoparticles for mass production given the constraints inherent in the process. The main means can be:

- Mechanosynthesis (high energy grinding).
- Chemical precipitation (reduction of metal salts for example). Chemical or physical vapor deposition (CVD or PVD).
- Plasma-assisted chemical vapor deposition (PECVD).
- Condensation of vapors by sudden expansion in supersonic nozzles.
- Radiofrequency cathode sputtering.
- Sublimation by laser ablation (vaporization of a sample by laser pulse).
- Laser pyrolysis (interaction between a continuous laser beam and a flow of reagents).
- The disintegration of submerged electrodes by the passage of sparks (as for machining by electroerosion).

2. Thermophysical properties of nanofluids

The thermophysical properties (thermal conductivity, dynamic and kinematic viscosity, specific heat capacity, etc.) are profoundly modified by the addition of nanoparticles and a large number of parameters can have a significant effect on this deviation (material, size, the aspect ratio, the concentration of particles in suspension, the conductivity of the base fluid, the temperature of the medium). Many research groups are trying to understand what are the mechanism or mechanisms at the origin of such differences but no phenomenology has yet been able to be formulated in a concise and satisfactory manner.

2. 1. Thermal conductivity of nanofluids

Nanoscale particle dispersions with a continuous liquid phase, often referred to as nanofluids, are of interest to many applications in process and energy technology. We can cite here the miniaturization of electronic devices by efficient cooling [1], the development of high-performance materials for thermal insulation [2], or the design of new working fluids for energy storage [3]. A key property characterizing dispersions is their effective thermal conductivity. The first experimental observations in the 1990s asserted that adding a small amount of solid nanoparticles to liquids can improve the effective thermal conductivity of nanofluids by up to 250% compared to the base fluid [4]. This report has triggered a plethora of experimental and theoretical studies, most of which give similar conclusions, as highlighted in the review article by Tertsinidou et al. [5]. However, other studies do not observe any significant improvement [5,6,7]. So far, debate has continued on the relevant mechanisms affecting thermal conduction in nanofluids, where Brownian motion [8,9,10], aggregation [11, 12] and interfacial stratification [13, 14] related to particles or a combination of these effects have been considered to be the main factors in improved energy transport.

Heat transfers within fluids lead to many practical and industrial applications, including in transportation, power supply, air conditioning and electronic cooling, etc. The current development of nanosciences originates from the demonstration of the specific properties of matter with nanometric dimensions. This has given rise to new fields of study in a large number of laboratories and has enabled the development of fluids with original properties.

Since nanoparticles with high thermal conductivity suspended in the base fluid which has low thermal conductivity, remarkably increase the thermal conductivity of nanofluids. Researchers have developed several models to predict the estimate of the conductivity of the nanofluid and many experiments have been carried out to compare the experimental data with these analytical models, made up of very regular elements such as spherical nanoparticles. The models described in the literature are prediction tools developed in order to understand the mechanisms of heat transfer within nanofluids. In this section, we will present the models most used in the case of nanofluids.

Maxwell model

Maxwell's model [15] and its derivatives are probably the most widely used in the literature. This basic model assumes that the particles are spherical, millimeter or microscopic in size, and are dispersed in low concentrations in a continuous matrix. [17]:

$$\frac{\lambda_{nf}}{\lambda_{bf}} = 1 + \frac{3(\alpha - 1)\varphi}{(\alpha + 2) - (\alpha - 1)\varphi} \quad \textbf{(I. 1)}$$

With $\alpha = \frac{\lambda_p}{\lambda_{bf}}$

Hamilton-Crosser model

This model [16], derived from that of Maxwell, incorporates a form factor n to take into account the non-spherical shape of the particles:

$$\frac{\lambda_{nf}}{\lambda_{bf}} = \frac{\alpha + (n-1) + (n-1)(\alpha - 1)\varphi}{\alpha + (n-1) + (1-\alpha)\varphi} \quad \textbf{(I. 2)}$$

n=3: Maxwell model for spherical particles.

n=6: Cylindrical particles.

Bruggemen model

Bruggemen proposed an implicit model which makes it possible to predict the thermal conductivity of nanofluids without limitation on the volume concentration. This model assumes spherical shaped particles [18]:

$$\varphi\left(\frac{\lambda_p - \lambda_{nf}}{\lambda_p + 2\lambda_{nf}}\right) + (1-\varphi)\left(\frac{\lambda_{bf} - \lambda_{nf}}{\lambda_{bf} + 2\lambda_{nf}}\right) = 0 \quad \textbf{(I. 3)}$$

Xuan model

Xuan's model is another extension of Maxwell's law, which this time takes into account the effect of Brownian motion of particles and clusters of particles with a mean radius of gyration r_a [18]:

$$\lambda_{nf} = \frac{\lambda_p + 2\lambda_{bf} + (\lambda_p - \lambda_{bf})\varphi}{\lambda_p + 2\lambda_{bf} - (\lambda_p - \lambda_{bf})\varphi}\lambda_{bf} + \frac{\rho_p \varphi C_{pp}}{2}\sqrt{\frac{K_B T}{3\pi\eta r_a}} \quad \textbf{(I. 4)}$$

Chon model

A recent model due to Chon [19] incorporates the effect of temperature, particle size, volume fraction, physico-chemical properties of the heat transfer fluid and Brownian motion [18]. This model is to date and to our knowledge the most complete and the most suitable to describe our experimental results:

$$\frac{\lambda_{nf}}{\lambda_{bf}} = 1 + 64.7\varphi^{a}\left(\frac{d_{bf}}{d_{p}}\right)^{b}\left(\frac{\lambda_{p}}{\lambda_{bf}}\right)^{e} P_{r}^{d} R_{e}^{e} \qquad \textbf{(I. 5)}$$

with Pr the Prandtl number of the heat transfer fluid and Re the Reynolds number, here based on the speed of Brownian motion of nanoparticles in the fluid. a, b, c, d and e are dimensionless numbers to be determined for each type of nanofluid.

This model was used by Chon to model the thermal conductivity of the water/Al_2O_3 nanofluid. The values of the parameters a, b, c, d and e found by Chon in this particular case are: a = 0.746; b = 0.369; c = 0.7476; d = 0.9955 and e = 1.2321 [18, 20].

The following figure gathers the models of the spherical particles and of the cylindrical particles, also the comparison of some experimental study.

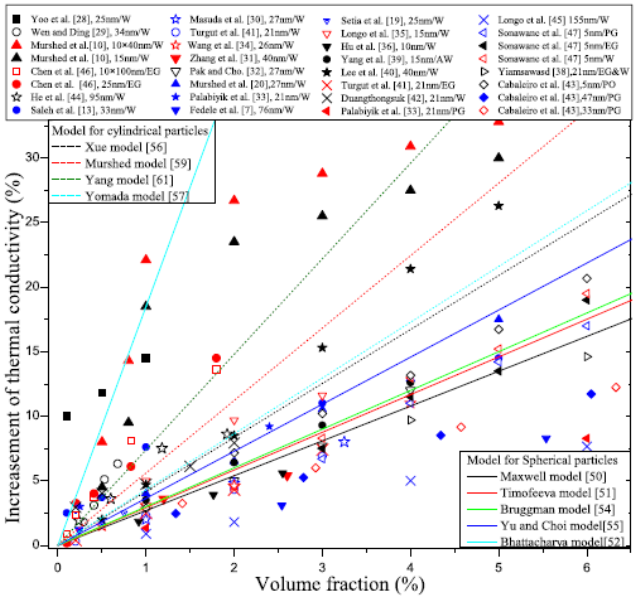

Figure 3:The comparison of various model predictions with experimental data for TiO2 nanofluids at room temperature [21].

2. 2. Viscosity of nanofluids

Viscosity characterizes the ability of a fluid to flow. His knowledge is fundamental for all applications involving the transport of fluids. The addition of the nanoparticles helps to increase and improve the thermal conductivity of the nanofluid, but it can also lead to an unfavorable increase in dynamic viscosity. Numerous theoretical and experimental studies have been carried out in order to estimate or measure the dynamic viscosity of nanofluids, and to quantify the

importance of the main parameters that influence it. Several theoretical models have been developed to predict the evolution of the dynamic viscosity of suspensions under certain conditions. In this part, we will focus on the models most used in the case of nanofluids.

Einstein's Law

Einstein was the first to study the evolution of the viscosity of a dilute suspension as a function of the volume fraction of the solid [22]. He linked viscosity to the dissipation of energy in the suspension by spherical and rigid particles. Einstein finally came to a simple relation valid only in the case of a very dilute suspension (φ≤0.02) of monodisperse spheres [2,3]:

$$\eta_{nf} = \eta_f \left(1+2.5\varphi\right) \quad \textbf{(I. 6)}$$

with $\varphi = \frac{Vs}{Vs + Vf}$ the volume fraction of solid, V_s the volume of the solid phase in suspension and V_f the volume of the host fluid. In order 2 in φ, Einstein's formula is written:

$$\eta_{nf} = \eta_f \left(1 + 2.5\ \varphi + k_2\varphi^2\right) \quad \textbf{(I. 7)}$$

with $5.2 \leq k^2 \leq 6.2$.

Laws of concentrated suspensions

In the field of concentrated suspensions (φ>0.5), empirical or semi-empirical relations based in part on Einstein's relation have been developed [22]. In this field, the viscosity of the suspension is no longer essentially governed by the viscosity of the host fluid and the solid volume fraction but it also depends on the optimal organization of this dry solid fraction, characterized by the maximum stacking compactness. granular φm. Three relationships are frequently used in the field of concentrated suspensions (table I.2).

Table I. 2: Some semi-empirical models of dynamic viscosity for concentrated suspensions

Equation name	Equation
Mooney [2]	$\eta_{nf} = \eta_n \exp\left(\frac{2,5\varphi}{1-\frac{\varphi}{\varphi m}}\right)$ **(I. 8)**
Krieger-Dougherty [4]	$\eta_{nf} = \eta_n \left(1-\frac{\varphi}{\varphi m}\right)^{-2,5\varphi m}$ **(I. 9)**
Quemada [5]	$\eta_{nf} = \eta_n \left(1-\frac{\varphi}{\varphi m}\right)^{-2,5\varphi m}$ **(I. 10)**

2. 3. Electrical conductivity of nanofluids

One of the most important thermophysical properties is the electrical conductivity of nanofluids. The results reveal considerable enhancement of this property [23,24] with the addition of nanoparticles to the base fluid. Shen et al. [10] used ZnO as a nanoparticle and insulated oil as the base fluid. They observed 973 times enhancement in the electrical conductivity in a volume fraction of about 0.75%. Glover et al. [24] observed that with the addition of about 0.5% (by weight) functional sulfonated carbon nanotube, electrical conductivity increased 13 times. White [25] reported 100 times enhancement in the electrical conductivity with the addition of 7% (by volume) of nanoparticles. They also observed that the electrical conductivity increased with reducing the particle size. Pastoriza-Gallego et al. [26] investigated the electrical conductivity of ZnO nanofluids in propylene as the base fluid.They observed enhancement of about 100 times in a volume fraction of about 7%. Electrical conductivity is affected by different parameters such as: Brownian motion, agglomeration, and stability [27]. Bordi et al. [28] observed that with particle aggregation, the number of particles reduced and the size of particles increased. This matter reduces Brownian motion of particles and then electrical conductivity dropped. Literature review revealed that, the Maxwell model cannot predict this enhancement in the electrical conductivity. For example, Shen et al. [23] reported that the Maxwell model underestimates the measured experimental data of the electrical conductivity. Based on this underestimation, they reported two mechanisms of dynamic and static for the electrical conductivity of nanofluids. Sarojini et al. [29] observed an unsatisfactory agreement between the experimental data and theoretical results of Maxwell model and they attributed this difference to the polarization effect

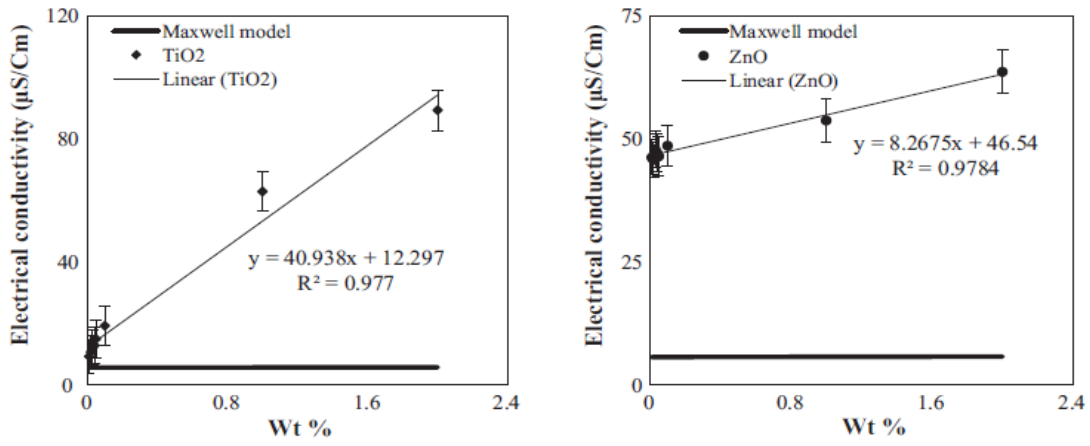

Figure 4:Electrical conductivity of nanofluids as function of concentration at 300K [30]

3. Elaboration methods of nanocomposites based on nanomaterials in polymer's matrix

INTRODUCTION

In order to disperse nanoparticles in an organic medium, the main problem to be faced is to avoid the aggregation of these nanoparticles within the matrix.

Indeed, whatever the morphological aspect of the nanoparticles, they generally tend to form aggregates stabilized by various types of interactions (ionic, hydrogen bridges, Van der Waals, etc.). These interactions are most often more important than the interactions between the surface of the nanoparticles and the organic matrix in which it is desired to disperse them. These types of interactions, for example, lead the carbon nanotubes to agglomerate in bundles. Likewise, these interactions, more particularly anionic attraction in the case of montmorillonite sheets, keep these sheets stable, thus creating a highly hydrophilic interlayer space preventing the penetration of a large number of organic molecules, which are often hydrophobic. It is therefore, most of the time, necessary to "pre-treat" the nanoparticles using compatibilizers or surfactants (chemical grafts) to improve their dispersion and their distribution within the matrix which receives them. There are then several techniques for developing these polymer matrix nanocomposites. The main ones are:

- direct mixing of the polymer and nanoparticles in solution (aqueous or solvent)

- mixing in the molten polymer,

- in situ polymerization in the presence of nanoparticles,

3. 1. Mixture in solution method

The production principle is based on the possibility of dispersing the nanoparticles in a solvent in which the polymer is soluble.

- The nanoparticles are mixed with a suitable solvent.

- The polymer is also dissolved in the same solvent.

- The mixture of the two solutions therefore allows the polymer to come to be absorbed and to be inserted between the nanoparticles.

- The nanocomposite is then obtained by evaporation of the solvent.

The advantage of this method is that it makes it possible to produce intercalated nanocomposites from a low polarity polymer matrix. On the other hand, the disadvantage is that it remains very little applicable in the industrial environment given the large amount of solvent required.

3. 2. Processing in the molten state

The principle is to mix the polymer in the molten state (thermoplastic) and the nanoparticles. The shearing effected during mixing (in extrusion for example) influences the dispersion of the nanoparticles. Under these conditions, if the interaction between the matrix polymer and the surface area of the nanoparticles is good, the mobility of the polymer chains is sufficient to penetrate the inter foliar space and form an intercalated or exfoliated nanocomposite. However, the simple mixing of certain polymers like polypropylene with nanoparticles is sometimes not enough. In fact, the apolarity of the polymer matrix leads to poor interaction with the nanoparticle and does not allow good intercalation. For this type of polymer, it is then necessary either to pre-treat the polymer also by chemical grafting (maleic anhydride: polar substituent) or to use copolymers. This

method preferred by manufacturers due to its simplicity and profitability. Indeed, the advantage that it presents, apart from dispensing with the use of solvents, is that it allows the use of conventional polymer processing techniques.

3. 3. In situ polymerization

This technique for preparing nanocomposites consists in polymerizing the monomer (s) in the presence of nanoparticles figure 5. The chemistry of the sol-gel process is another in-situ method of preparing nanocomposites, involving hydrolysis reactions. and condensation of MXn type precursors where M is a metal ion (Si, Ti, Zr, Sn, Al, etc.) and X is a group sensitive to hydrolysis. Typically, X is an alkoxide (-OMe, -OEt) or a halide (-Cl). Figure 6 shows schematically the hydrolysis-condensation mechanism of a metal alkoxide. The sol-gel process (soft chemistry) is a very widely used method for the preparation of composite materials, given the mild experimental conditions in which the material is prepared [31, 32 , 33, 34, 35 ,36] . Typically, the hydrolysis-condensation step of the precursor is carried out in solution in an organic solvent in the presence of water and of a catalyst, and in ambient temperature. The final structure of the inorganic network is managed by the nature of the solvent and of the catalyst, and the relative concentrations, with respect to that of the precursor, of water and of catalyst. After the synthesis step, the solvent is extracted then the material is subjected to various heat treatments adapted to the thermal resistance

of the organic component. From the sol-gel process, different strategies have been developed to generate an inorganic network in an organic medium (polymer) [37].

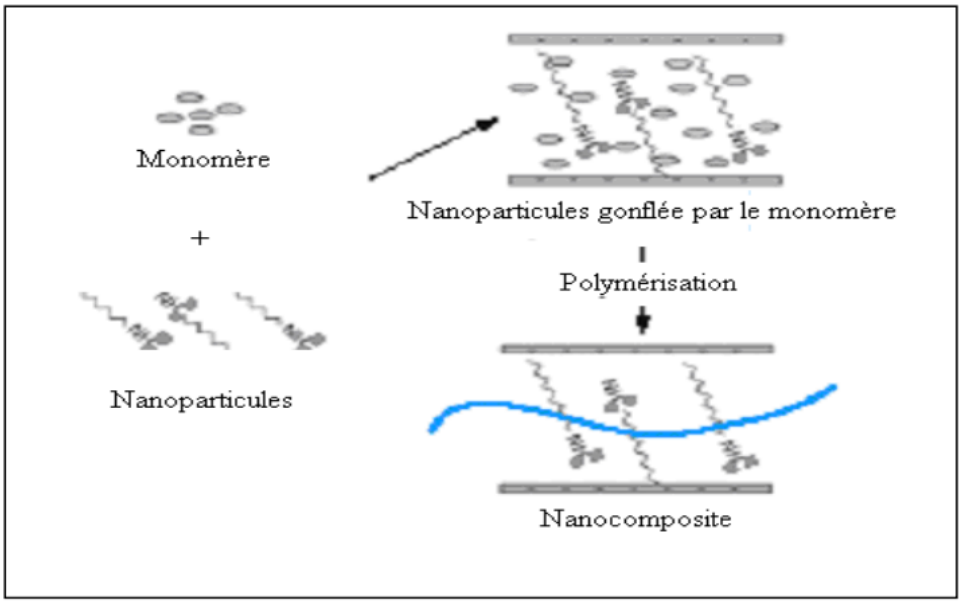

Figure 5:Principle of in situ polymerization[38]

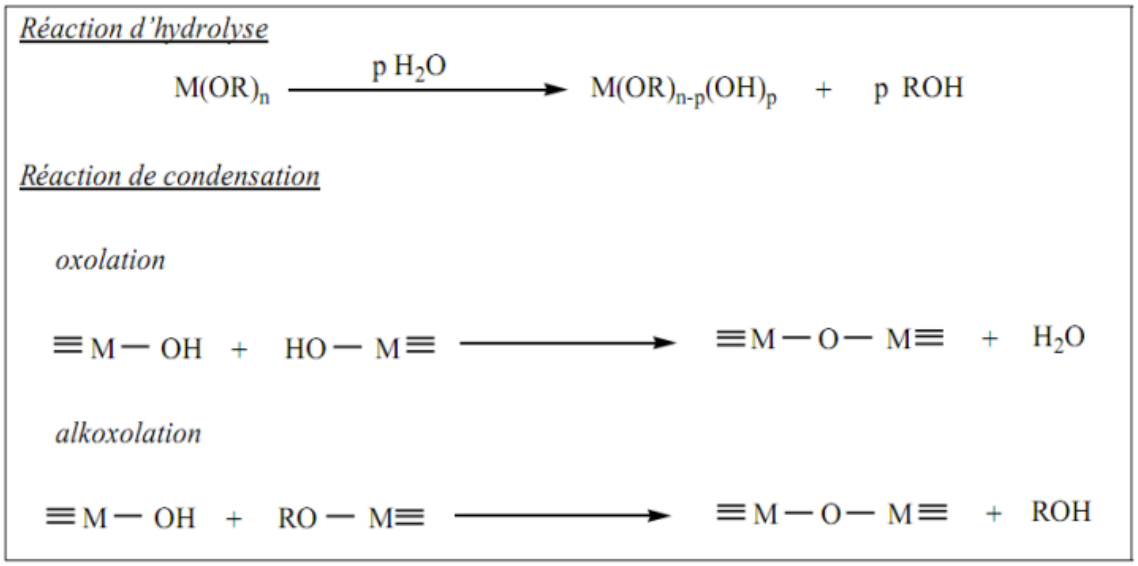

Figure 6:Hydrolysis-condensation mechanism of the sol-gel process in the case of a metal alkoxide[38]

4. Polytetrafluoroethylene (PTFE) properties and applications

INTRODUCTION

PTFE is better known in the industrial and commercial field under the name Teflon. It is a practically branchless linear polymer composed of carbon and fluorine atoms. PTFE has a hexagonal crystal structure with 15 CF2 per unit cell [39]. The individual polymer chains have a helical configuration and are roughly tight hexagonal [40]. The detailed structure of PTFE has been reported in the literature [41]. PTFE has chemical and thermal resistance (−200°C to +260°C, temporarily up to 300°C). It has a very low dielectric constant and a low melting rate. It does not dissolve in any of the strong acids, including hot fuming nitric acid. [42] This polymer is used in the manufacture of items such as pump valves and pipes where chemical resistance to materials is required. In addition, this thermoplastic material has excellent sliding properties, a non-stick surface and the best insulating properties. This contrasts, however, with low mechanical strength and high density compared to other plastics [43].

4. 1. Applications of PTFE in various fields

Polytetrafluoroethylene (PTFE) or teflon as indicated in the last paragraph has been recognized as being the most widely consumed fluoropolymer in the world. Since the discovery of this material, PTFE has flourished and the applications have proven to be innumerable. Over the past years the growth of PTFE in industrial, domestic and defense applications is steadily increasing without any hindrance. The range of applications around the world differs when PTFE has been cast as a pure material or as a composite. The applications of PTFE in various fields are listed in the following.

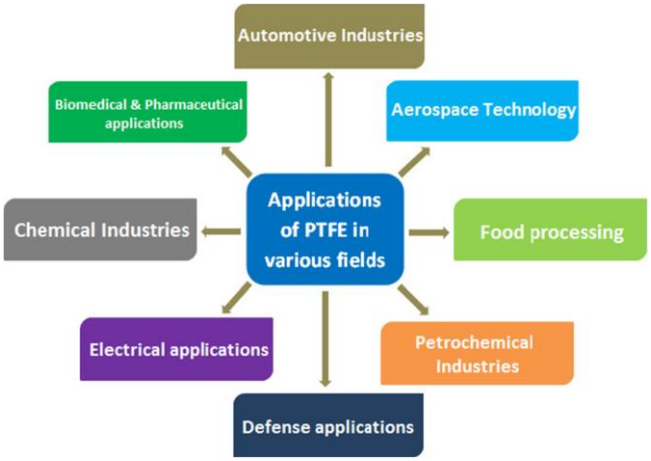

Figure 7:Application of PTFE in various fields[44]

4. 2. Optical and spectral properties of PTFE

The optical and spectral properties inherent in PTFE greatly aid in the instrumentation of efficient optical devices. The parameters of light reflection and scattering of PTFE are extremely high; therefore, material was unavoidable in optical instrumentation. The reflectance factor is the measure of the surface's ability to reflect light, which is equal to the ratio of reflected flux to incident flux. PTFE exhibits good optical characteristics of a broad ultraviolet to near infrared spectrum and performs well when exposed to light or other electromagnetic radiation. Reflectance angle measurements were studied using a reflectometer which was used to measure the bidirectional reflectance of the PTFE vane [45].

5. Notion of energy bands (Gap energy)

In an isolated atom, electrons can only be found in certain possible states characterized by quantum parameters to which discrete energy levels correspond. When identical atoms come together to form a solid, the interaction that appears between the electrons of the atoms of the crystal multiplies each discrete level into a set of infinitely close states: a band of electronic energy in a crystal therefore results from the hybridization of the individual levels of the atoms that make up the crystal. The possible energies for an electron in a solid form what are called allowable bands separated by forbidden bands. The binding orbitals form the band valence (the last full) and the anti-binder that of conduction (the first empty), separated by a forbidden band (Gap) of width Eg figure 8.

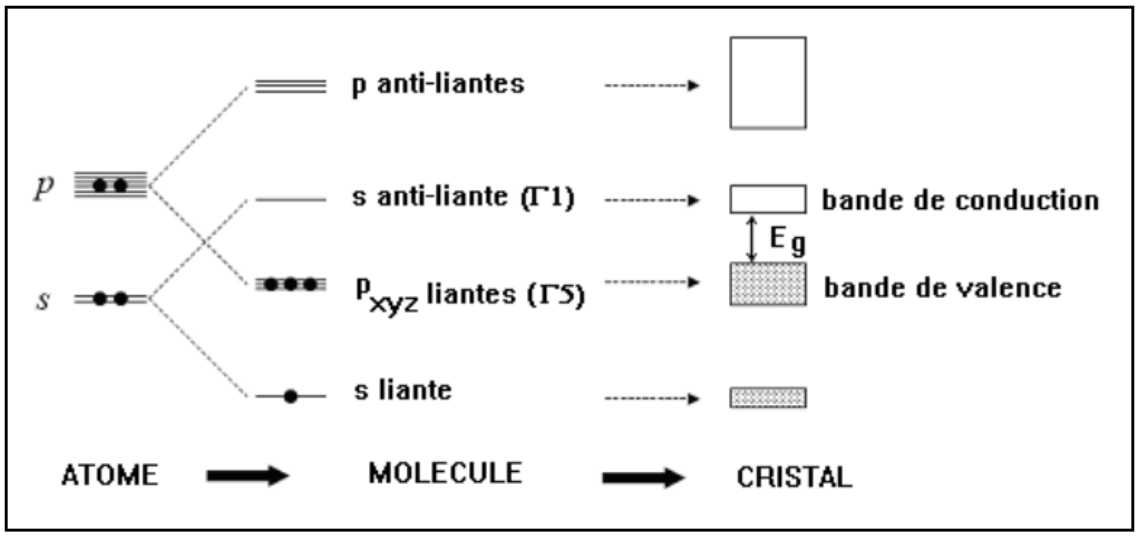

Figure 8:Electronic levels in an isolated atom and in a crystal[38]

Figure 9 shows the energies of the forbidden band as a function of the lattice parameter for some semiconductors.

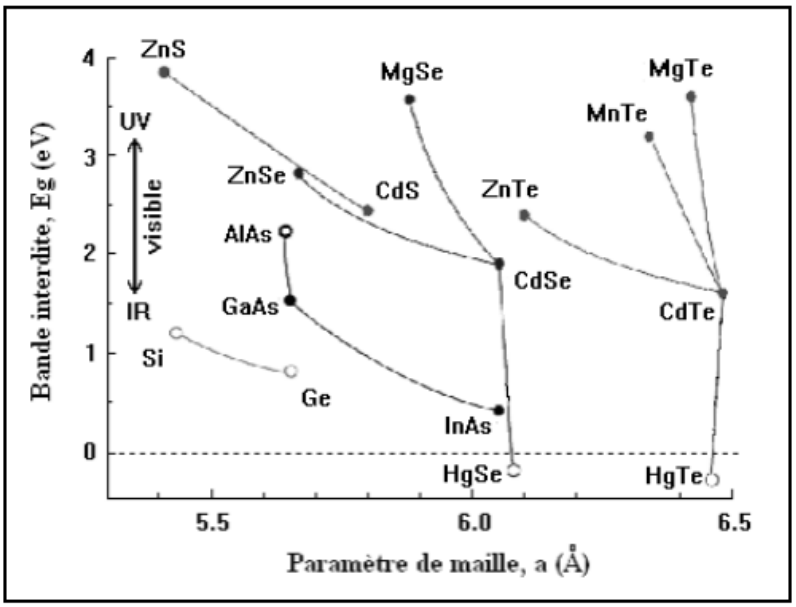

Figure 9:Bandgap as a function of the cubic mesh parameter for different semiconductors [46].

6. Techniques of characterizations

6. 1. X-ray diffraction (XRD) of Li2PtO3

X-ray diffraction (XRD) is an important technique for determining the structures of crystals. The theory behind XRD is the result of the pioneering work of the Braggs (father and son). The main principle of XRD is the diffraction of X-rays in specific directions by atoms in crystal structure. Since interplanar distances in crystals are of the order of Angstroms, therefore X-rays are the appropriate choice, since the wavelength of the wave must be of the order of the size of the slit for the phenomenon diffraction takes place. Braggs suggested that the crystal structure could be thought of as a lattice of atoms forming several planes. X-rays hitting an atom will scatter in a certain direction. Scattered X-rays can interfere constructively if they are in phase or destructively if they are out of phase.

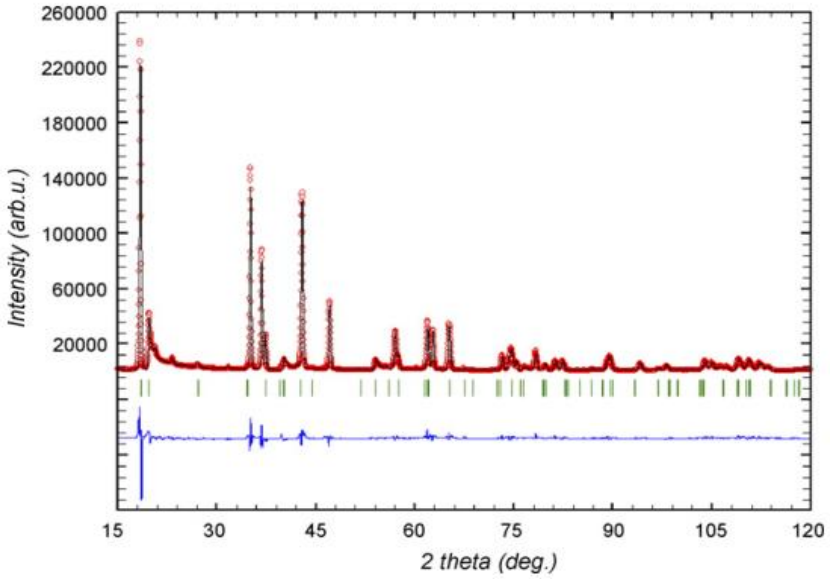

Figure 10:Experimental X-ray powder diffraction pattern (dotted curve) compared to the FAULTS-refined profile (continuous line) and difference curve corresponding to sample Li2PtO3 [47].

6. 2. Infrared and UV-visible spectrophotometer of Co2P2O7, 6H2O

6. 2. 1. Infrared spectroscopy

Infrared spectroscopy (IR spectroscopy) is an Optical technique that detects molecular bond vibrations and rotations upon absorption of infrared light. Because different chemical functional groups absorb IR light at different frequencies, IR spectroscopy can be used for chemical structure analysis, chemical fingerprinting and chemical imaging. This absorption has shown the existence of the bonds of certain samples, the infrared spectrum represents the transmittance T (%) on the ordinate; it is expressed as a percentage (%) according to the number of waves on the abscises, and is expressed in (cm^{-1}). We can see that the absorption strips are pointing downwards a low transmission value corresponds to a high absorption and each band is characterized by its position, width and intensity.

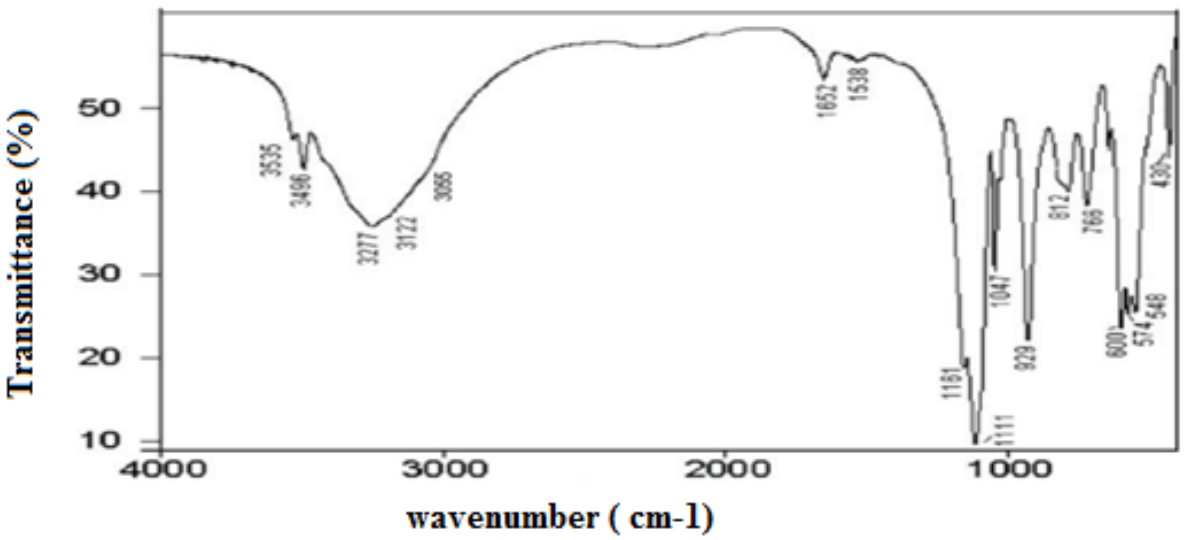

Figure 11:Infrared spectrum of Co2P2O7, 6H2O

6. 2. 2. UV-Visible spectroscopy of KMnPO4•H2O

The T92 + is a high-performance dual beam spectrophotometer with a variable spectral bandwidth from 0.1 to 5 nm, selected by a continuously variable slit. Pyrophosphates exhibit high transmittance in the UV-visible region and with a minimum abrupt absorption of around 300 nm. While the interaction with infrared light causes vibrational transitions for molecules, the shorter wavelength and higher energy radiation in the UV (200-400nm) and visible (400-700nm) range of the electromagnetic spectrum cause many organic molecules to undergo electronic transitions. This means that when a molecule absorbs energy from UV or visible light, one of its electrons changes from a lower energy to a higher energy molecular orbital. UV-visible absorption spectroscopy (UV-Vis) is the measurement of the attenuation of a light beam after it has passed through a sample or after reflection on the surface of a sample. Absorption measurements can be performed at a single wavelength or over a wide spectral range. The absorption of UV or visible radiation corresponds to the excitation of outside electrons. There are three types of electronic transition that can be considered:

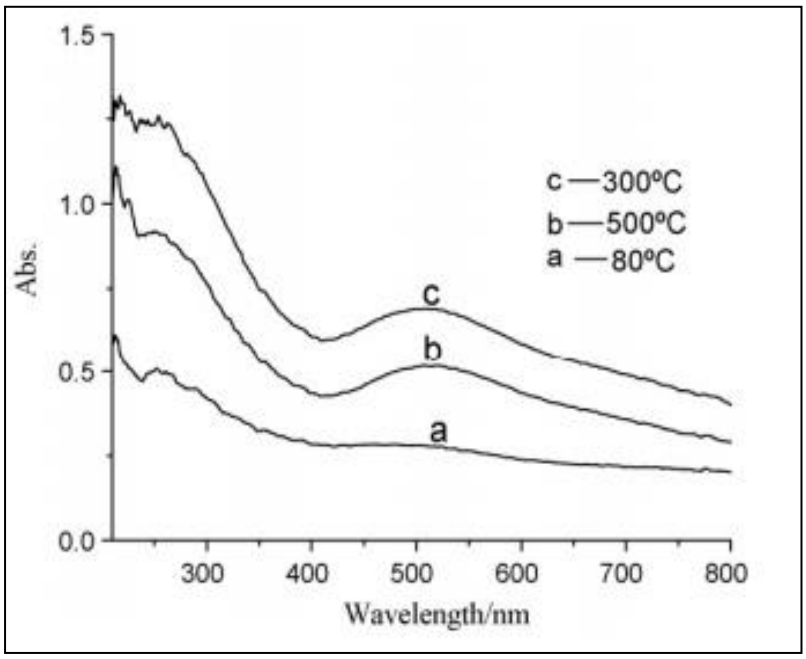

Figure 12:UV–visible absorption spectra of the product of KMnPO4•H2O a different temperature[48].

6. 3. Transmission Electron Microscopy (TEM) and Scanning Electron Microscopy (SEM)

6. 3. 1. Transmission electron microscopy

Transmission electron microscopy (TEM) makes it possible to observe at high resolution (1 to 2 Å) biological samples or very thin materials containing small constituents such as cell organelles, very fine nanoparticles, etc. This microscopy technique also makes it possible to analyze the composition of the sample at the atomic scale, namely the aggregation of a few atoms to form nanoparticles.

An electron beam emitted by an electron gun passes through the sample at high speed. The interaction between the electrons and the sample produces radiation that is transcribed into an image that can be viewed on a screen. The optical image obtained is in black and white and has different contrasts depending on the number of electrons that have passed through the sample.

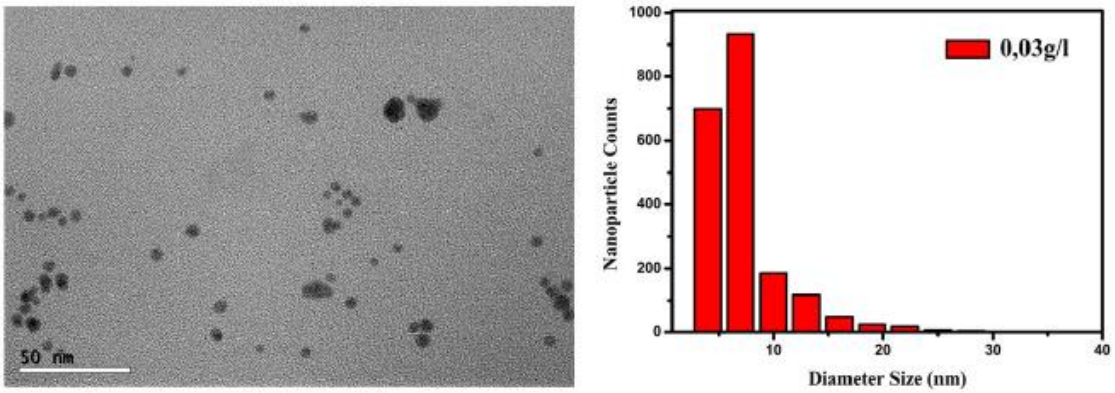

Figure 13:TEM images of Silver nanoparticles synthesized at concentration 0,03g/L of Silver nitrate[62]

6. 3. 2. Scanning electron microscopy

Scanning electron microscopy (SEM) is used to observe the surface of large biological samples at the nanoscale.

Unlike TEM, the electron beam does not pass through the sample but scans its surface. The reflected radiation produces a signal transcribed into an image that can be viewed on a screen. The image obtained is in black and white and presents contrasts allowing a view of the surface in relief, with a great degree of detail (visualization of bacteria on the surface of the skin or characterization of the surface state of the hair for example).

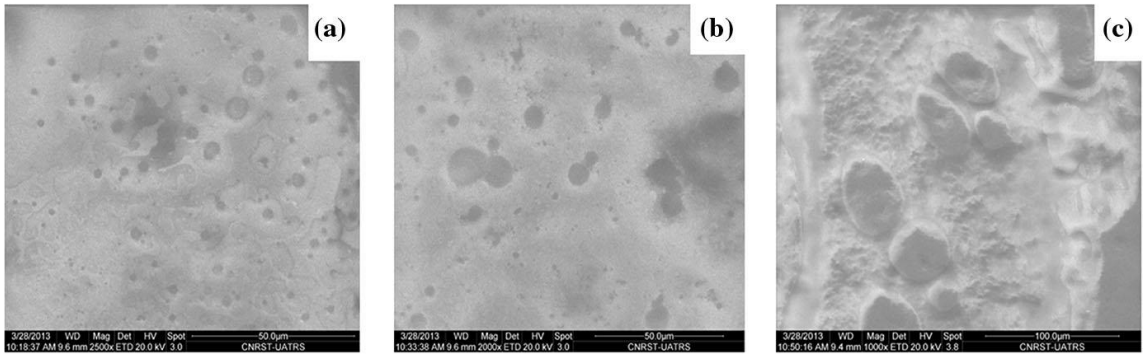

Figure 14:SEM images of Silver-latex nanocomposites at different MW irradiation times: a 40 s, b 90 s and c 120 s, respectively [63]

7. Simulation methods

7. 1. FDTD method

Since 1966, the FDTD method has been successfully applied by Yee [53], to various electromagnetic problems and phenomena, such as plasmonic applications [52]. Then, the FDTD method can model the propagation in dispersive media known as Drude material [52], [54]. The z-transform approach has been applied to describe the complex permittivity and its frequency dependence of the medium [55]. The effective permittivity at the interfaces of curved materials [57, 58, 59] was used to take into account the geometry of the system with the absorbent boundary conditions PML [56]. In this paper, the results of the 2D-FDTD numerical simulation are presented for silver cylinders immersed in a dielectric medium.

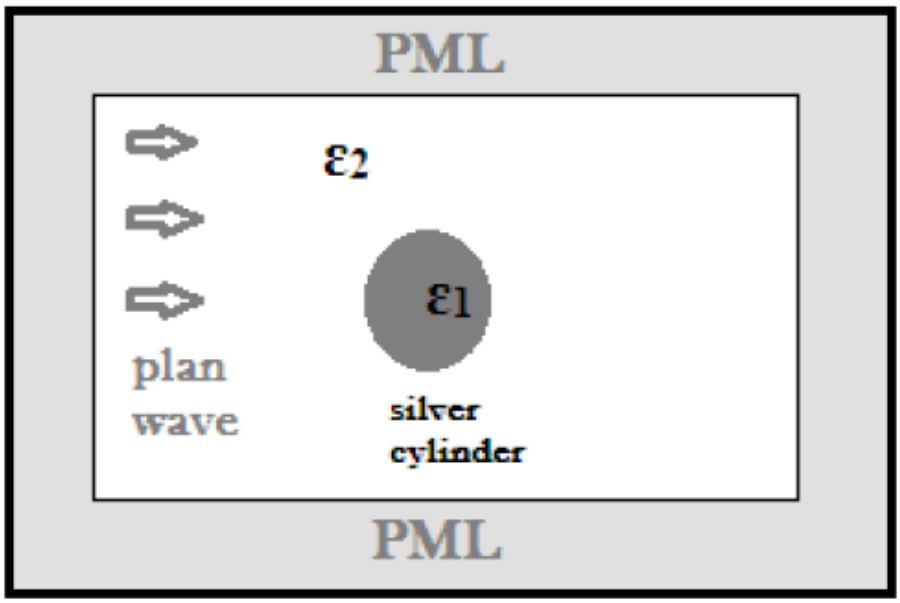

Figure 15:Computational Setup: an Incident TMz polarization illuminate[60]

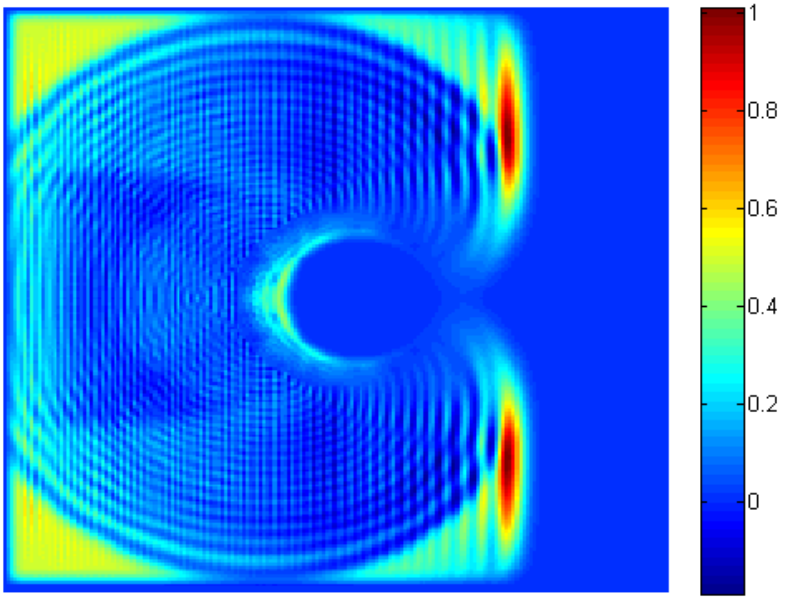

Figure 16:Visualization of the FDTD-computed Ez scattered field distribution along the x-y planar[60]

7. 2. Hot wire method

The studied structure is a wire generally made of platinum placed on a heated by the Joule effect using comsol multiphisique V.5.1. The wire is generally of the order of 25 µm in diameter, and of a few centimeters in length, on the other hand the mixture to be characterized is of the order of 2 or 3cm on the side. The following figure 17 shows a thermal image of the entire structure of a titanium oxide characterization.

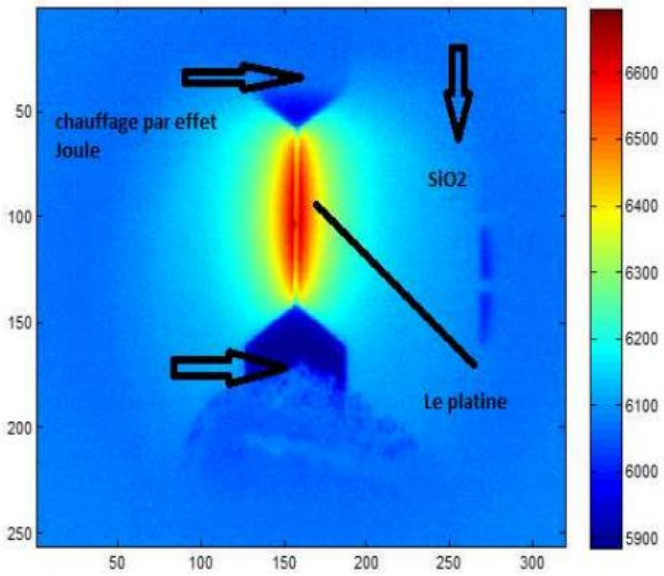

Figure 17:Thermal imaging of the structure[61]

CONCLUSION

In this chapter, we presented the different optical and electrical properties of nanoparticles of Silver, PTFE, Erbium, Gadolinium and Glycerol, and their fields of application, which are the subject of this work. This has been described from the of physical behavior point of view. The techniques for characterizing the materials to be produced are also presented in a short and well-planned manner, and among these techniques the hot wire technique (THW). This last technique was the subject of the simulation part which also represents the simulation of surface plasmon resonance (SPR) of nanoparticles.

References

[1] M.H. Buschmann, R. Azizian, T. Kempe, J.E. Juliá, R. Martínez-Cuenca, B. Sundén, Z. Wu, A. Seppälä, T. Ala-Nissila, Int. J. Thermal Sci. 129, 504–531 (2018)
[2] M. Schwan, L.G. Kramer, T. Sottmann, R. Strey, Phys. Chem. Chem. Phys. 12, 6247–6252 (2010)
[3] M.M. MacDevette, T.G. Myers, Int. J. Heat Mass Transf. 92, 550–557 (2016)
[4] S.U.S. Choi, Z.G. Zhang, W. Yu, F.E. Lockwood, E.A. Grulke, Appl. Phys. Lett. 79, 2252–2254 (2001)
[5] G. Tertsinidou, M.J. Assael, W.A. Wakeham, Int. J. Thermophys. 36, 1367–1395 (2015)
[6] G.J. Tertsinidou, C.M. Tsolakidou, M. Pantzali, M.J. Assael, L. Colla, L. Fedele, S. Bobbo, W.A. Wakeham, J. Chem. Eng. Data 62, 491–507 (2016)
[7] P. Keblinski, R. Prasher, J. Eapen, J. Nanopart. Res. 10, 1089–1097 (2008)
[8] S.P. Jang, S.U.S. Choi, Appl. Phys. Lett. 84, 4316–4318 (2004)
[9] J. Koo, C. Kleinstreuer, J. Nanopart. Res. 6, 577–588 (2005)
[10] R. Prasher, P. Bhattacharya, P.E. Phelan, J. Heat Transf. 128, 588–595 (2006)
[11] J.W. Gao, R.T. Zheng, H. Ohtani, D.S. Zhu, G. Chen, Nano Lett. 9, 4128–4132 (2009)
[12] E.V. Timofeeva, A.N. Gavrilov, J.M. McCloskey, Y.V. Tolmachev, S. Sprunt, L.M. Lopatina, J.V. Selinger, Phys. Rev. E 76, 061203 (2007)
[13] W. Yu, S.U.S. Choi, J. Nanopart. Res. 6, 355–361 (2004)
[14] H.U. Kang, S.H. Kim, J.M. Oh, Exp. Heat Transf. 19, 181–191 (2006) [15] C. Maxwell, A Treatise on Electricity and Magnetism. Oxford University Press, Cambridge, UK, (1904).
[16] R.L. Hamilton, O.K. Crosser. Thermal conductivity of heterogeneous two-component systems. Industrial and Engineering Chemistry Fundamen-tals 1 (3) (1962) 187-191.
[17] W. Yu, S.U.S. Choi. The role of interfacial layers in the enhanced thermal conductivity of nanofluids: A renovated Maxwell model. Journal of Nanoparticle Research 5 (2003) 167-171.
[18] R. S. Vajjha, D. K. Das. Experimental determination of thermal conductivity of three nanofluids and development of new correlations. International Journal of Heat and Mass Transfer 52 (2009) 4675-4682.
[19] C.H. Chon, K.D. Kihm, S.P. Lee, S.U.S. Choi. Empirical correlation finding the role of temperature and particle size for nanofluid (Al2O3) thermal conductivity enhancement. Appl. Phys. Lett. 87 (15) (2005) 153107.
[20] H. A. Mintsa, G. Roy, C. T. Nguyen, D. Doucet. New temperature dependent thermal conductivity data for water-based nanofluids. International Journal of Thermal Sciences 48 (2009) 363-371.
[21] L. Yang, K. Du, A comprehensive review on heat transfer characteristics of TiO2 nanofluids, Int. J. Heat Mass Transf. 108 (2017) 11–31.
[22] G. V. Casquillas. Contrôle de température et étude des transferts thermiques dans des dispositifs microfluidiques. These de doctorat, Faculte des sciences d'Orsay, effectuee au Lab- oratoire de Photonique et de Nanostructures, (2008).
[23] L. Shen, H. Wang, M. Dong, Z. Ma, H. Wang, Solvothermal synthesis and electrical conductivity model for the zinc oxide-insulated oil nanofluid, Phys. Lett. A 376 (2012) 1053–1057.
[24] B. Glover, K.W. Whites, H. Hong, A. Mukherjee, W.E. Billups, Effective electrical conductivity of functional single-wall carbon nanotubes in aqueous fluids, Synth. Met. 158 (2008) 506–508.
[25] S.B. White, Enhancement of Boiling Surfaces using Nanofluid Particle Deposition, The University of Michigan, 2010.
[26] M.J. Pastoriza-Gallego, L. Lugo, J.L. Legido, M.M. Piñeiro, Thermal conductivity and viscosity measurements of ethylene glycol-based Al2O3 nanofluids, Nanoscale Res. Lett. 6 (2011) 1–11.
[27] S. Ganguly, S. Sikdar, S. Basu, Experimental investigation of the effective electrical conductivity of aluminum oxide nanofluids, Powder Technol. 196 (2009) 326–330.
[28] F. Bordi, C. Cametti, P. Codastefano, P. Tartaglia, Electrical conductivity of colloidal systems during irreversible aggregation, Phys. A: Stat. Mech. Appl. 164 (1990) 663–672.
[29] K.K. Sarojini, S.V. Manoj, P.K. Singh, T. Pradeep, S.K. Das, Electrical conductivity of ceramic and metallic nanofluids, Colloids Surf. A: Physicochem. Eng. Aspect 417 (2013) 39–46. [30] S.N. Shoghl, J.

Jamali and M.K. Moraveji ; Electrical conductivity, viscosity, and density of different nanofluids: An experimental study; doi.org/10.1016/j.expthermflusci. 2016.01.004
[31] P. Hajji, L. David, J.F. Gerard et al., Synthesis, structure, and morphology of polymersilica hybrid nanocomposites based on hydroxyethyl methacrylate. Journal of Polymer Science: Part B: Polymer Physics, vol. 37, 3172-3187 (1999).
[32] C.J.T. Landry, B.K. Coltrain, M.R. Landry et al., Poly(vinyl acetate)/silica filled materials : materials properties of in situ vs fumed silica particles. Macromolecules, vol. 26, 3702-3712 (1993).
[33] J.E. Mark, Ceramic-reinforced polymers and polymer-modified ceramics. Polymer Engineering and Science, vol. 36, n°24, 2905-2920 (1996).
[34] L. Matejka, K. Dusek, J. Plestil et al. Formation and structure of the epoxysilica hybrids. Polymer, vol. 40, 171-181 (1998).
[35] B.M. Novak, C. Davies, "Inverse" organic-inorganic composite materials. 2. Free-radical routes into nonshrinking sol-gel composites. Macromolecules, vol. 24, 5481-5483 (1991).
[36] A. D. Pomogailo, Hybrid polymer-inorganic nanocomposites. Russian Chemical Reviews, vol. 69, n°1, 53-80 (2000).
[37] G. Kickelbick, Concept for the incorporation of inorganic building blocks into organic polymers on a nanoscale. Progress in Polymer Science, vol. 28, 83-114 (2003).
[38] Nassim TOUKA, Dispersion des nano-cristaux semi conducteurs dans des matrices à large bande interdite : Etude des propriétés optiques.
[39] Wunderlich, B. Macromolecular Physics, Vol. 1; Academic: New York, 1973.
[40] Liang, C. Y.; Krimm, S. J Chem Phys 1956, 25(3), 563–571.
[41] Bunn, C. W.; Howells, E. R. Nature 1954, 174, 549–551.
[42] Gowariker, V. R.; Viswanathan, N. V.; Sreedhar, Polymer Science; New Age International: India, 2002.
[43] Wikol, M.; Hartmann, B.; Brendle, J.; Crane, M.; Beuscher, U.; Brake, J.; Shickel,
T. 2nd ed.;W. L. Gore: Newark, DE, 2007.
[44] E. Dhanumalayan & Girish M. Joshi. Performance properties and applications of polytetrafluoroethylene (PTFE)—a review. doi.org/10.1007/s42114-018-0023-8
[45] Chen YC, Lin HC, Lee YD (2003) The effects of filler content and size on the properties of PTFE/SiO2 composites. J Polym Res 10(4):247–258
[46] F. Tinjoux, Thèse de doctorat, université Joseph Fourier, Grenoble I (2003).
[47] Kittel C, Kolb E, Bardon N. Physique de l'état solide. 7th ed. Paris: Dunod; 1998.
[48] panelA.GrugerA.NovakA.RégisPh.Colomban,Infrared and Raman study of polyaniline Part II: Influence of ortho substituents on hydrogen bonding and UV/Vis—near-IR electron chargePittayagorn Noisong and Chanaiporn Danvirutai*, Kinetics and Mechanism of Thermal
[49] Filippetti A, Hill NA. Coexistence of magnetism and ferroelectricity in perovskites. Phys Rev B 2002;65:195120.
[50] Gwénaël GOUADEC and Philippe COLOMBAN, Raman Spectroscopy of Nanomaterials: How Spectra Relate to Disorder, Particle Size and Mechanical Properties, Progress in Crystal Growth & Characterization of Materials 20
[51] Fennie CJ, Rabe KM. Ferroelectric transition in YMnO3 from first principles. Phys Rev B 2002;72:100103.
[52] Ahmed, I.; E. H. Khoo; O. Kurniawan; E. P. Li. Modeling and simulation of active plasmonics with the FDTD method by using solid state and Lorentz–Drude dispersive model. Optical Society of America B, Vol. 28, 2011, pp. 352–359.
[53] Yee, K. S. Numerical Solution of Initial Boundary Value Problems Involving Maxwell's Equations in Isotropic Media;IEEE Trans. Antennas Propagat. 1966, AP-14, 302–307.
[54] Kunz, K. S.; Luebbers, R. J. The Finite Difference Time Domain Method for Electromagnetics; CRC Press, Boca Raton, 1993.
[55] Sullivan, D. M. Electromagnetic Simulation Using the FDTD Method; New York, IEEE Press, 2000.
[56] Berenger, J. R. A perfectly matched layer for the absorption of electromagnetic waves; J. Computat. Phys. 1994, 114, 185-200.
[57] Zhao, Y.; Hao, Y. Finite-difference time-domain study of guided modes in nano-plasmonic waveguides; IEEE Trans. Antennas Propag. 2007, 55, 3070–3077.

[58] Zhao, Y.; Hao, Y. Conformal Dispersive Finite-Difference Time-Domain Simulations of Plasmonic Waveguides; IEICE 2007, 224-227.
[59] Mohammadi, A.; Jalali, T.; Agio, M. Dispersive contour-path algorithm for the two-dimensional finite difference time-domain method; Optics Express 2008, 16, 7397-7406.
[60] Otman Sofiane, Said Ouaskit. FDTD Simulations of Surface Plasmons Using the Effective Permittivity Applied to the Dispersive Media. American Journal of Electromagnetics and Applications. Vol. 5, No. 2, 2017, pp. 14-19. doi: 10.11648/j.ajea.20170502.11
[61] Nasser FEKIRI MASTER. Transferts de chaleur dans des éléments micro et nano structurés : Simulation et expérimentation par thermographie infrarouge et microscopie SThM
[62] M. Ider; K. Abderrafi ;A. Eddahbi, S. Ouaskit and A. Kassiba. Rapid Synthesis of Silver Nanoparticles by Microwave-Polyol Method with the Assistance of Latex Copolymer.DOI:10.1007/s10876-016-1096-6
[63] Ider; K. Abderrafi; A. Eddahbi, S. Ouaskit and A. Kassiba . Silver Metallic Nanoparticles with Surface Plasmon Resonance: Synthesis and Characterizations

CHAPTER II:

SYNTHESIS OF SILVER NANOPARTICLES BY MICROWAVE IRRADIATION AND THEIR EFFECT ON GAP ENERGY OF NANO-COMPOSITE BASED ON MWCNT

1. Synthesis and characterization of Silver nanoparticles by microwave irradiation

INTRODUCTION

The size of the nanoparticles of the metal objects such as silver, has an impact on the behavior of the mediums namely, the thermal conductivity [1], the electrical conductivity [2] of the composites associated that well be treated in the chapter III.

The silver nanoparticles are used in deferent fields, such as microelectronic [3], photo catalytic effect [3-5], optoelectronics [8], lithography [6], and in the field of biology as bacterial biosensors. All these applications of the metal nanoparticles are due to their important property, which is surface Plasmon resonance (SPR).

The size of the silver nanoparticles depends on the method of synthesis and the polymer used [9] (MW-Polyol; Electrochemical; Laser Ablation; Photochemical; Sonochemical; and chemical radiation [9-10]).

The technology requires a very short time in the industrial field therefore we require a rapid method, among these methods we state MW-polyol method [9-10]; which has effectiveness in controlling the length of synthesis of the size and the shape [9-10].

The formation of nanoparticles needs an enormous pressure, requires which can be generated by a microwave that applies irradiations on the base fluid which is in general a polar fluid ex: (ethanol, water) which transforms the irradiated energy to vibrations of the polar molecules and thus a rapid and homogeneous elevation of the temperature and the speed of the reaction.

1. 1. Materials and experimental Setup

The synthesis of nanoparticles by wet process is generally done by precursors of salts, the silver nitrate as the source of silver ($AgNO_3$, 99 % purity). And the solvent for silver nitrate is the ethanol that is used as pure solution, and the suspension is done by a polymer.

A silver nitrate (0.1504g) was dissolved in ethanol (40mL) and separated into three samples with 5mL, 10mL and 15mL. Then, 0.4g of latex copolymer dissolved in ethanol (40mL) and it was added 10mL to each sample. The samples were heated under MW irradiation at 300 W during 50s

The microwave setup used for the preparation of silver nanoparticles consists in microwave oven (Mars5-System from company CEM) working at frequency 2.45 GHz and maximum power of 1200W.

The silver nanoparticles were synthesized by reduction of silver nitrate in the presence of latex copolymer under MW irradiation. Latex concentration and microwave heating time were varied in

order to determine the optimum experimental conditions leading to monodispersed silver nanoparticles with controlled size and shape.

During the heating process, the colorless solution of the reaction mixture turned gradually faint yellow to the golden yellow color, characteristic of the silver nanoparticle formation. All the samples were cooled at 20–25 °C temperature just after the reaction with the aim to stabilize the silver-latex colloid structure.

1. 2. Characterization and discussions

1. 2. 1. Characterization by FT-IR Spectroscopy

The infrared spectrum represents the transmittance, the intensity transmitted, counted from 0 to 100%, relative to the intensity of the incident beam, instead of the intensity absorbed. Thus, on the spectrum I.R. the abscise is the wave number (in cm^{-1}) and the ordinate transmittance T expressed as a percentage. A 100% transmittance means that there is no absorption, so in I.R. the absorption bands point downwards. An IR spectrum extends from 400 cm^{-1} to 4500 cm^{-1}. The elongation of the O-H bond of the ethanol used gives an intense absorption band. The frequency of elongation depends on the existence or not of hydrogen bonds: H-O, the vibration frequency $\nu O{-}H$ is at 3386.5 cm^{-1}. In the interval of 1250 to 680 cm^{-1}, the absorption bands are associated with complex variations of the vibrational and rotational energy of the whole molecule. Table II.1 gives the frequencies of the basic fluid (Ethanol) with polymer (10mL) compound. Note also a strong and wide absorption band of 3200cm^{-1} at 3700cm^{-1} is characteristic of the O-H bond. The hydrogen bonds established between the alcohol molecules weaken the O-H bonds. This implies an enlargement of the band. The link O-H is in this case called "O-H linked" Figure 18 represents the spectrum of basic fluid (Ethanol) with polymer (10mL).

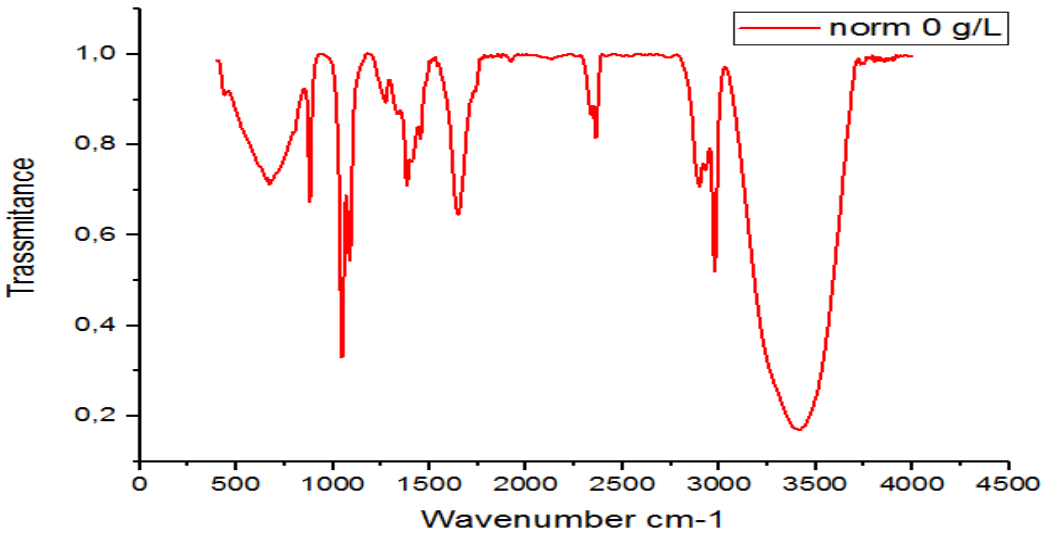

Figure 18:FT-IR spectrum of basicfluid (Ethanol) with polymer (10mL)

Table II. 1:Alcohol and polymer compound group frequencies

basic fluid (Ethanol) with polymer (10mL)			
Peak position	**full width at half maximum (FWHM)**	**Spectral form**	**Assignment**
662,21166 ± 1,59693	252,31582 ± 3,5894	delicate	Alcohol, OH out-of-plane
880,60518 ± 0,38883	14,65708 ± 0,80415	wide	
1061,03928 ± 0,40781	59,69744 ± 0,82977	wide	Primary alcohol, C-O stretch
1390,55933 ± 1,39166	132,36961 ± 2,91278	delicate	CH_2 et CH_3 deformation
1650,63546 ± 0,74355	82,76654 ± 1,52639	delicate	
2348,45799 ± 1,1646	46,83449 ± 2,36922	wide	
2903,65779 ± 1,10769	78,84766 ± 2,47902	delicate	elongation liaison C-H
2976,79162 ± 0,36142	22,64502 ± 0,8175	wide	Non bond hydroxyl group, OH stretch
3386,47884 ± 0,56928	340,74336 ± 1,26637	delicate	Normal ‘‘polymeric’’ OH stretch

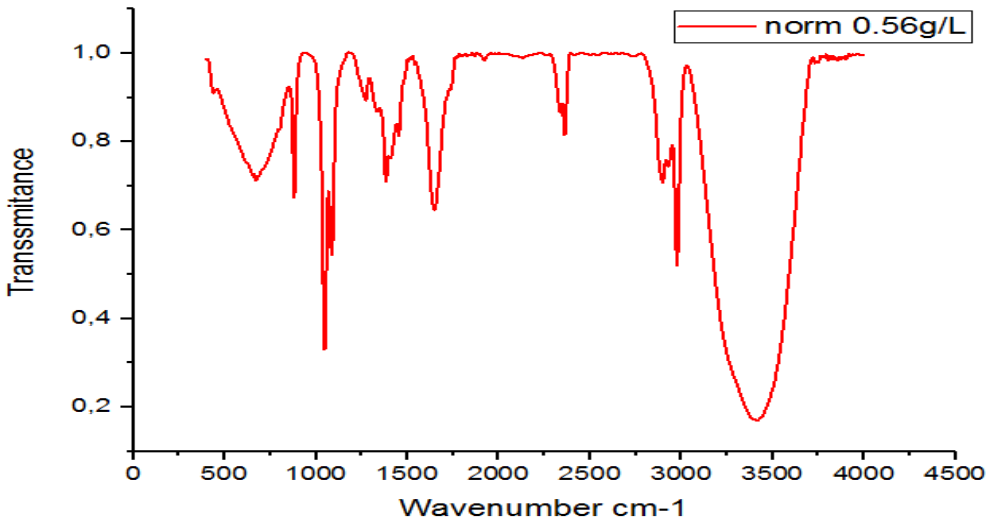

Figure 19:FT-IR Spectrum of basic fluid (Ethanol) with polymer (10mL) +20mL of Silver nitrate

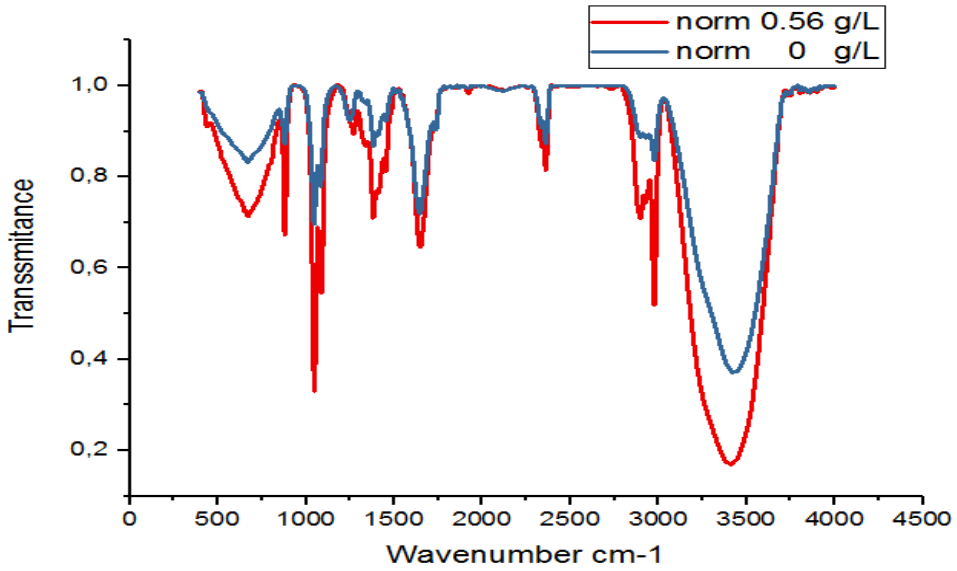

Figure 20:FT-IR Spectra of basic fluid (Ethanol) with polymer (10mL) (0g/L) and fluid (Ethanol) with polymer (10mL) +20mL of Silver nitrate (0.56g/L)

1. 2. 2. UV–Visible spectroscopy

UV–Vis spectroscopy was used to characterize the optical properties of the prepared colloidal silver dispersions and to follow the reaction process. Absorption spectra were recorded in the range of 400–800nm using an UV-3100 selecta spectrophotometer with quartz cuvette. The solutions prepared at MW irradiation in 300W powers. The blank solution was prepared by dissolving 0.4104g of latex copolymer in 40 ml of ethanol.

The Figure 21 shows the absorbance as a function of the wavelength (λ). We see three spectra with different Silver nitrate concentrations. The visible color change can give information about the formation of Silver nanoparticles which is obvious to prove by the measurement of UV-Vis spectra. A phenomenon will occur; it is the surface plasmonic resonance of the electrons of the nanoparticle appearing in the form of bung in the UV-visible spectrum. The position of this plasmon band and the width at half height (FWHM) gives a strong information of the sizes of the nanoparticles. The size distribution of the particles as shown in the figures of SEM and TEM also can be obtained by the width at half height (FWHM) the Figure 23. The synthesis of nanoparticles under microwave irradiation for 50s gives a solution yellow. This translates that the sizes of the nanoparticles are very small which give Surface Plasmon Resonance bands (SPRs) included in the range of 300 to 500nm with a peak positioned at about 410-420 nm [11-13].

Figure 21 shows UV-Vis absorption spectra of Silver nanoparticles produced at different concentrations of Silver nitrate (0.26g/L, 0.38g/L, 0.51g/L) there is an observation of the bungs of localized Surface Plasmon Resonance (LSPR).

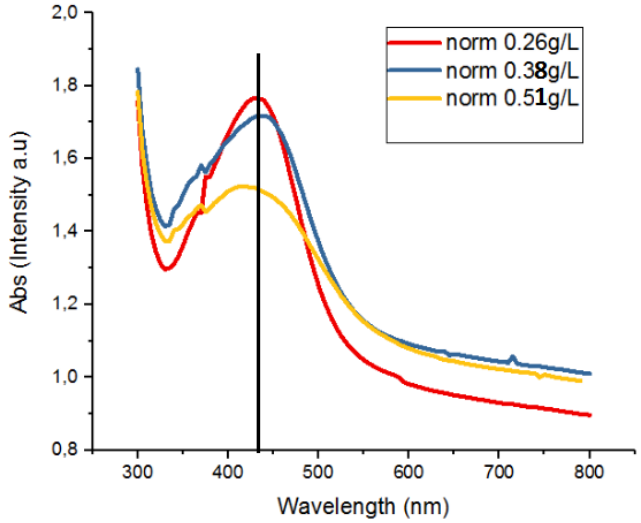

Figure 21:UV–Vis absorption spectra of Silver nanoparticles prepared at different concentration of Silver nitrate (AgNO3) and MW power of 300 W and MW heating time is 50s.

The objective of this synthesis is to have suspended nanoparticles of controlled sizes, at the same time, the effect of the concentration on the sizes of the nanoparticles formed, which is obtained in the figure (The higher the concentration, the lower the absorption [10]. The curve on the right shows the position of (SPR) as a function of the concentration of silver nitrate and the width at half height as a function of the concentration. It is observed that the higher the concentration increases with width and height with a peak position of (SPR), it may be due to the size of the nanoparticles formed.

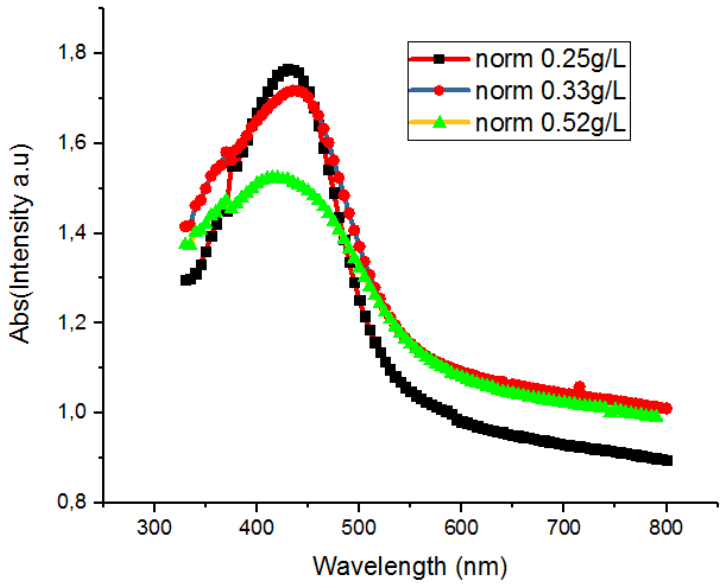

Figure 22:UV–Visible normalized absorption spectra of Silver nanoparticles prepared at different AgNO3 concentration

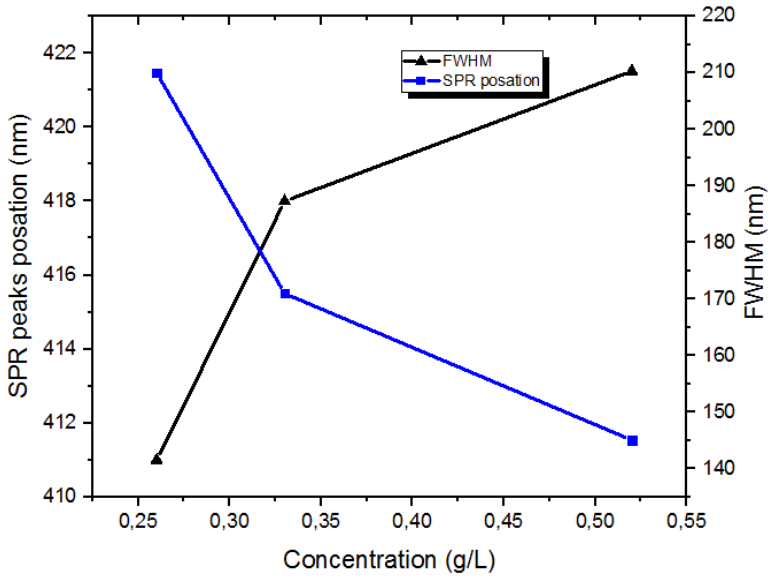

Figure 23: SPR position and FWHM as a function of concentration

1. 2. 3. SEM characterization

Figure 24 ((a), (b), (c), (d), (e), (f)) shows microphotographs of the scanning electron microscope (SEM) of Silver-latex structures synthesized at different concentrations under the MW irradiation at 300W for 50s. These micrometer-scale images show particles that are spherical in shape and are scattered in a micron-scale space (5-20 μm), and thus microparticles of the latex are observed [10]. the resolution of the microscope is too weak to observe Silver nanoparticles due to Silver nitrate

concentration ($AgNO_3$) is low (0.23g/L for micrographs (a), (c), (e) and 0.51g/L for micrographs (b), (d) (f)). The microparticles of the latex increase with the increase of the irradiation time MW [9] [10], and therefore in this case also increase with the concentration of Silver nitrate. On the other hand, the size distribution of the microparticles is not standardized.

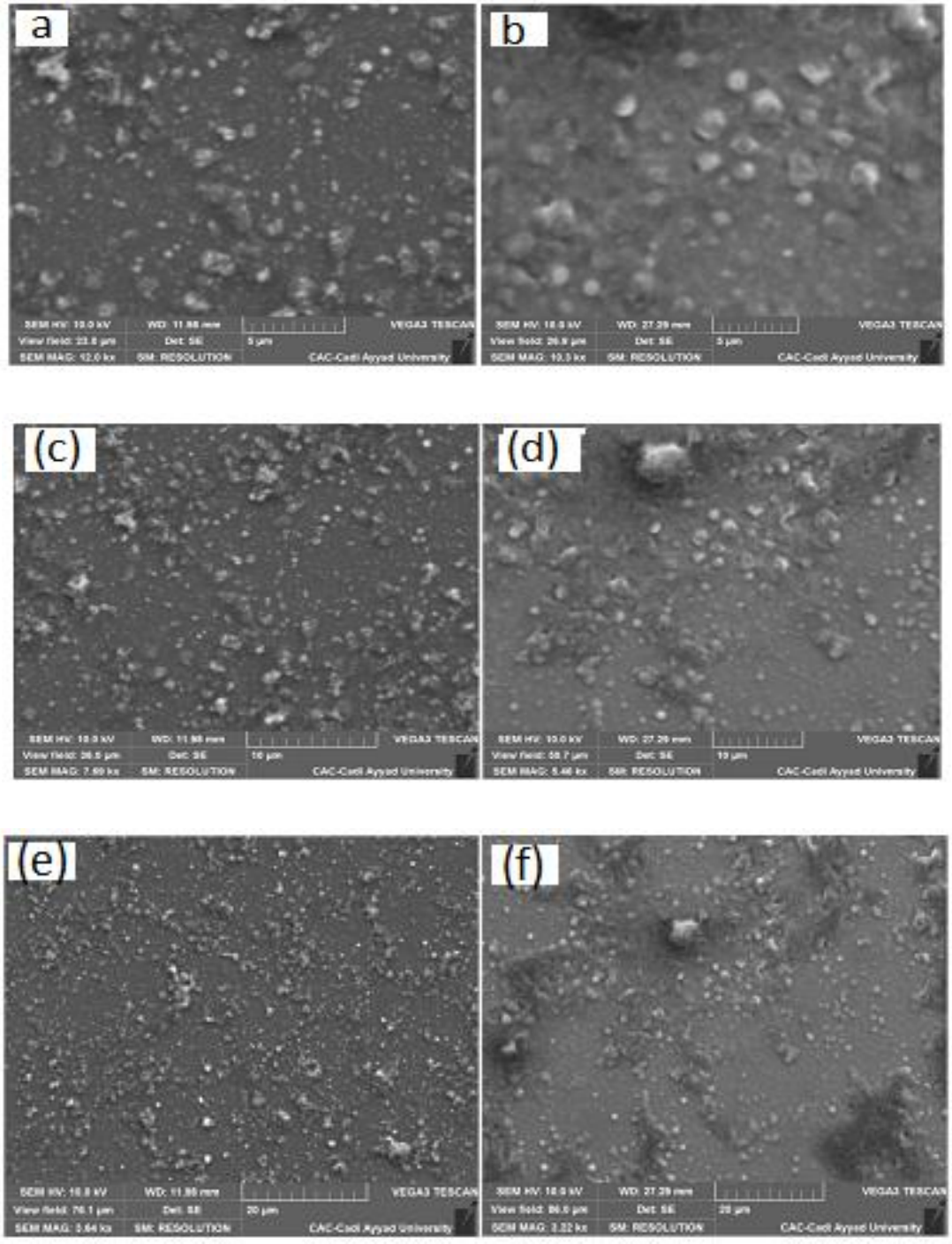

Figure 24:SEM images of Silver nanocomposites, the lift images correspond to 0.26g/L concentration at 5, 10 and 20 resolutions (a, c, e), the right images correspond to 0.51g/L at same resolutions (b, d, f)

1. 2. 4. TEM characterization

To obtain a good precision of the size of the synthesized Silver nanoparticles, the transmission electron microscope (TEM) was made figure 25 for the 0.51g/L concentration sample. In the image, the nanoparticles are of spherical shapes and non-uniform sizes of average value 15 nm as shown by the histogram illustrated by the image obtained.

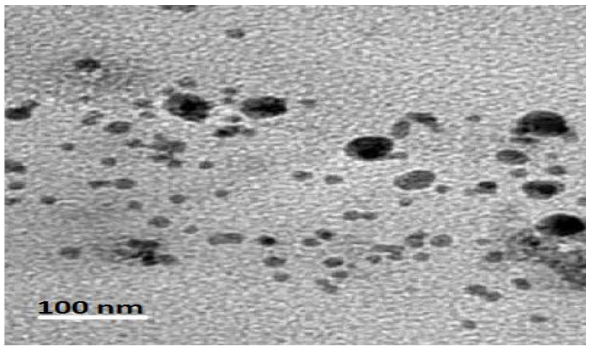

Figure 25:TEM image of round Silver nanoparticles at 0.51g/L concentration with 100 nm resolution

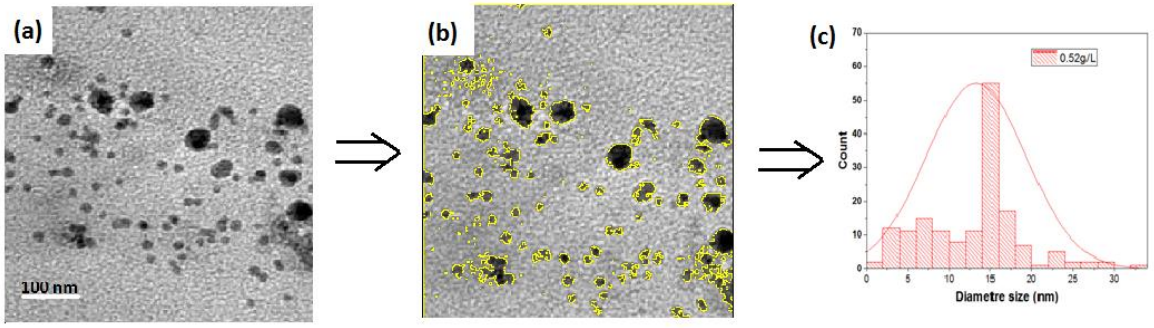

Figure 26:TEM image (a); adjust TEM image with imageJ logicial (b) and histogram distribution (c) count particles as function diameter size

1. 2. 5. EDX Energy Diffusive X-ray Characterization

The formation of silver nanoparticles is confirmed with Energy Dispersive X-ray (EDX) Analysis figure 27. The figure shows in vertical the intensity of X-ray and the horizontal represents the energy (Kev). We observed in spectrum twelve peaks for nine elements are (Ca, O, Na, Mg, Al, Si, Cl, and Ag) two of the metallic Ag are located at 2.9 and 2.8 Kev. Silicon and oxygen was detected because the substrate used of the sample is on the Silicon oxide.

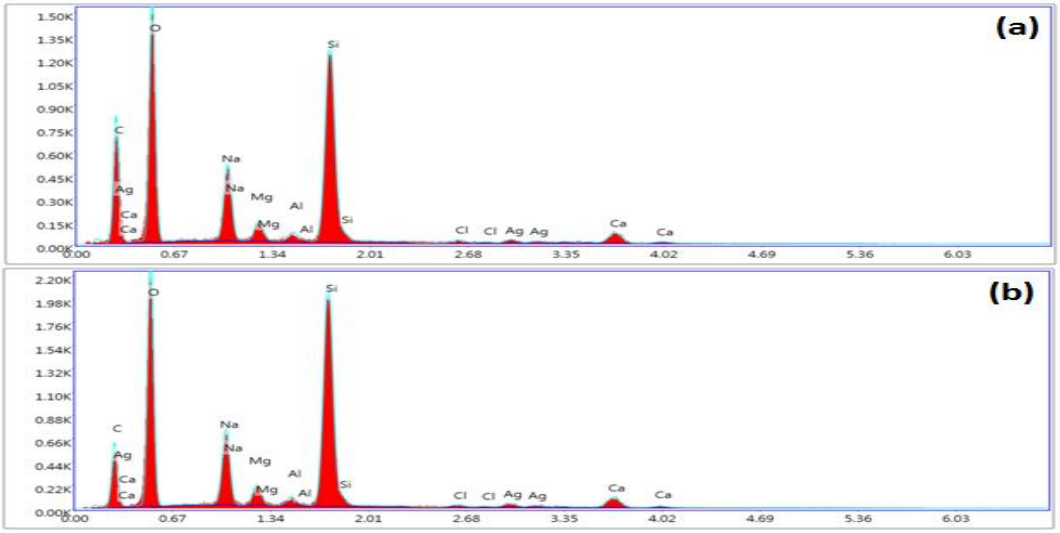

Figure 27:Energy dispersive X-ray analysis (EDAX) spectrum of silver nanoparticles synthesized at deferent silver nitrate concentration(a) for 0.26 g/Land (b) of 0.51g/L

The table II.2 show the Weight % and Atomic % of the composition element in the analysis samples at deferent concentration Weight % (0.25g/L ⇔ 2.09 % and 0.52g/L ⇔ 2.53%) correspond Atomic % (0.25g/L ⇔0.35% and 0.52g/L ⇔0.45%). We are observed deferent values for those two samples it means the concentrations used of the silver nitrate are deferent.

Table II. 2: Represent the weight percent and atomic percent of elements composition in the analyzed samples at deferent concentration (a) correspond 0.25g/L and (b) correspond 0.52g/L

(a)

Element	Weight %	Atomic %
C K	24.10	36.36
O K	31.58	35.76
NaK	8.76	6.90
MgK	1.95	1.46
AlK	0.89	0.60
SiK	24.25	15.65
ClK	0.67	0.34
AgL	2.09	0.35
CaK	5.72	2.58

(b)

Element	Weight %	Atomic %
C K	15.49	24.96
O K	33.97	41.08
NaK	9.51	8.00
MgK	2.23	1.78
AlK	0.95	0.68
SiK	28.93	19.93
ClK	0.61	0.34
AgL	2.53	0.45
CaK	5.77	2.79

2. Effect of Silver nanoparticles on Gap energy of nano-Composite based on MWCNT

After the synthesis of the silver nanoparticles by the method mentioned above, 2mL of each concentration (0.26 g/L, 0.33g/L, 0.52g/L) were added to 3 flasks containing 30mL of Ethanol and

1g of Multi Wall Carbon Nanotube MWCNT and with a hydrothermal autoclave in four at 60°C mixtures were heated.

Characterization by UV-visible led us to determine the variation of the gap energy as a function of concentration by which the nanostructures based on MWCNT were doped, figure 28 (a) represents the square of (ahv) as a function of the energy of the photons in order to determine the gap energy [15], figure 28 (b) represents the gap energy as a function of concentration of the doping sample which shows the decrease of gap with the increase of the concentration.

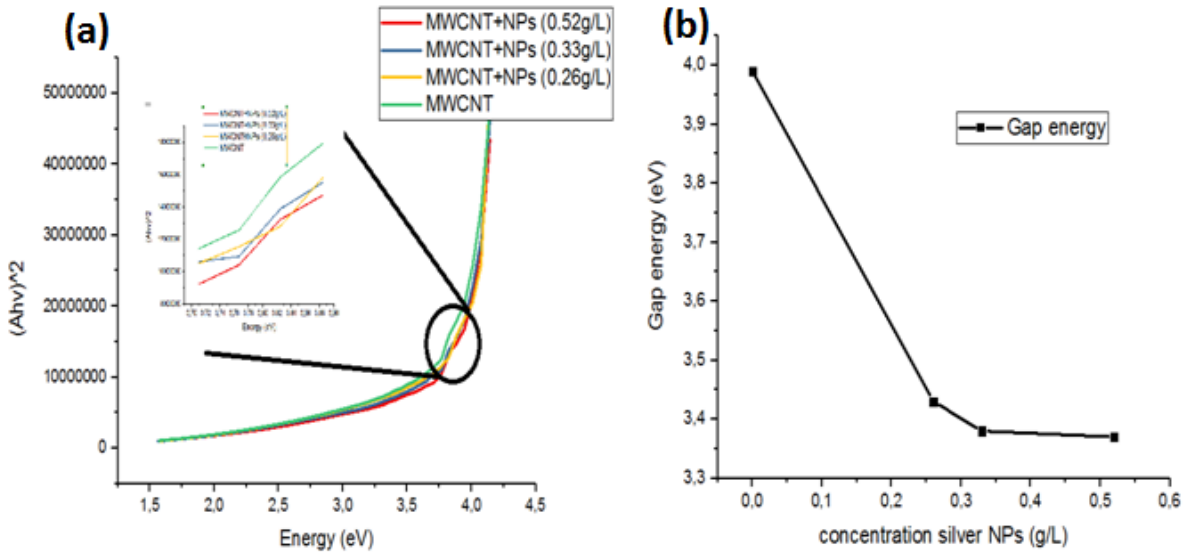

Figure 28: The variation of the dependence (ahv)2 as a function of photon energy (Eph) (a) and gap energy as a function of concentration silver nanoparticles.

CONCLUSION

The new synthetic method of silver nanoparticles based on industrial latex with the presence of a very strong pressure using microwave irradiation. This method of synthesis is very fast and gives us a time advantage which implies energy saving. In addition to that this method is very effective because it allows to have very small nanoparticles. This process has been the subject of a patent registered internationally [14]. We studied the effect of silver nitrate concentration on morphology and size distribution as well. The control of the size of the nanoparticle is possible by the variation of the concentration of the precursor or by the variation of the concentration of suspension polymer and the irradiation time [9,10]. The characterization by UV-visible helped us to have a prediction of size which is confirmed by the TEM characterization.

The doping of MWCNT by silver nanoparticales generate an increase the gap energy, which gives us an important vision of the variation of this gap during the drought of these samples which we can use in the photovoltaic field.

Reference

[1] P. Warrier, ATeja. Effect of particle size on the thermal conductivity of nanofluids containing metallicnanoparticles.2011,6:247.
[2] Ivan Sondi and Branka Salopek-Sondi. Silver nanoparticles as antimicrobial agent: a case study on E. coli as a model for Gram-negative bacteria. 275 (2004) 177–182
[3] G. Schmid (1992). Chem. Rev. 92, 1709.
[4] M. G. Bawendi, M. L. Steigerwald, and L. E. Brus (1990). Annu. Rev. Phys. Chem. 41, 477.
[5] W. A. Deheer (1993). Rev. Mod. Phys. 65, 611.
[6] S. Joseph and B. Mathew (2014). J. Rec. Sc. Res. 3, 185.
[7] A. N. Shipway, M. Lahav, and I. Willner (2000). Adv. Mater. 12, 993.
[8] H. Q. Jiang, S. Manolache, A. C. Wong, and F. S. Denes (2004). J. Appl. Polym. Sci. 93, 1411.
[9] M. Ider ; K. Abderrafi ;A. Eddahbi, S. Ouaskit and A. Kassiba. Rapid Synthesis of Silver Nanoparticles by Microwave-Polyol Method with the Assistance of Latex Copolymer.DOI:10.1007/s10876-016-1096-6
[10] Ider ; K. Abderrafi ;A. Eddahbi, S. Ouaskit and A. Kassiba . Silver Metallic Nanoparticles with Surface Plasmon Resonance: Synthesis and Characterizations
[11] T. Tsuji, K. Iryo, N. Watanabe, and M. Tsuji, Appl. Surf. Sci. 85 (2002) 202.
[12] C. Murphy and N. R. Jana, Adv. Mater. 14 (2002) 80.
[13] O. Wilson, G. J. Wilson, and P. Mulvaney, Adv. Mater. 14 (2002) 1000.
[14] Saïd OUASKIT, Adil EDDAHBI, Mohamed MOUSSETAD, Rahma ADHIRI, Mina IDER,K. Abderrafi Procédé d'élaboration de nanoparticules métalliques dans une émulsion acqueuse de latex sous l'effet d'irradiation micro-ondes. Numéro de demande: PCT/MA2013/000036 ; Numéro de publication : WO 2014/088383 (12 Juin 2014).
[15] Abdelghafour El Moutarajji, BouazzaTbib, and Khalil El-Hami. Effect of Erbium Addition on Optical and Electrical Properties of Polytetrafluoroethylene :doi.org/10.1007/978-3-030-12065-8_10.

CHAPTRE III:

EFFECT OF SILVER NANOPARTICLES ON ELECTRICAL AND THERMAL CONDUCTIVITIES OF THE GLYCEROL.

1. Effect of Silver nanoparticles on electrical conductivity of the Glycerol

INTRODUCTION

The nanoparticles of the metal objects such as silver, cooper, iron, some metals oxide, Influence the behavior properties of the mediums namely, the thermal conductivity [1,2], Silver nanoparticles as antimicrobial agent [3], the dynamic viscosity [2], And the optical property (Gap energy) [4] of the composts associated. The silver nanoparticles based Nano fluid meet the application in deferent field, such as Microelectronic impressions [5], photo catalytic effect [6-7], optoelectronics [8], heat transfer systems [9], lithography [10], and in the field of biology as bacterial biosensors [4]. Because the silver nanoparticles have one of famous property which is the surface Plasmon resonance (SPR) which allowed to apply in several fields.

The sizes of our silver nanoparticles depend on the method of synthesis and the polymer used for suspension of the nanoparticles [11] (MW-Polyol; Electrochemical; Laser Ablation; Photochemical; Sonochemical; and chemical radiation [11-12]). The advantage of this technology is that it has a very short time in the industrial field. For this, we need a rapid method, among these methods the one mentioned in this work is MW-polyol [11-12]; that has effectiveness of controlling the time of synthesis of size and shape [11-12].

The formation of nanoparticles needs an enormous pressure, which can be generated by a microwave which applies irradiations on the base fluid which is in general a polar fluid ex: (Ethanol, Water) which transforms the irradiated energy to vibrations of the polar molecules and thus a rapid and homogeneous elevation of the temperature and the speed of the reaction.

1. 1. Preparation of Nano fluid NpsAg/Glycerol and experimental setup

After the preparation of the original samples of mass concentration of Silver nitrate (1.287g/L, 1.925g/L and 2.57g/L) in the vials located on the left hand-side of the image. We diluted our original samples 5 times by adding Ethanol to have smaller concentrations of Silver nanoparticles (0.257g/L, 0.385g/L, 0.514g/L) in the vials located on the right of the image, then we took 1mL of each last sample and we put in tubes containing 9mL of Glycerol to finally have our material to be studied in concentration (0.025g/L, 0.038g/L and 0.051g/L).

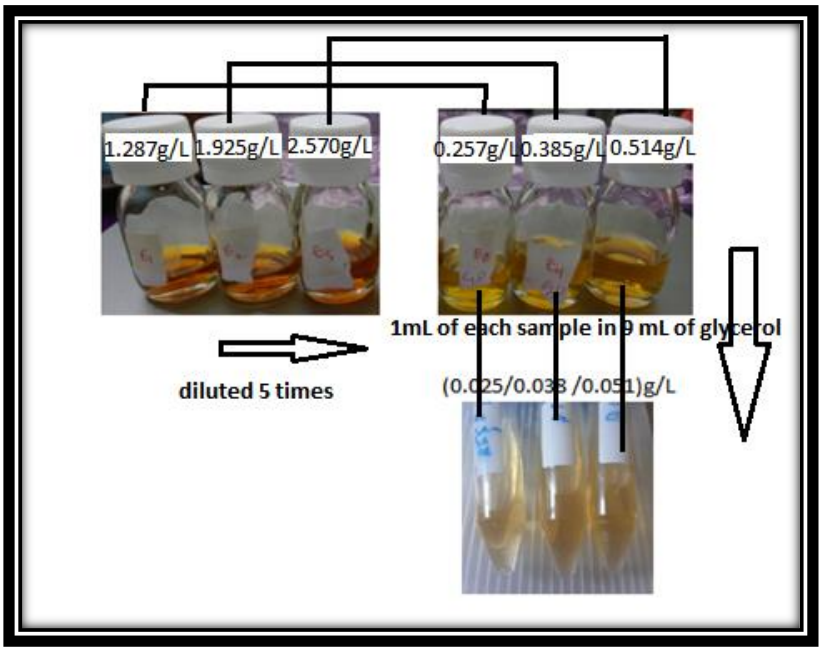

Figure 29:Diagram illustrates the preparation steps of the Glycerol-based Silver nanoparticle nanofluid

1. 2. Characterization, results and Discussions

1. 2. 1. FT-IR characterization of Glycerol and Glycerol with Silver nanoparticles

The infrared spectrum represents the transmittance, the intensity transmitted, counted from 0 to 100%, relative to the intensity of the incident beam, instead of the intensity absorbed. Thus, on the spectrum I.R. the abscise is the wave number (in cm^{-1}) and the ordinate transmittance T expressed as a percentage. A 100% transmittance means that there is no absorption, so in I.R. the absorption bands point downwards. An IR spectrum extends from 400 cm^{-1} to 4500 cm^{-1}. in the wavelength range 3500-2500 cm^{-1}, i.e. the peaks centered at 3294, 2934, 2880 cm-1 are due to the stretching vibrations of the OH groups (Glycerol, Alcohols and Polymers), unbound hydroxyl OH group and elongation of CH bond. and in the range of 1700 to 700 cm^{-1}, the positions of the peaks centered by 1412, 1210, 1108, 1031, 922, 850 cm^{-1} are bung corresponding successively to the deformation of CH_2 and CH_3, stretching of primary alcohol CO and OH alcohols out of plan.

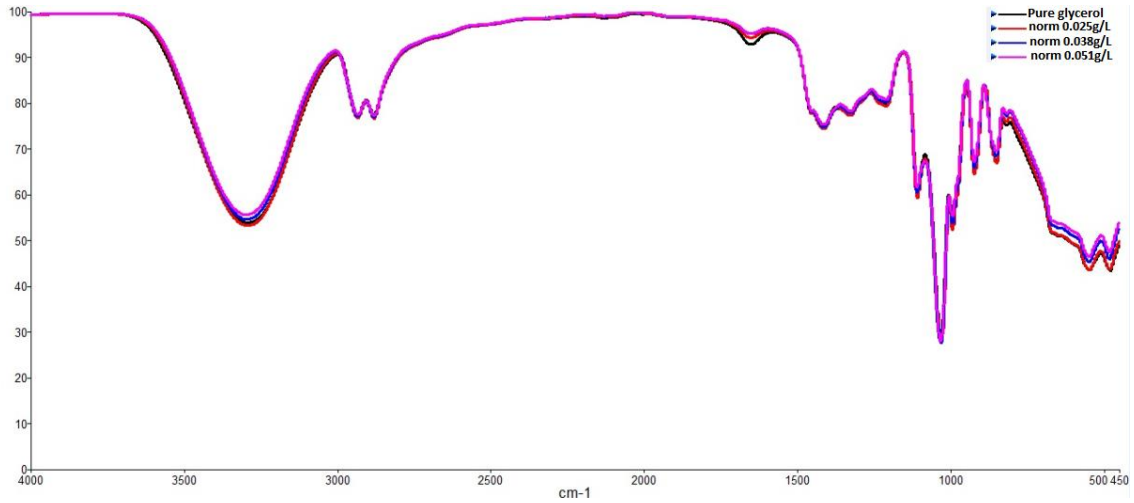

Figure 30:Transmittance FT-IR of Glycerol and Glycerol with various concentration

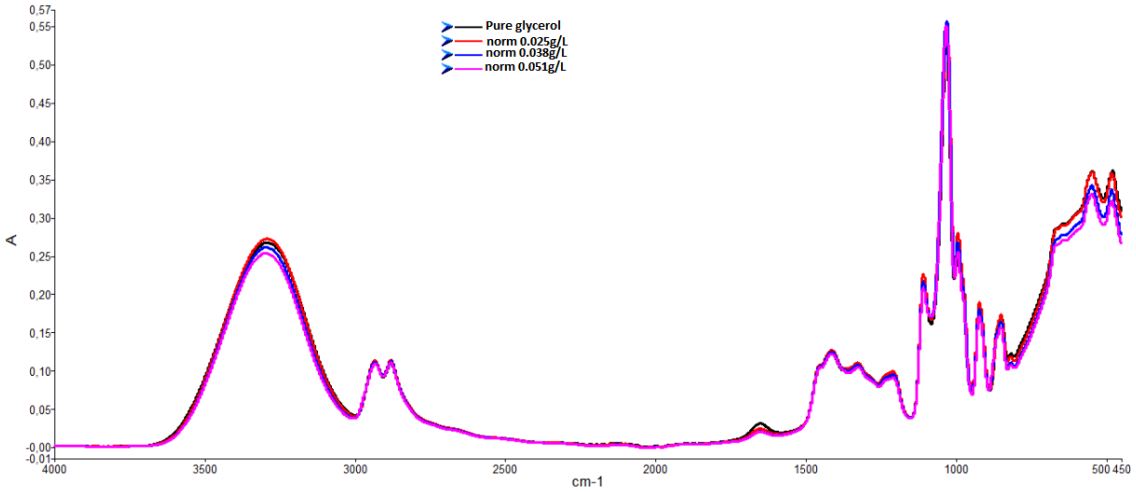

Figure 31:Absorbance FT-IR of Glycerol and Glycerol with various concentration

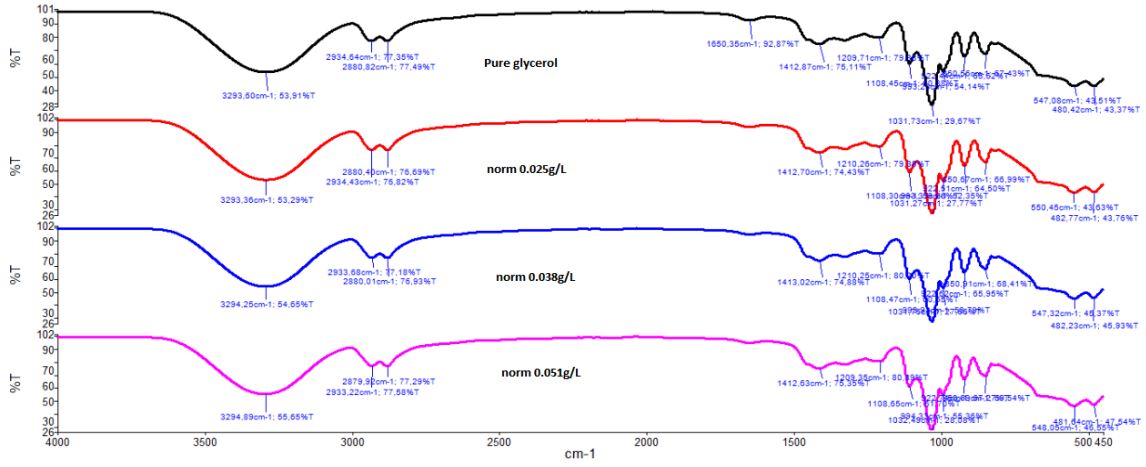

Figure 32:Transmittance TF-IR and position bands of Glycerol and Glycerol with various concentration

The flowing table represents all the bungs that have appeared in the FT-IR spectra with its transmittance values

Table III. 1:Represent the Peak position and transmittance% FT-IR of Glycerol and Glycerol with various concentration of Silver nanoparticles

Peak posation	Transmittance%	**Assignment**
850	67	Alcohol, OH out-of-plane
993	54	
1210	79	Primary alcohol, C-O stretch
1412	75	CH_2 and CH_3 deformation
2880	76	elongation liaison C-H
2933	77	Non bonded hydroxyl group, OH stretch
3294	54	Normal ‘‘polymeric’’ OH stretch

1. 3. Influence of the concentration of Silver nanoparticles on the electrical conductivity of Glycerol

The samples of Glycerol doped with Silver nanoparticles with concentrations of 0.025g/L, 0.038g/L and 0.051g/L. Are subject to the measurement of electrical conductivity. The flow table represent the value of electrical conductivity at various concentration and temperature.

Table III. 2:Represents the electrical conductivity of Glycerol and doped Glycerol

Concentration(g/L)	**Electrical conductivity(µS) at temperature 27°C**	**Electrical conductivity(µS) at temperature 40°C**
0	0,08	0,27
0,025	0,088	0,386
0,038	0,23	0,467
0,051	0,359	0,671

Figure 33 Shows the conductivity of Glycerol and of the doped Glycerol as a function of the concentration of the Silver nanoparticles. We notice that the conductivity of Glycerol increases when the temperature increases, at 27°C the value is 0.08µS on the other hand at 40°C the value

is 0.27µS and the same for doped Glycerol by the different values of the concentration, it means when the temperature increases, the value of the conductivity increases too.

On the other hand, the electrical conductivity increases with the concentration, at 27°C the electrical conductivity takes the values of 0.08µS, 0.088µS, 0.23µS and 0.359µS for pure Glycerol and the concentrations 0.025g/L, 0.038g/L and 0.051g/L successive.

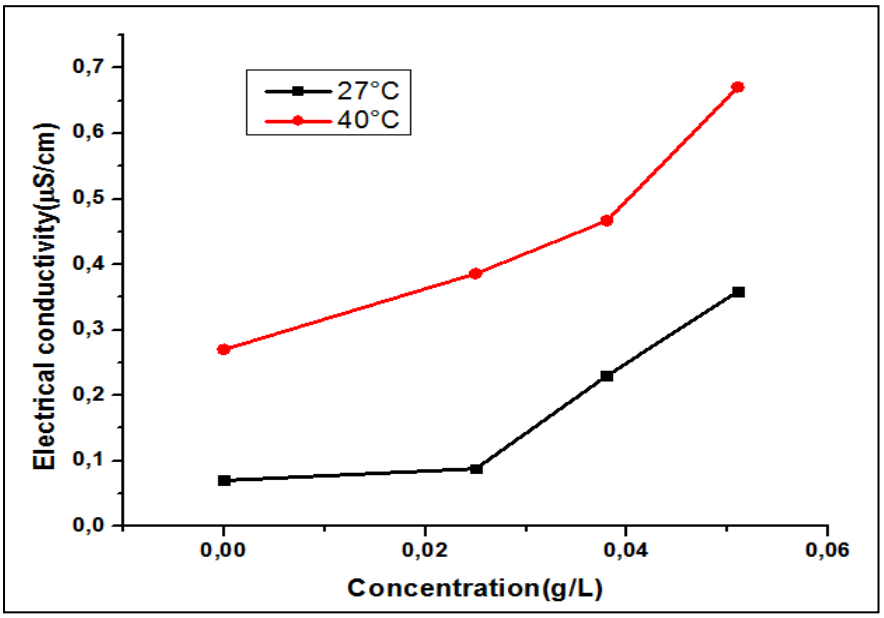

Figure 33:Electrical conductivity according concentration of Glycerol and doped Glycerol

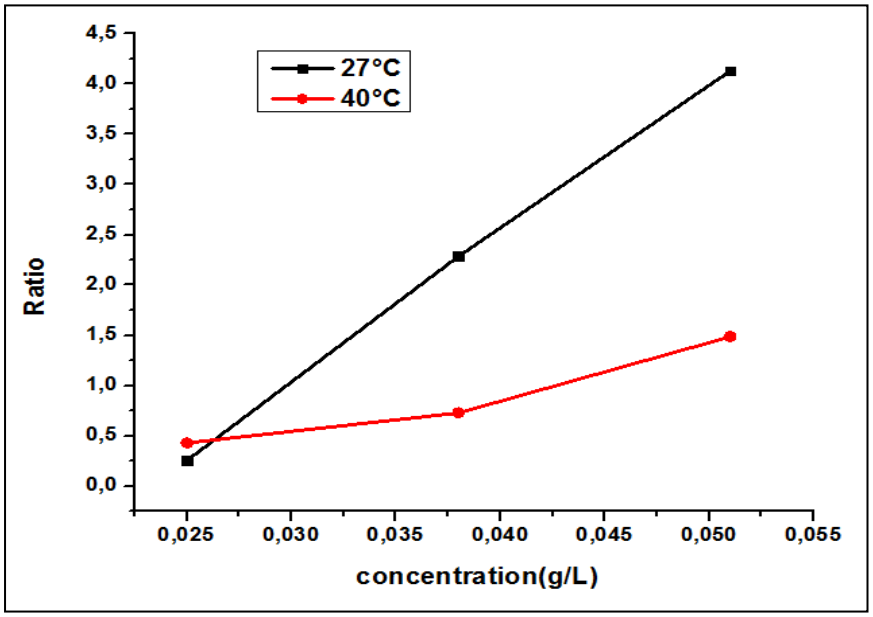

Figure 34:Electrical conductivity ratio according concentration of Glycerol and doped Glycerol

2. Effect of Silver nanoparticles on thermal conductivity of the Glycerol.

INTRODUCTION

In this paragraph, we present the principle and implementation of the transition hot-wire method (THW) based thermal conductivity measurement for characterization of liquids. This is a variant of the transient method which has the advantage of operating with weak excitations, thus limiting the influence of natural convection.

We have adapted this method to the measurement of the thermal conductivity of nanofluids, generally synthesized in small quantities.

We have conducted a detailed study of the limitations of the method in order to estimate the precision of the measurements and to validate the use of such a simple and inexpensive device for the thermal characterization of nanofluids.

Over the years many techniques have been developed to measure the thermal conductivity of liquids. A number of these techniques are also used for nanofluids. We have assembled in figure 35 a classification of the main measurement techniques available today, we mainly distinguish between so called transient methods and quasi-static methods.

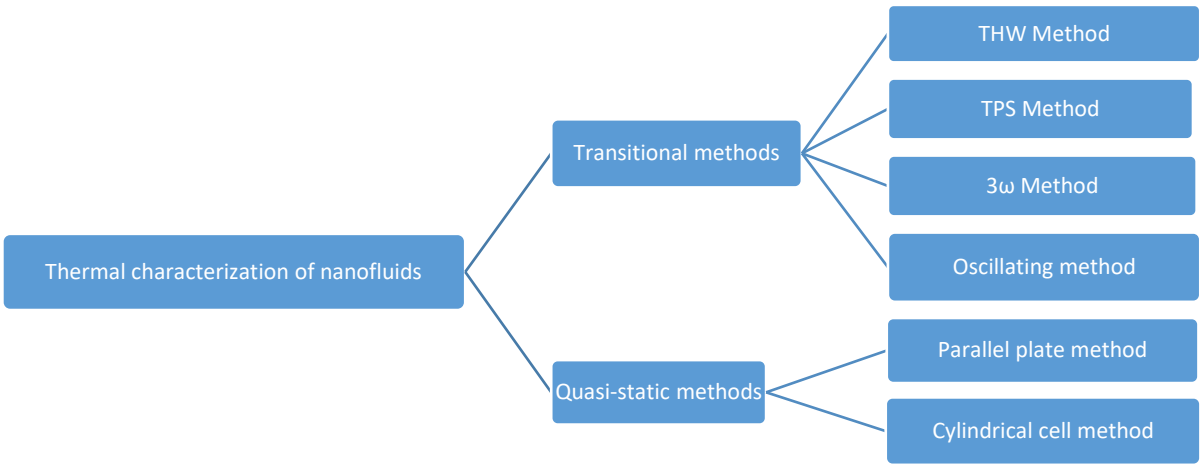

Figure 35:Classification of the main methods of thermal characterization of liquids available today. The figure indicates the preeminence of the method in a ranking based on the number of publications, according to [1]

2. 1. Transient methods

Transient methods use the "sudden" generation of heat in the sample to be characterized by the Joule effect produced in a heating line, usually metallic, placed in thermal contact with the sample. We then measure the rapid1 temporal variation $\Delta T(t)$ the temperature of the heating line which results from this brief thermal excitation, via the variation of its electrical resistance $\Delta T(t)$.

Transient methods have the following advantages:

- They are much faster (a few minutes at most) than the quasi-static methods (up to a few hours), thus making it possible to limit the influence of convection on the measurements;
- They make it possible to determine both the thermal conductivity and the specific heat of the medium to be characterized;
- The heating line can be used both as a thermal excitation source and as a thermometer, eliminating the delicate issues of precise relative placement of the sensor and the heat source. This property even makes it possible in certain very favorable cases to envisage absolute measurements which theoretically do not require calibration of the device;
- The quantities that contain the information are electrical, which greatly facilitates the design of the instrumental device, its interfacing and makes the extraction and processing of data easy;
- No special preparation of the sample is necessary;
- The ranges of thermal conductivity scanned can be important: from 0.01W/mK to 100W/mK.

Obviously these methods also have some drawbacks, few however:

- The heating line must have a very small radius a_1 (compared to the dimensions of the container) which can complicate the installation of the wire and its handling (the current radii are of the order of 10 to 25 μm);
- The length L of the wire should preferably check the relation $L / a_1 \gg 1$ in order to limit errors due to edge effects of electrical contacts and to convection. This constraint is not easy to achieve when one has to characterize very small samples.
- The medium to be characterized must be insulating so that the electric current i(t) which passes through the heating filament does not also pass through part of the fluid. In general, a very thin Teflon or kapton insulating sheath is used. These two materials have the advantage of being fairly good thermal conductors and of introducing very low errors in the determination of the thermal characteristics of the fluid being probed.

We briefly describe three of the six methods recalled in figure 35 We deliberately limit ourselves to transient methods because they are systematically used in recent publications.

2. 1. 1. Hot-Wire method (THW)

The Hot Wire method with constant excitation, better known name THW (Transient Hot Wire), uses a very fine platinum wire which immerses in the fluid to be characterized. A constant electric current is suddenly circulated in the wire, causing there by the Joule effect the release of a constant thermal energy which heats the surrounding fluid. The greater the thermal conductivity of the surrounding liquid, the smaller the temperature rise of the wire. It is this principle that is used to measure thermal conductivity. The experience lasts a maximum of 10-200 seconds, so it's very quick. Platinum wire serves as both a source of thermal energy and a temperature sensor. This method obeys the theory of the heating line developed by Cars law and Jaeger [2] and the temperature variation $\Delta T(a_1,t)$ of the wire of radius a_1 is given in good approximation for times t long enough before $t_\ell = \frac{(a_1)^2}{4\alpha}$ by the relation:

$$\Delta T = \frac{\dot{q}_{DC}}{4\pi\lambda}\ln\left(\frac{4\alpha t}{a_1^2}\right) - \frac{\dot{q}_{DC}\gamma}{4\pi\lambda} \qquad \textbf{(III. 1)}$$

with λ the thermal conductivity of the fluid, α its thermal diffusivity, $\dot{q}_{DC}$ the linear power released by the Joule effect in the platinum wire and γ the Euler constant.

The thermal conductivity λ of the medium in which the wire is immersed can easily be determined using (4.1) from the recording of the instantaneous temperature of the heating wire, provided that the linear thermal power $\dot{q}_{DC}$ is known precisely.

We have shown in figure III.2 the typical shape of $\Delta T = T(a_1,t) - T_0$ as a function of ln (t), in the case of pure water at ambient temperature and pressure, with:

- λ=0,6W. m^{-1}.K^{-1}, ρ=1, 0×103kg.m^{-3}, c=4, 2×103J.K−1.kg^{-1};
- a_1 =25μm;
- L=2cm
- $\dot{q}_{DC}$ =4, 5mW.

By determination, the coefficient α of the equation $\Delta T = T(a_1, t) - T_0 = \alpha \ln(t)$ we can calculate the thermal conductivity with relation **(III. 1)** .

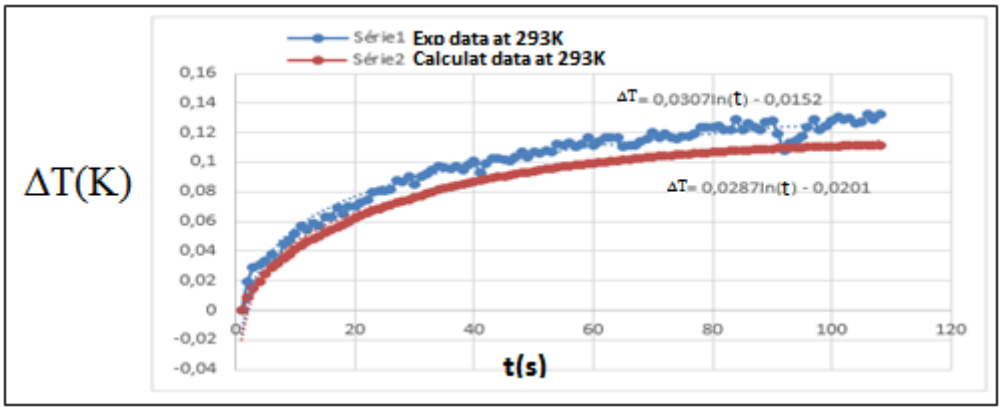

Figure 36:(Blue) represents experimentally the temperature variation of the wire as a function of time immerged in pure water at 290K. (Brown) represented by simulation of the variation of the temperature of the wire as a function of time for pure water at 290K

By applying the precedent relation, we find the values of thermal conductivity for pure water in the case of our experience and in the case of simulation:

$$\lambda_{\exp} = \frac{\dot{q} D_C}{4\pi L \alpha_{\exp}} = \frac{4.5*10^{-3}}{4\pi * 0.02 * 0.03} = 0.59 W.m^{-1}.K^{-1}$$

And calculate value $$\lambda_{cal} = \frac{\dot{q} D_C}{4\pi L \alpha_{cal}} = \frac{4.5*10^{-3}}{4\pi * 0.02 * 0.028} = 0.6 W.m^{-1}.K^{-1}$$

We have shown in figure 37 the block diagram of an assembly used to excite the heating wire and determine its temperature variation $T(a_1, t)$. Usually, an acquisition card connected to a computer is used to acquire and process the information signals. It is now possible to find such thermal conductivity probes marketed by manufacturers. Unfortunately, they are very expensive compared to the relative simplicity of the sensor and are often poorly suited to the characterization of small quantities.

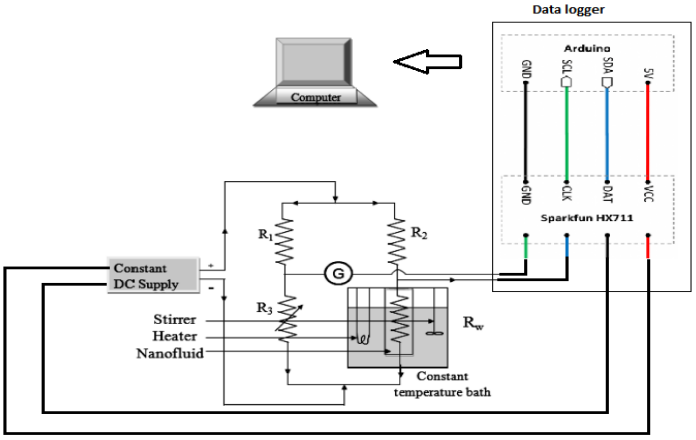

Figure 37:Transient hot-wire set-up for measuring the thermal conductivity of nanofluids

2. 1. 2. 3ω method

The 3ω method is another variant of the transient method which this time uses a harmonic electric current $i(t) = Icos(\omega_0 t)$ rather than a constant current as in the THW method. With modern detection means (synchronous detection amplifier, instrumentation amplifier, harmonic analysis,...) This method allows the use of low amplitude excitation currents, thus limiting losses by thermal radiation, as well as the influence convection in the liquid and the appearance of non-linear phenomena of self-heating of the liquid and the heating wire. The harmonic current $i(t)$ generates by Joule effect within the filament a thermal power of pulsation $\omega = 2\omega_0$ which itself generates a variation of the temperature of the wire, and therefore of its electrical resistance, each comprising a component of pulsation $2\omega_0$. Finally, the electrical voltage across the wire will have a very weak harmonic component (a few μV) of pulsation $\omega = 3\omega_0$ which contains all the information on the heating process and therefore on the thermal properties of the fluid. It is from the detection of this voltage that the method gets its name.

It was Cahill [3] who first proposed the equations which govern in the 3ω method, the harmonic temperature variation ΔT(t) of a thin heating tape (figure 38) of width 2b, deposited by spraying on an insulating solid substrate.

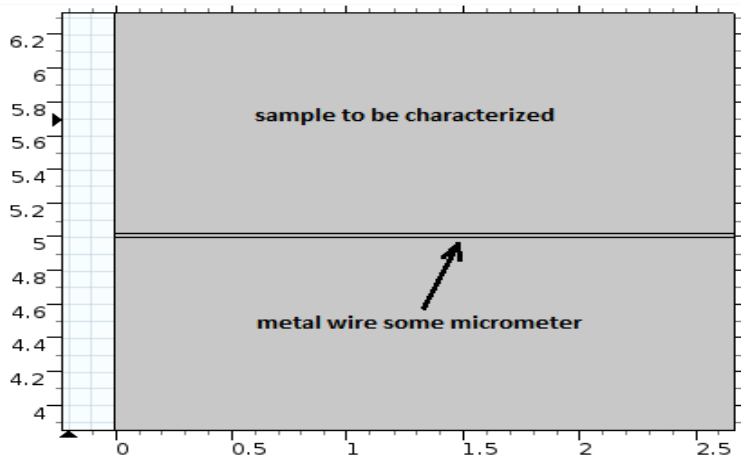

Figure 38:Metal wire 25 µm wide emerged in a semi-infinite fluid to be characterized

Cahill showed that the amplitude ΔT of the temperature averaged over the entire width of the strip is given in the case of the semi-infinite hypothesis by:

$$\Delta T = \frac{P}{L\pi\lambda}\int_0^{inf}\frac{\sin^2(kb)}{(kb)^2(k^2+q^2)^{\frac{1}{2}}}dk \qquad \textbf{(III. 2)}$$

The method has mainly been applied to the thermal characterization of insulating solids and thin films [3, 4, 5, 6, 7, 8, 9].

2. 1. 3. TPS method

The transient plane source method (TPS: Transient Plate Source) is another variation of the transient method which this time uses a heating filament wound in a double spiral (figure 39) which serves as both a temperature sensor and a source of heat. thermal excitation of the fluid. The sensor is protected by a flexible kapton sheath which allows versatile use (liquids, solids, gels, etc.), it must however be entirely immersed in the medium to be characterized.

Figure 39:Probe used in the TPS method to thermally excite the sample and measure the temperature of the heating filament

2. 2. Characterization, results and discussions

2. 2. 1. interface circuit design

we used for the acquisition of analog data a very famous card called arduino uno, which is a very easy to handle interface and is in the market of electronic components and available at a cheaper cost by comparing with others card like DAQ for LabView .... The measuring cell comprises a gold wire 3.5cm in length and 100nm in diameter connected with a Wheatstone resistance bridge, the values of these resistors are 1K. To detect the variation of the potential defernce across the metal wire we used an HX711 amplifier which is compatible with our arduino uno acquisition board. The following figure illustrates all the president descriptions.

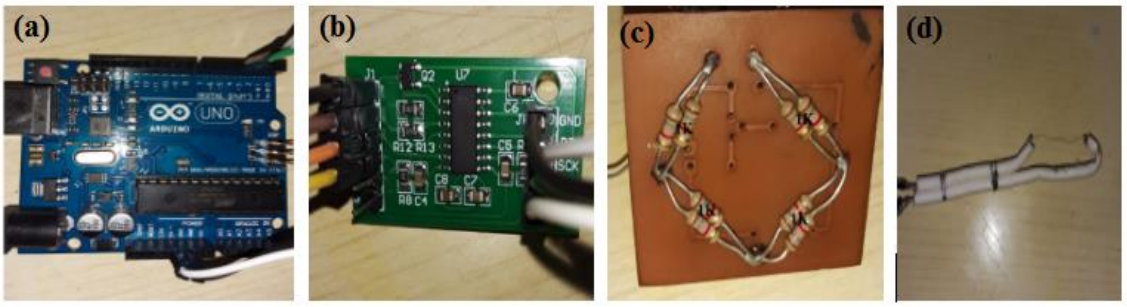

Figure 40:(a) ATMEGA 328P micro controller arduino uno. (b) Amplifier HX711. (c) Wheatstone bridge. (d) Measuring cell

2. 2. 2. Software installation and program code.

The acquisition interface contains an ATMEGA 328P micro controller which sends the signal converted into digital (ADC: Analog digital conversion) to the computer via a USB port with a baud rate of 9600. The code which displays the acquired values is the following:

```
#include "HX711.h"

// HX711 circuit wiring
const int LOADCELL_DOUT_PIN = 2;
const int LOADCELL_SCK_PIN = 3;

HX711 scale;

void setup() {
  Serial.begin(9600);
  scale.begin(LOADCELL_DOUT_PIN, LOADCELL_SCK_PIN);
}

void loop() {

  if (scale.is_ready()) {
    long reading = scale.read();
    Serial.print("HX711 reading: ");
    Serial.println(reading);
  } else {
    Serial.println("HX711 not found.");
  }

  delay(1000);

}
```

The monitor that we took to record the values to be processed is a TeraTerm application compatible with Windows 7. The value obtained in a .dat file that we can convert into an excel file which allows us to plot the variation curves temperature as a function of time

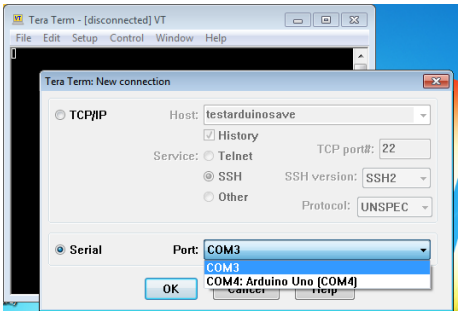

Figure 41:TerTerm settings for Arduino uno

2. 2. 3. Curves obtained

After installing the monitor to record the variation in the potential difference between the terminals of the resistance bridge, we could calculate the temperature variation of the metal wire. figure 42 represents the variation of the temperature as a function of time, it was noted that the variation follows a natural logarithm function which is confirmed by the fitting of the curve and also the value of the logarithm coefficient reduced during the increase of the increase in fraction. Therefore,

the variation in the temperature of the wire decreases more and more with the increase in fraction, which means that the heat exchange varies.

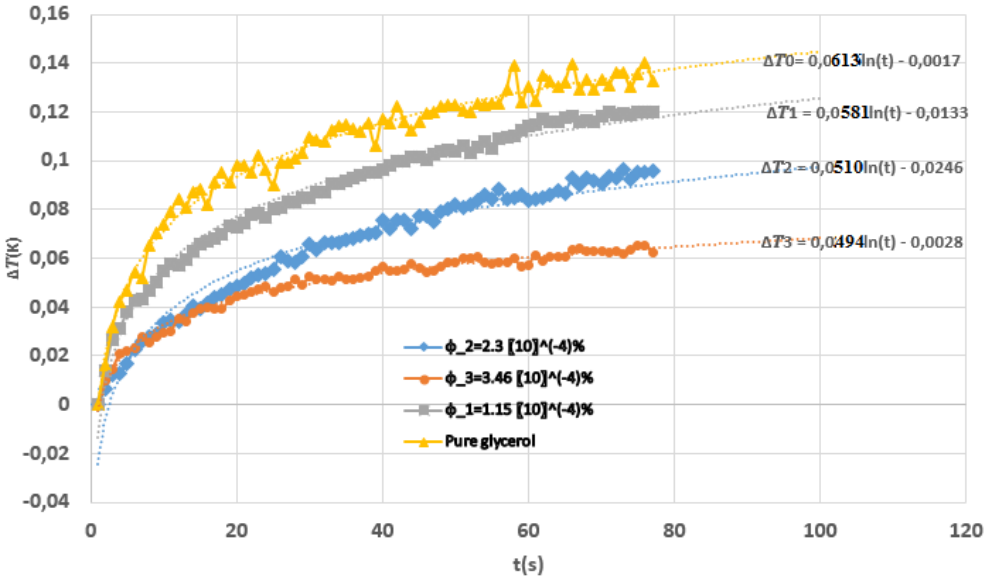

Figure 42:The variation of the temperature of the metal wire over the time of each sample at 290K of various volume fraction

2. 2. 4. Effect of volume fraction on the thermal conductivity

The following table represents the values of the conductivity as a function of the concentration, which is obtained by opting the coefficient of logarithm of time and replacing it in the relation of thermal conductivity shown in paragraph 2 .1 .1.

Table III. 3:The concentration values depend on the concentration of the Silver nanoparticles

Fraction(%)	Pure Glycerol	$1.15\ 10^{-4}$	$2.3\ 10^{-4}$	$3.46\ 10^{-4}$
Thermal conductivity in ($W.m^{-1}.K^{-1}$)	0,292	0,309	0,351	0,363

In the following figure we have represented the values of the table president, we clearly noticed a very strong increase in thermal conductivity, the values of the last one were increased by multiplying times 2 and more.

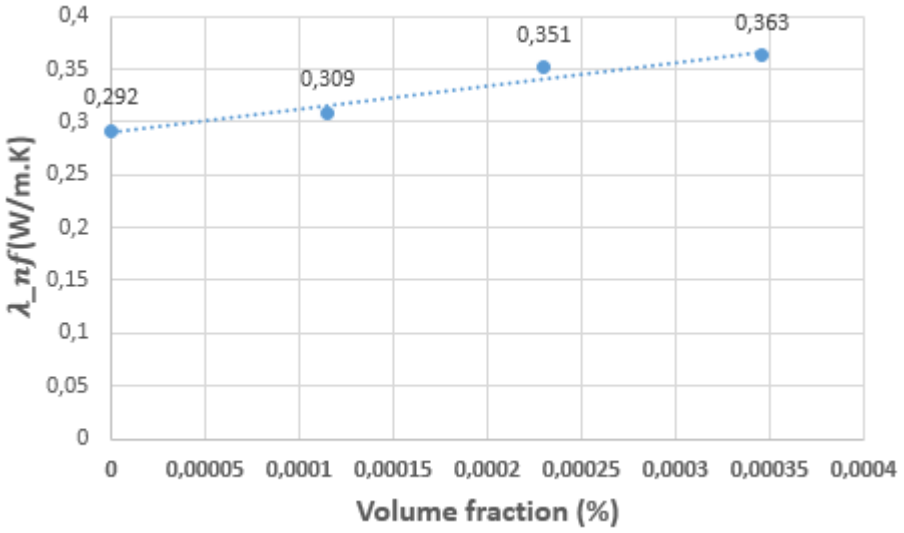

Figure 43:Evolution of thermal conductivity as a function of volume fraction

2. 2. 5. Theoretical models of thermal conductivity

2. 2. 5. 1. Maxwell model

Maxwell's model [10] and its derivatives are probably the most widely used in the literature. This basic model assumes that the particles are spherical, millimeter or microscopic in size, and are dispersed in low concentrations in a continuous matrix. [11]:

$$\frac{\lambda_{nf}}{\lambda_{bf}} = 1 + \frac{3(\alpha - 1)\varphi}{(\alpha + 2) - (\alpha - 1)\varphi} \qquad \textbf{(III. 3)}$$

With $\alpha = \frac{\lambda_p}{\lambda_{bf}}$

2. 2. 5. 2. Hamilton-Crosser model

This model [12], derived from that of Maxwell, incorporates a form factor n to take into account the non-spherical shape of the particles:

$$\frac{\lambda_{nf}}{\lambda_{bf}} = \frac{\alpha + (n-1) + (n-1)(\alpha - 1)\varphi}{\alpha + (n-1) + (1-\alpha)\varphi} \qquad \textbf{(III. 4)}$$

n=3: Maxwell model for spherical particles.

n=6: Cylindrical particles.

2. 2. 5. 3. Bruggemen model

Bruggemen proposed an implicit model which makes it possible to predict the thermal conductivity of nanofluids without limitation on the volume concentration. This model assumes spherical shaped particles [18]:

$$\varphi\left(\frac{\lambda_p-\lambda_{nf}}{\lambda_p+2\lambda_{nf}}\right)+(1-\varphi)\left(\frac{\lambda_{bf}-\lambda_{nf}}{\lambda_{bf}+2\lambda_{nf}}\right)=0 \qquad \textbf{(III. 5)}$$

2. 2. 5. 4. Xuan model

Xuan's model is another extension of Maxwell's law, which this time takes into account the effect of Brownian motion of particles and clusters of particles with a mean radius of gyration r_a [13]:

$$\lambda_{nf}=\frac{\lambda_p+2\lambda_{bf}+(\lambda_p-\lambda_{bf})\varphi}{\lambda_p+2\lambda_{bf}-(\lambda_p-\lambda_{bf})\varphi}\lambda_{bf}+\frac{\rho_p\varphi C_{pp}}{2}\sqrt{\frac{K_BT}{3\pi\eta r_a}} \qquad \textbf{(III. 5)}$$

2. 2. 5. 5. Chon model

A recent model due to Chon [14] incorporates the effect of temperature, particle size, volume fraction, physico-chemical properties of the heat transfer fluid and Brownian motion [15]. This model is to date and to our knowledge the most complete and the most suitable to describe our experimental results:

$$\frac{\lambda_{nf}}{\lambda_{bf}}=1+64.7\varphi^a\left(\frac{d_{bf}}{d_p}\right)^b\left(\frac{\lambda_p}{\lambda_{bf}}\right)^e P_r^d R_e^e \qquad \textbf{(III. 6)}$$

With P_r the Prandtl number of the heat transfer fluid and Re the Reynolds number, here based on the speed of Brownian motion of nanoparticles in the fluid. a, b, c, d and e are dimensionless numbers to be determined for each type of nanofluid.

This model was used by Chon to model the thermal conductivity of the water/Al_2O_3 nanofluid. The values of the parameters a, b, c, d and e found by Chon in this particular case are: a = 0.746; b = 0.369; c = 0.7476; d = 0.9955 and e = 1.2321 [13, 25].

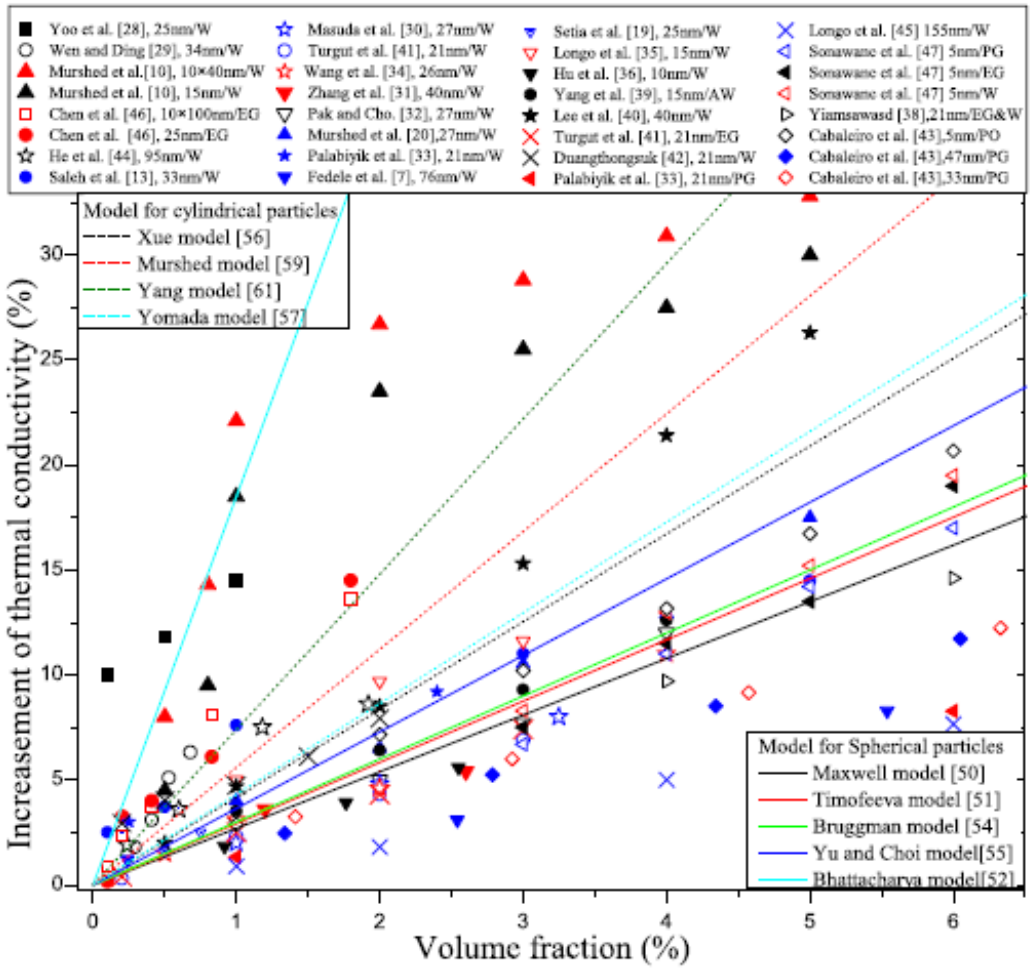

Figure 44:The comparison of various model predictions with experimental data for TiO2 nanofluids at room temperature[16]

2. 2. 6. Experimental and theoretical comparison

Figure 45 represents the modeling of experimental values with Maxwell and Bruggmen, this figure shows that there is a convergence between the experimental values and the models. The model closest to our experimental values is the Maxwell model.

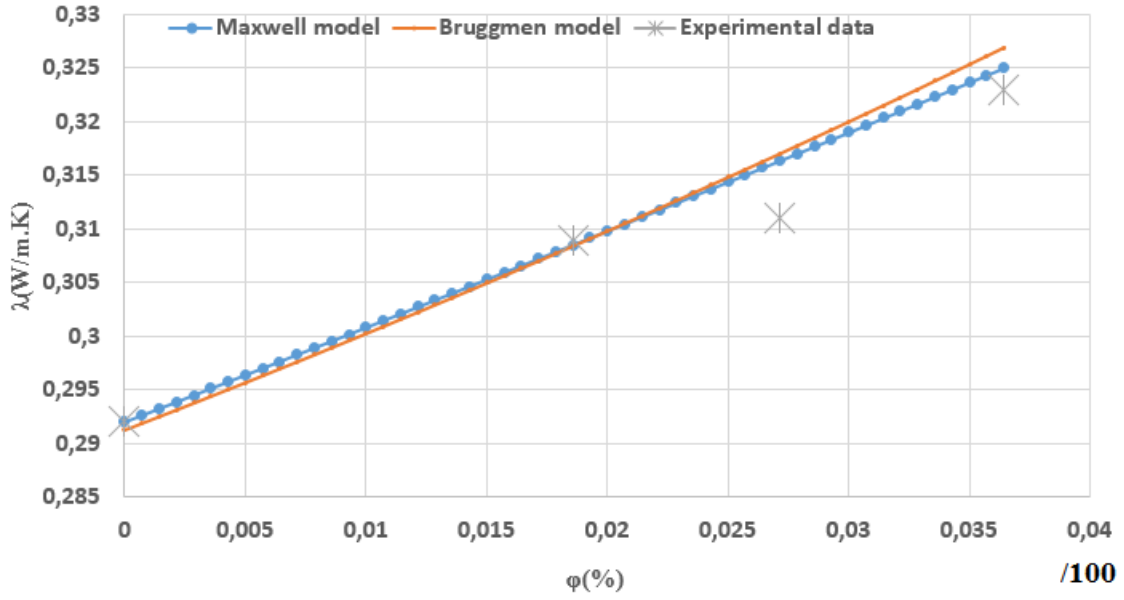

Figure 45:The comparison of thermal conductivity predictions with experimental data and Maxwell and Bruggmen model

when we plot the trend curve of our experimental values we find a linear model as shown in the following figure.

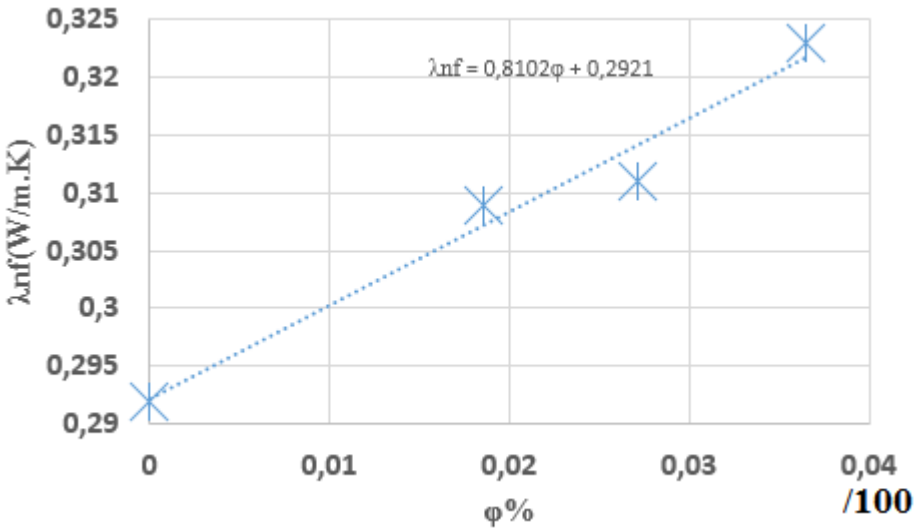

Figure 46:The trend curve of experimental values

CONCLUSION

In this study, the thermal conductivity of SilverNps-Glycerol nanofluids is investigated experimentally. The influence of volume fractions ranging from $1.15\,10^{-4}\%$ to $3.46\,10^{-4}\%$, temperatures at 20°C and nanoparticles sizes of 15nm on the thermal conductivity were presented and discussed. We have noticed the following conclusions from the results:

The experimental results demonstrate that using Silver nanoparticles enhances the effective thermal conductivity of the nanofluids based (Glycerol). However, the effective thermal conductivity of the nanofluid has the same trend as the based fluid (Glycerol) pattern.

The SilverNps-Glycerol nanofluids are stable for at least 24 months after preparation. The possible models for Glycerol-based nanofluids fail to accurately predict the thermal conductivity of SilverNps-Glycerol nanofluids. Therefore, a new empirical correlation has been developed.

References

[1] G. Paul, M. Chopkar, I. Manna, P.K. Das, *Techniques for measuring the thermal conductivity of nanofluids: A review*, Renewable and Sustainable Energy Reviews **14**, 1913 (2010).
[2] H.S. Carslaw, J.C. Jaeger, *Conduction of heat in solids, 2nd ed*, London: Oxford (1959).
[3] D. Cahill, *Thermal conductivity measurement from 30 to 750 K: the* 3*ω method*, Rev. Sci. Instrum. **61**, 802 (1990).
[4] R. Franck, D. Drach, J. Fricke, *Determination of thermal conductivity and specific heat by a combined* 3*ω/decay technique*, Rev. Sci. Instrum. **64**, 760 (1993).
[5] S. Lee, S. Kwun *Heat capacity measurement of dielectric solids using a linear surface heater: Application to ferroelectrics*, Rev. Sci. Instrum. **65**, 966 (1994).
[6] I. Moon, Y. Jeong, S. Kwun, *The* 3*ω technique for measuring dynamic specific heat and thermal conductivity of a liquid or solid*, Rev. Sci. Instrum. **67**, 29 (1996).
[7] T. Borca-Tasciuc, A. R. Kumar, G. Chen, *Data reduction in* 3*ω method for thin-film thermal conductivity determination*, Rev. Sci. Instrum. **72**, 2139 (2001).
[8] A. Jacquot, B. Lenoir, A. Dausher, *Numerical simulation of the* 3*ω method for measuring the thermal conductivity*, J. Appl. Phys. **91**, 4733 (2002).
[9] B. W. Olson, S. Graham, K. Chen, *A practical extension of the* 3*ω method to multilayer structures*, Rev. Sci. Instrum. **76**, 053901 (2005).
[10] C. Maxwell, A Treatise on Electricity and Magnetism. Oxford University Press, Cambridge, UK, (1904).
[11] W. Yu, S.U.S. Choi. The role of interfacial layers in the enhanced thermal conductivity of nanofluids: A renovated Maxwell model. Journal of Nanoparticle Research 5 (2003) 167-171.
[12] R.L. Hamilton, O.K. Crosser. Thermal conductivity of heterogeneous two-component systems. Industrial and Engineering Chemistry Fundamen-tals 1 (3) (1962) 187-191.
[13] R. S. Vajjha, D. K. Das. Experimental determination of thermal conductivity of three nanofluids and development of new correlations. International Journal of Heat and Mass Transfer 52 (2009) 4675-4682.
[14] C.H. Chon, K.D. Kihm, S.P. Lee, S.U.S. Choi. Empirical correlation finding the role of temperature and particle size for nanofluid (Al2O3) thermal conductivity enhancement. Appl. Phys. Lett. 87 (15) (2005) 153107.
[15] H. A. Mintsa, G. Roy, C. T. Nguyen, D. Doucet. New temperature dependent thermal conductivity data for water-based nanofluids. International Journal of Thermal Sciences 48 (2009) 363-371.
[16] L. Yang, K. Du, A comprehensive review on heat transfer characteristics of TiO2 nanofluids, Int. J. Heat Mass Transf. 108 (2017) 11–31.
[17] G. V. Casquillas. Contrôle de température et étude des transferts thermiques dans des dispositifs microfluidiques. These de doctorat, Faculte des sciences d'Orsay, effectuee au Laboratoire de Photonique et de Nanostructures, (2008).

CHAPTRE IV:

EFFECT OF SILVER NANOPARTICLES ON GLYCEROL VISCOSITY

INTRODUCTION

Significant progress in physics and chemistry made it possible, from the end of the 1990s, to the synthesis of particles of nanometric dimensions, which, dispersed in a carrier liquid, constitute nanofluids; their synthesis met the need to improve the thermal diffusivity of coolants by adding a solid phase (metallic nanoparticles) of better thermal conductivity and which remains in stable suspension. The announced increase in the thermal conductivity of these suspensions reached unexplained levels and very different from those predicted by conventional models. This subject has therefore aroused great interest in recent years because it combines fundamental aspects (thermal exchanges at small-scale interfaces) and applied aspects. Regarding this last point, it is necessary to precisely quantify the overall energy balance of the flow of a nanofluid, that is to say, among other things, to know its viscosity because a viscous flow dissipates energy by internal friction to the fluid.

The rheology of nanofluids has given rise to much less research than thermal behavior, and until our time the analysis of the rheological properties of nanofluids remains superficial. The predominance of surface effects and the influence of Brownian motion are the two elements that distinguish a classic suspension from a nanofluid. Both thermally and rheologically, the presence of aggregates and their size will influence the transport properties of nanofluids.

In this chapter we are interested in studying the viscosity of the nanofluids that we have prepared, for different concentrations and different temperatures.

1. fluid rheology

1. 1. Rheological parameters

Rheology studies the flow or deformation of a fluid under the effect of the stresses applied to it. If we consider the fluid in continuous shear flow represented in figure 47, three fundamental quantities make it possible to describe the deformations of the fluid:

• τ: the shear stress expressed in N/m^2.

• $\dot{\gamma}$: The shear rate (or speed gradient) noted in general $\dot{\gamma} = v / d$, expressed in s^{-1}.

• η: The dynamic shear viscosity expressed in Pa.s.

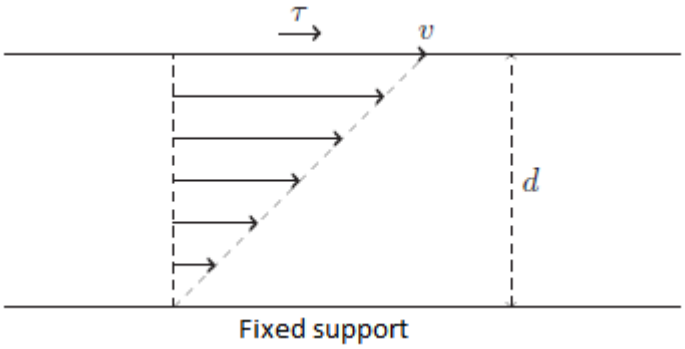

Figure 47:Fluid under continuous shear: v is the speed of the upper fluid blade relative to the fixed support and d is the thickness of the fluid layer considered

In the important case of Newtonian fluids, the dynamic viscosity does not depend on the shear rate $\dot{\gamma}$, it is therefore constant at constant thermodynamic parameters. We can define the dynamic viscosity of a Newtonian fluid by the relation:

$$\tau = \eta \dot{\gamma} \qquad \textbf{(IV. 1)}$$

with η = cste. Many simple liquids like water, certain oils, or glycerol are Newtonians. This model is also suitable for the case of dilute suspensions whose volume concentration in particles does not exceed a few percent. We also define the kinematic viscosity ν is defined by:

$$\nu = \frac{\eta}{\rho} \qquad \textbf{(IV.2)}$$

where ρ is the density of the fluid expressed in kg/m^3.

1. 2. Power dissipated in the fluid by the stress

A viscous flow dissipates mechanical energy by friction internal to the fluid. The mechanical power dP_f dissipated by the elementary force dF = τdS is expressed by:

$$dP_f = d\vec{F}.\vec{v} \qquad \textbf{(IV.3)}$$

We deduce from this the power density dissipated for a Newtonian fluid: $P_f^v = \frac{dP_f}{dxdydz} = \tau \dot{\gamma} = \eta \dot{\gamma}^2$

. The greater the dynamic viscosity, the more mechanical power there is dissipated by the viscous forces within the flowing fluid. In terms of the energy balance of a machine (engine, compressor,...) This loss is harmful and must be limited. It is therefore important to quantify the influence of nanoparticles in suspension on the dynamic viscosity of the nanofluid.

2. Rheological apparatus: Viscometers

A viscometer is a device intended to measure the viscosity of fluids. There are two types of viscometers: “process” viscometers and laboratory viscometers, in our work we are only interested in rotational viscometers.

2. 1. Laboratory viscometers.

Rotational viscometers measure the torque required to rotate a spindle typically immersed in a fluid. The spindle is driven in rotation by a motor passing through a calibrated spring. The resistance to flow will increase with the size of the spindle and/or the speed of rotation. Some are bidirectional measurement with variable speed control. This type of viscometer is not suitable for industry. Indeed, due to the presence of a motor and depending on the frequency of use, the viscosity measurement can diverge quite quickly and regular calibrations are necessary. In addition, with these systems, it is impossible to measure very high viscosity fluids, clogging products, or even fibrous products.

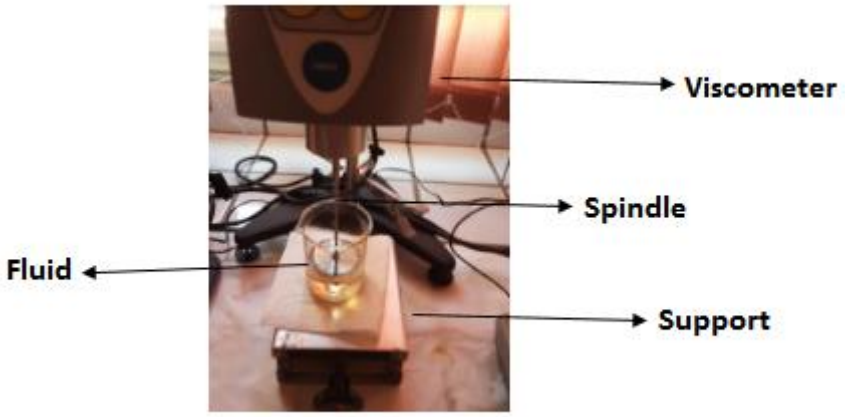

Figure 48:Rotational viscometer

Figure 49:Different spindles of viscometer

2. 2. Couette viscometer

Another type of rotational viscometer is the Couette viscometer: it is composed of two concentric cylinders, the inner cylinder being fixed and the outer cylinder in rotation driven by a motor. Measuring the torque necessary to prevent rotation of the inner cylinder under the effect of the viscosity force of the fluid contained between the two cylinders makes it possible to return to the value of the viscosity of the fluid. The flow between the two cylinders is Couette flow.

3. Rheological laws of suspensions

3. 1. Presentation

In the field of nanofluids, we can distinguish two types of suspensions. A dilute suspension is characterized by a very low volume fraction of solid species. As the particles are very far from each other, no short or long distance interaction disturbs their trajectory. For this type of suspension, the viscosity increases linearly as a function of the concentration of solid elements. Concentrated suspensions, which we have not studied, are characterized by volume concentrations that exceed 50%. The literature contains numerous equations governing the dynamic viscosity of a suspension η from the dynamic viscosity of the host fluid η0 and the volume fraction of solid species φ or C [1].

3. 2. Einstein's Law

Einstein was the first to study the evolution of the viscosity of a dilute suspension as a function of the volume fraction of the solid [2]. He linked viscosity to the dissipation of energy in the suspension by spherical and rigid particles. Einstein finally came to a simple relation valid only in the case of a very dilute suspension (φ≤0.02) of monodisperse spheres [2,3]:

$$\eta_{nf} = \eta_f \left(1+2.5\varphi\right) \quad \textbf{(IV.4)}$$

with $\varphi = \frac{Vs}{Vs + Vf}$ the volume fraction of solid, V_s the volume of the solid phase in suspension and V_f the volume of the host fluid. In order 2 in φ, Einstein's formula is written:

$$\eta_{nf} = \eta_f \left(1 + 2.5\ \varphi + k_2\varphi^2\right) \quad \textbf{(IV.5)}$$

with $5.2 \leq k^2 \leq 6.2$.

3. 3. Laws of concentrated suspensions

In the field of concentrated suspensions (φ>0.5), empirical or semi-empirical relations based in part on Einstein's relation have been developed [2]. In this field, the viscosity of the suspension is no longer essentially governed by the viscosity of the host fluid and the solid volume fraction but

it also depends on the optimal organization of this dry solid fraction, characterized by the maximum stacking compactness. granular φ_m. Three relationships are frequently used in the field of concentrated suspensions (table V.1).

Table IV. 1:Some semi-empirical models of dynamic viscosity for concentrated suspensions

Equation name	Equation
Mooney [2]	$\eta_{nf=}\ \eta_n \exp\left(\frac{2,5\varphi}{1-\frac{\varphi}{\varphi m}}\right)$
Krieger-Dougherty [4]	$\eta_{nf=}\ \eta_n\left(1-\frac{\varphi}{\varphi m}\right)^{-2,5\varphi m}$
Quemada [5]	$\eta_{nf=}\ \eta_n\left(1-\frac{\varphi}{\varphi m}\right)^{-2,5\varphi m}$

4. Protocols and experimental results

4. 1. Aim of the study and reminders on the samples to be studied

The objective of our experimental study is to analyze the influence of the concentration of silver nanoparticles on the viscosity of the host liquid when we change the concentration of nanoparticles of size between 10 and 20nm. The liquid chosen as carrier medium is Glycerol (Glycerol for molecular biology, 99%) in which the nanoparticles can remain in stable suspension thanks to a high viscosity. Different volume concentrations of nanoparticles were used.

during the nanofluid synthesis we used the mass of 0.1541g of silver nitrate which is dissolved in ethanol as detailed in the nanoparticle synthesis chapter (chapter 2). For one of the samples we took 15mL of the solution which contains this mass of silver nitrate (40mL ethanol + AgNO3) which will be added to 40ml of the polymer in the ethanol, i.e. the amount of silver nitrate material taken is n = (m (AgNO3) / M (AgNO3)) * (15/40) = 0.34e-4mol, the same for the amount of silver formed, because a formation of one mole of Ag also requires one mole of silver nitrate. The volume of Silver metal Vs is:

$$Vs=n*V_m=0.34.10^{-4}*10,27=3.49.10^{-3}mL$$

Such as V_m=10.27 mL/mol is a molar volume.

Finally, the fraction of the silver in the mixture is:

$$\varphi_0 = \frac{V_s}{V_s + V_f} = \frac{3.49.10^{-3}}{3.49.10^{-3} + 55} = 6.34.10^{-3}\%$$

The mixture was diluted again with Glycerol to have the following fraction of the Silver nanoparticles:

E_1: $\varphi_1 = 1.15.10^{-4}\%$

E_2: $\varphi_2 = 2.31.10^{-4}\%$

E_3: $\varphi_3 = 3.46.10^{-4}\%$

Figure 50:Samples at various fraction

4. 2. Dynamic viscosity of Glycerol and Ag/Glycerol nanofluid

4. 2. 1. Dynamic viscosity of Glycerol

We measured the viscosity of the host liquid as a function of temperature, using the BROOKFIELD rotary viscometer equipped with a SP6 spindle geometry, PRM=20tours/mim. Glycerol is a Newtonian liquid in the temperature range we have studied (10–50°C). The results are shown in figure 51.

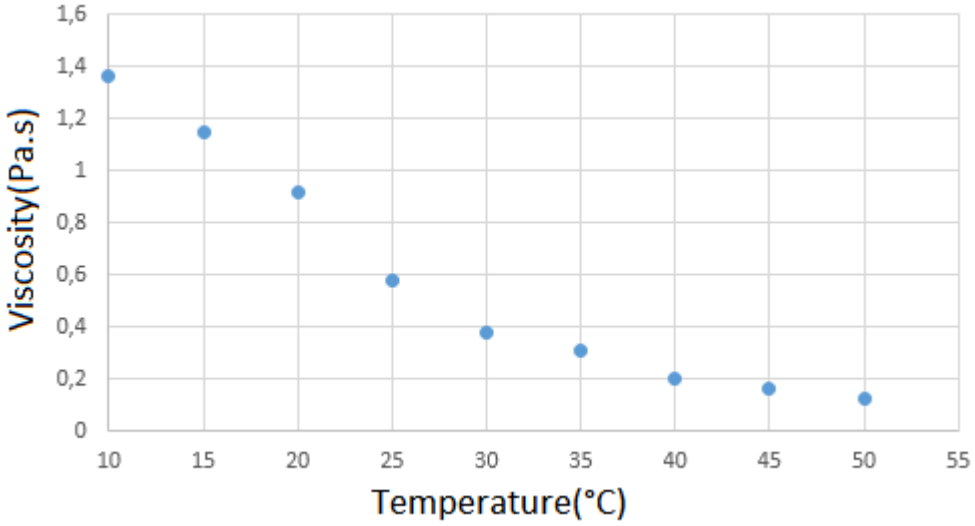

Figure 51:Dynamic viscosity of Glycerol as a function of the absolute temperature T. Measurements obtained for a torque ramp from 6 to 68m.N/rad

4. 2. 2. Dynamic viscosity of the Ag / Glycerol nanofluid

We evaluated the influence on the viscosity of the suspension of various concentrations, which translates into the volume fraction of silver nanoparticles with an average diameter of 15 nm. All the results are shown below for the various volume fractions of nanoparticles that we prepared. For each temperature, the measurements obtained with a stress ramp of 6% Pa to 68% mN/rad show a Newtonian behavior of the nanofluid for any concentration studied. This latter property is commonly observed for dilute suspensions of spherical particles.

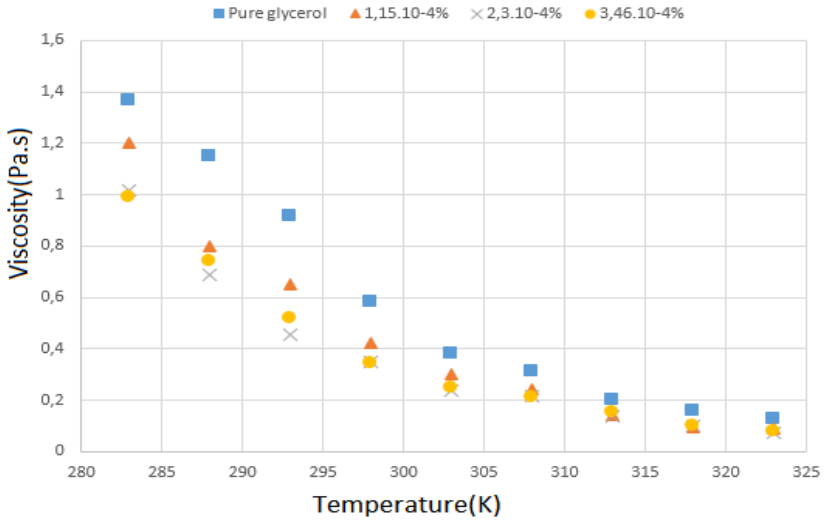

Figure 52:Influence of the volume fraction in nanoparticles on the dynamic viscosity of the Ag / Glycerol-15nm nanofluid with (φ0, 2φ0, 3φ0). Measurements obtained for a torque ramp from 6% Pa to 68%

There are several important results:

The inclusion of nanoparticles considerably reduces the dynamic viscosity of the fluid over the entire temperature range studied. A diminution of about 30% of the viscosity of the fluid is observed for a maximum volume fraction $\varphi_3 = 3.46.10^{-4}\%$. This is a significant reduction which can result in significant internal mechanical losses in the fluid and constitute an advantage for technological applications.

CONCLUSION

Our experimental study of the influence of silver nanoparticles on the dynamic viscosity of Glycerol yielded several important and original results. The inclusion in the Glycerol of spherical nanoparticles of (Ag) in small proportions which are already prepared in an Ethanol matrix with the existence of the polymer considerably modifies the viscosity of the Glycerol, almost 30% decrease for a volume fraction $\varphi_3 = 3.46.10^{-4}\%$. The inclusion of nanoparticles does not change the behavioral law of the host fluid, well described by Chen's model. This observation can reflect the fact that the nanoparticles, in low concentration, do not significantly modify the interactions between the Glycerol particles. The latter therefore imposes its constitutive law as a function of the temperature.

These considerable decreases in viscosity represent a significant advantage in the use of nanofluids with machines such as motors, compressors, ... It is therefore important for the future of such fluids to be able to establish an energy balance that takes these mechanical aspects into account.

References

[1] J.-P. Guillemin. *Rhéologie de suspensions concentrées de matériaux énergétiques recyclables-Modélisation du temps de coulée*. These soutenue a Saint-Etienne, le 25 janvier (2008).
[2] J.P. Guillemin, A. Werckerle, L. Brunet, O. Bonnefoy, G. Thomas.*Application d'un modèle de viscosité à la coulée d'explosifs : Modélisation du temps de coulée*. Rheologie **10** (2006)40-48.
[3] C.T. Nguyen, F. Desgranges, G. Roy, N. Galanis, T. Mare, S. Boucher, H. Angue Mintsa. *Temperature and particle-size dependent viscosity data for water-based nanofluids-Hysteresis phenomenon*. International Journal of Heat and Fluid Flow **28** (2007) 1492-1506.
[4] L. Struble, G.-K. Sun. *Viscosity of Portland Cement Paste as a Function of Concentration*. Advn Cem Bas Mat **2** (1995) 62-69.
[5] A. M. Wierenga, A. P. Philipse. *Low-shear viscosity of isotropic dispersions of (Brownian) rods and fibres; a review of theory and experiments*. Colloids and Surfaces A: Physicochem- ical and Engineering Aspects **137** (1998) 355-372.
[6] R. B. Bird, W. E. Stewart, E.N. Lightfoot. *Transport phenomena, 2end ed.* John Wiley & Sons (2002).
[7] H. Chen, S. Witharana, Y. Jin, C. Kim, Y. Ding. *Predicting thermal conductivity of liquid suspensions of nanoparticles (nanofluids) based on rheology*. Particuology **7** (2009) 151-157.
[8] L.D. Landau, E.M. Lifshitz *Fluid mechanics, 2end ed.* Pergamon Press, Oxford (1987), pp 73-75.

CHAPTER V:

NUMERICAL STUDIES ON GLYCEROL, SILVER AND THEIR NANOCOMPOSITE USING COMSOL MULTIPHYSICS, SURFACE PLASMON AND FDTD METHOD; COMPARISON WITH EXPERIMENTAL RESULTS

1. Simulation of the thermal conductivity with Comsol multiphysics

INTRODUCTION

The COMSOL Multiphysics software is used to calculate the problem of interest to us, namely the heating of a micro-wire of platinum immersed in Glycerol. It is a tool for solving finite element partial differential equations. The modeling of a system such as the one studied here takes place in several stages. The first step is to define the physics "modules" that will be used. In this case, it will be the thermal module "heat transfer in solids and liquids" and the electricity module "Joule heating". The following phases of modeling are common to other physical modeling software. In chronological order, there are:

1. Drawing of the geometry of the system.

2. Choice of different materials in the property library.

3. Setting up of the boundary and initial conditions in each module with the possible coupling of these.

4. Mesh of the elements of the structure.

5. Choice of the solver and the convergence parameters, then resolution of the problem.

6. Post processing of the calculated data (here temperature and electric current).

In the last phase to process the results, there are several tools available to represent any computable physical quantity in the complete model, along a plan, along a line or a point. The quantities represented in 2D can also depend on time if the study is carried out in an unsteady state. We can then process the results directly in the software via the “report” tab or under another software such as Matlab, Exel or OreginePro as in our case. The particular interest of COMSOL lies in the possibility that we have to couple different physical models. It is also possible to work in a steady state and in a transient state. The convergence of calculations in stationary mode is obviously faster. The work that is presented below therefore involves following the different stages of creating a model under COMSOL. One of the most delicate parts of this work consists in introducing the physics and the parameters used during the modeling (equation, initial conditions, boundary conditions, electricity modulus). This point and the associated problems are discussed below.

For this study we approach the problem according to two approaches. In the first case, we are interested in the two-dimensional (2D) modeling of a section of the experimental device. Secondly, taking into account the limitations of the 2D model, the last part of this study is centered on the comparison between the results of numerical simulations and the experimental measurements obtained thanks for this study we approach the problem according to two approaches. In the first case, we are interested in the two-dimensional (2D) modeling of a section of the experimental device. Secondly, taking into account the limits of the 2D model, the last part of this study is centered on the comparison between the results of numerical simulations and the experimental measurements obtained thanks to the experimental device.

1. 1. Numerical modeling:

In this first section, the basic equations and the boundary condition equations used in COMSOL to make numerical simulations are recalled. We then present the main stages of a typical modeling. A sub-section is also devoted to the determination of the convective exchange coefficient.

1. 1. 1. Thermal transfer module:

In a solid, the heat transfer equation is written:

$$\rho C_p \frac{\partial T}{\partial t} - \lambda \Delta T = Q \qquad \textbf{(V. 1)}$$

With:

• ρ the density, in $kg.m^{-3}$

• Cp the thermal capacity, in J/kg.

• λ thermal conductivity, in W/m.K

• Q the term internal heat source, in W.

• T the temperature field, in K.

Conditions to the limits:

• Thermal insulation: $-n.(-k.\Delta T) = 0$.

• Natural convection: heat transfer coefficient by convection h imposed.

• Imposed initial temperature, equal to the ambient temperature ($T_{init} = T_0 = 295.15$ K).

1. 1. 2. Electric module:

The equations solved by the electrical module are:

$$\Delta.J = Qc \quad \textbf{(V. 2)}$$

$$J = \sigma E + Je \quad \text{localized ohm's law} \quad \textbf{(V. 3)}$$

$$E = -\nabla V \quad \textbf{(V. 4)}$$

With:

• J is the density of the electric current, in $A.m^{-2}$

• σ: electrical conductivity, in $S.m^{-1}$

• E: electric field, in $V.m^{-1}$

• V: the electric potential, in Volt V.

• Qc: the source term, in W.

The experimental heating system is modeled by the term internal heat volume source Q and which represents the energy dissipated by the Joule effect in the control volume considered. This energy results from an electric power dissipated by the Joule effect, namely:

$$P = R * I^2 \quad \textbf{(V. 5)}$$

With:

• P the electrical power, in W.

• R the resistance, in Ω.

• I the intensity of electric current, in A.

Boundary condition:

• Electrical insulation: $-n.\ J = 0$

• Density of electric current imposed: $-n.J=J_n$

1. 1. 3. System design and mesh:

In order to represent the heating system used during the experiments, we will simplify the data of the problem by keeping only the characteristic dimensions of the key elements, namely the geometry of the platinum track and the overall size of the substrate.

1. 1. 3. 1. System design

The platinum wire is 25µm in diameter, 2cm long. The sample of the square shape of 2cm per side.

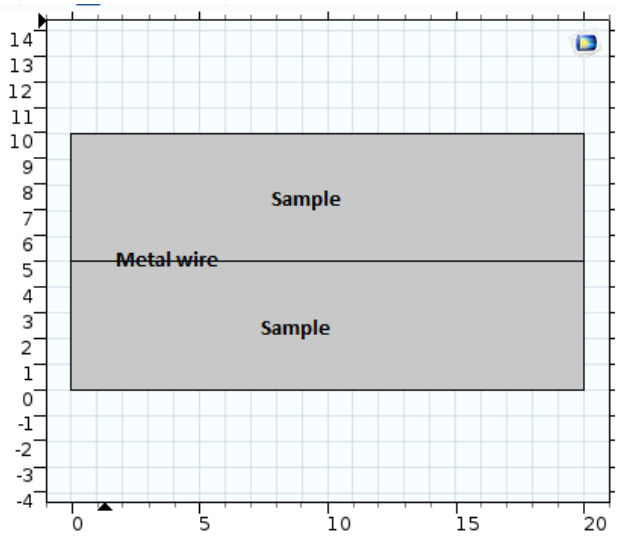

Figure 53:Represents the sample to be characterized with the heating wire.

1. 1. 3. 2. Mesh

the mesh chosen is of fine size at the nanometric scale, the results of these parameters are given by the following figure.

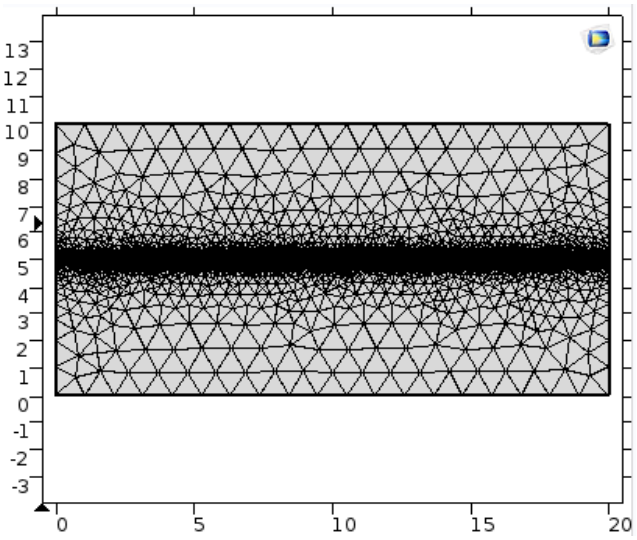

Figure 54:Mesh of system with a fine size

1. 1. 4. 2D simulation results

On the following diagram, we present the evolution of the temperature field in the 2D model. The calculations were made for a linear electric power of 4.5mW/m, which corresponds to the experiment exposed in the part of chapter III. The temperature field was obtained in transient regime at an instant t equal to 100s with the chosen medium is Glycerol.

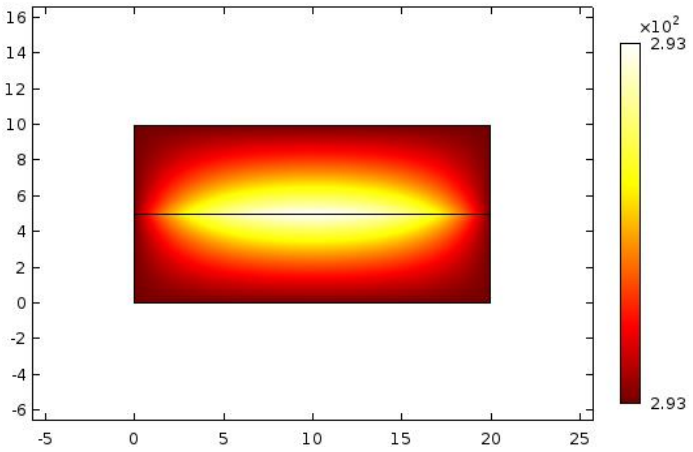

Figure 55:Surface temperature at 100s

To have a good precision of thermal conductivity measurement it is necessary to avoid the effect of convection, and this requires stopping the measurement in a short time as shown by the temperature profiles according to the position obtained with the cutting line.

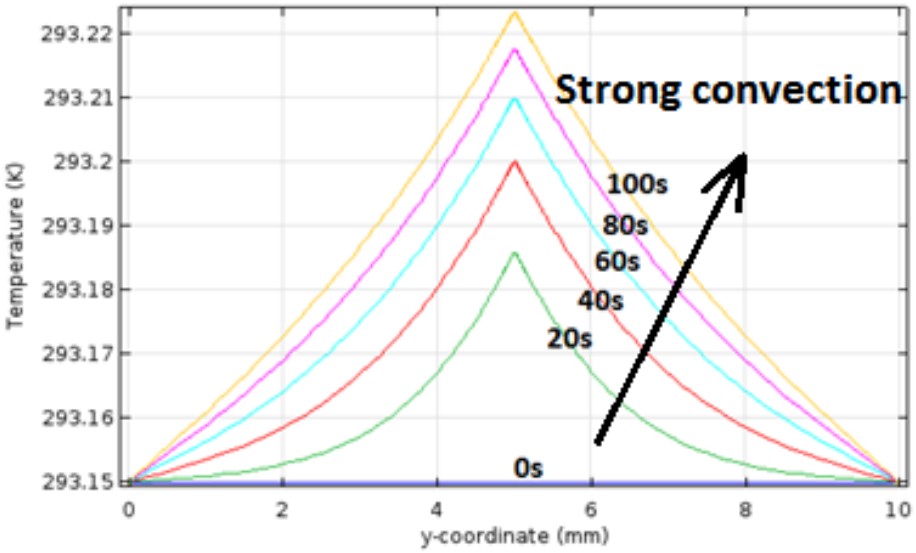

Figure 56:Evolution of the digital temperature field along a section line at 0s, 20s, 40s, 60s, 80s, 100s

1. 1. 5. The temperature variation in the wire

Over time the temperature of the wire increases in a logarithmic manner which is in agreement with the theory of the hot wire, the following figure represents the variation of the temperature of the wire as a function of time.

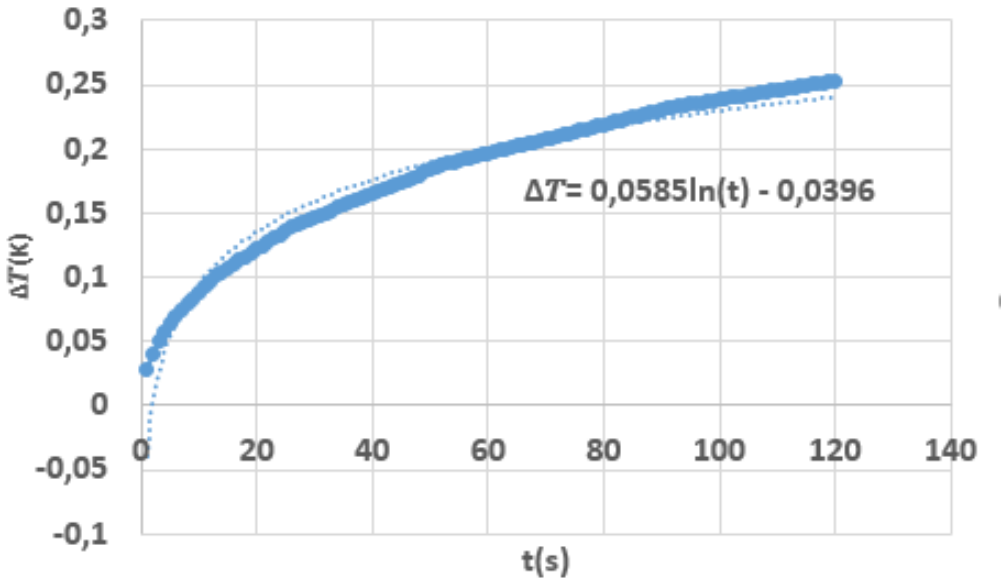

Figure 57:Variation of the temperature of the wire as a function of time.

1. 1. 6. Calculates the thermal conductivity of Glycerol

The values found of the thermal conductivity in all the experimental, bibliographic and simulated are:

The simulation value:

$$\lambda_{cal} = \frac{\dot{q} D_C}{4\pi L \alpha_{cal}} = \frac{4.5*10^{-3}}{4\pi*0.02*0.058} = 0.3W.m^{-1}.K^{-1}$$

The experimental value:

$$\lambda_{\exp} = \frac{\dot{q} D_C}{4\pi L \alpha_{\exp}} = \frac{4.5*10^{-3}}{4\pi*0.02*0.0613} = 0.292W.m^{-1}.K^{-1}$$

The bibliographic value

$$\lambda_{bib} = 0,285W.m^{-1}.K^{-1}$$

2. Simulation of the SPR of nanoparticles by FDTD method

INTRODUCTION

Among the numerical methods used in electromagnetism, the finite difference method in the time domain better known as FDTD is particularly important. It allows you to directly solve Maxwell's equations and acoustic wave equations in time and space for very general situations (nature of the source, inhomogeneous, dispersive, anisotropic, magnetic medium, etc.).

In this chapter we will expose the diagram of Yee which leads to the formulation and the implementation of the FDTD code for the modeling of the structures studied in this work.

2. 1. Time Domain Finite Difference Method (FDTD):

The FDTD method was initially designed for the numerical resolution of differential equations, then it was adapted and widely used in the modeling of electromagnetic problems in the fields of microwaves, telecommunications and detection. It seems particularly suited to the problems of nano-optics where the structures have details less than the wavelength but with dimensions remaining reasonable in relation to this wavelength.

The method of Finite-Difference Time-Domain (FDTD), allows to study in a precise and reliable way many problems belonging to electromagnetism. It is a useful tool for exploring the optical properties of metallic nanoparticles because it allows to model strongly heterogeneous systems, that is to say containing materials with different dielectric functions (dielectric, metal, plasma, etc.) and with complex geometric shapes. Moreover, since it is a temporal method, only one simulation is necessary to obtain the response of the system under study over a wide frequency band via the Fourier transform.

The FDTD method based on the explicit scheme of Yee [1], while the electric and magnetic fields discretized by a scheme of centered finite differences of order two for space and time. This algorithm allows at each time step to calculate the field at any point of the discretized space. The diagram of calculation being entirely explicit, it thus does not require any inversion of matrix and thus it presents a good efficiency of calculation. If the incident field is a pulse, the FDTD can also reproduce in a single calculation the behavior of an electromagnetic wave over a wide frequency band by a simple Fourier transform. FDTD was first used for the simulation of non-dispersive and isotropic materials.

Then, algorithms taking into account the dispersion were developed and used for the calculation of the reflection coefficients [2,3]. Other works taking into account anisotropy in the case of

materials characterized by a diagonal permittivity tensor have been published [4-6]. Finally, a more general FDTD scheme, suitable for anisotropic materials characterized by any permittivity tensor has been proposed more recently [7].

2. 1. 1. Maxwell's equations

We consider a linear, homogeneous, isotropic, non-magnetic medium (that is to say of relative magnetic permeability $\mu_r = 1$) and not charged.

If the medium is devoid of charges and electric currents $\rho = 0$, $j = 0$, the Maxwell-Faraday and Maxwell-Ampere equations in their local form are therefore written as follows:

$$\vec{\nabla}.\vec{E} = 0 \quad \text{Maxwell- Gauss equation} \qquad \textbf{(V. 6)}$$

$$\vec{\nabla}.\vec{H} = 0 \quad \text{Maxwell- Thomson equation} \qquad \textbf{(V. 7)}$$

$$\vec{\nabla}\times\vec{E} = -\mu_0 \frac{d\vec{H}}{dx} \quad \text{Maxwell- Faraday equation} \qquad \textbf{(V. 8)}$$

$$\vec{\nabla}.\vec{H} = \vec{J} + \varepsilon_0\varepsilon_r \frac{d\vec{E}}{dx} \quad \text{Maxwell Ampere equation} \qquad \textbf{(V. 9)}$$

In the two dimensional case, the systems describing the electromagnetic interactions when the polarization is electrical transverse (TE) or magnetic transverse (TM) are:

Electric transverse (TE)

$$\frac{\partial \mathrm{H}_y}{\partial t} = \frac{1}{\mu_0}\left(\frac{\partial \mathrm{E}_z}{\partial x}\right) \qquad \textbf{(V. 10)}$$

$$\frac{\partial \mathrm{H}_x}{\partial t} = -\frac{1}{\mu_0}\left(\frac{\partial \mathrm{E}_z}{\partial y}\right) \qquad \textbf{(V. 11)}$$

$$\frac{\partial \mathrm{E}_z}{\partial t} = \frac{1}{\varepsilon_0\varepsilon_r}\left(\frac{\partial \mathrm{H}_y}{\partial x} - \frac{\partial \mathrm{H}_x}{\partial y}\right) \qquad \textbf{(V. 12)}$$

Magnetic transverse (TM)

$$\frac{\partial E_x}{\partial t} = \frac{1}{\varepsilon_0 \varepsilon_r}\left(\frac{\partial H_z}{\partial y}\right) \quad \textbf{(V. 13)}$$

$$\frac{\partial E_y}{\partial t} = -\frac{1}{\varepsilon_0 \varepsilon_r}\left(\frac{\partial H_z}{\partial x}\right) \quad \textbf{(V. 14)}$$

$$\frac{\partial H_z}{\partial t} = \frac{1}{\mu_0}\left(\frac{\partial E_x}{\partial y} - \frac{\partial E_y}{\partial x}\right) \quad \textbf{(V. 15)}$$

We can independently treat the propagation of these two types of electromagnetic field in the material. The phenomena associated with these two modes can be quite different.

2. 1. 2. Principle of FDTD:

The FDTD method consists in transforming the partial differential equations that we want to solve, into finite difference equations. Taylor's limited series expansions are used for this. Let f(h) be a continuous and differentiable function representing a component of the electric or magnetic field:

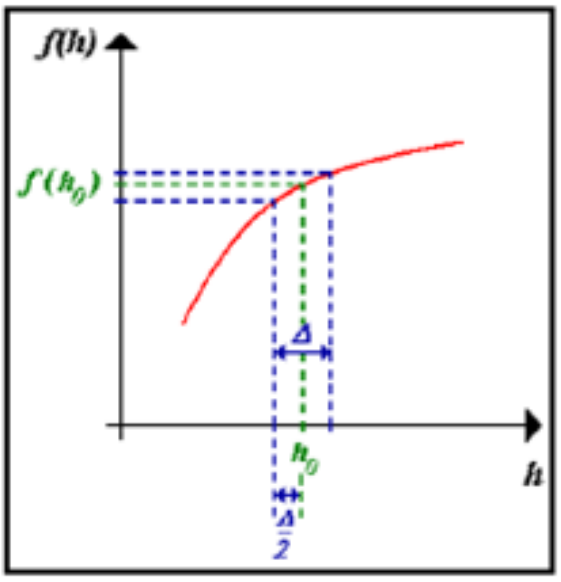

Figure 58:Representation of the principle of calculating the first derivative of h(x) around h_0

It is possible to obtain a centered approximation of the first derivative of f (h) at h_0 by a limited Taylor expansion to the right and left of the point h_0:

$$f(h_0+\frac{\Delta}{2}) = f(h_0)+\frac{\Delta}{2} f^{'}(h)/_{h=h_0}+\frac{1}{2!}(\frac{\Delta}{2})^2 f^{''}(h)/_{h=h_0}+\ldots\ldots\ldots \quad \textbf{(V. 16)}$$

$$f(h_0-\frac{\Delta}{2}) = f(h_0)-\frac{\Delta}{2} f^{'}(h)/_{h=h_0}+\frac{1}{2!}(\frac{\Delta}{2})^2 f^{''}(h)/_{h=h_0}+\ldots\ldots\ldots \quad \textbf{(V. 17)}$$

By subtracting equation (V.17) from equation (V.16) and dividing by Δ, we get:

$$\frac{\partial f}{\partial h}/_{h=h_0} = \frac{f(h_0+\frac{\Delta}{2})-f(h_0-\frac{\Delta}{2})}{\Delta}+o(\Delta^2) \quad \textbf{(V. 18)}$$

where o (Δ^2) represents the 2nd order error that is committed and overlooked.

The FDTD method is based on a double discretization, both temporal and spatial. The 3D space is discretized by a uniform mesh of pitch Δx = Δy = Δz and the space of time is discretized with a time increment Δt. Thus, each partial derivative (temporal or spatial) in the equations of evolution of the components of the electric and magnetic fields (equations (V.10) to (V.15)) will be replaced by a second order Taylor expansion.

2. 1. 3. Discretization of Maxwell's equations:

2. 1. 3. 1. Spatial discretization:

Let us take again the equations governing the temporal evolution of the component along x of the electric and magnetic fields (Equations (V.10) and (V.13)). For the record, these equations are as follows:

$$\frac{\partial H_x}{\partial t} = \frac{1}{\mu_0}\left(\frac{\partial E_y}{\partial z}-\frac{\partial E_z}{\partial y}\right) \quad \textbf{(V. 19)}$$

$$\frac{\partial E_x}{\partial t} = \frac{1}{\varepsilon_0\varepsilon_r}\left(\frac{\partial H_z}{\partial y}-\frac{\partial H_y}{\partial z}\right) \quad \textbf{(V. 20)}$$

According to equation (V.10), the calculation of H_x involves the partial derivative of E_y with respect to z and the partial derivative of E_z with respect to y. The centered approximation of the first derivative requires that the point where we calculate H_x is located at the same time:

- in the middle of a segment parallel to Oz whose two ends are points where E_y is known.

- in the middle of a segment parallel to Oy whose two ends are points where E_z is known.

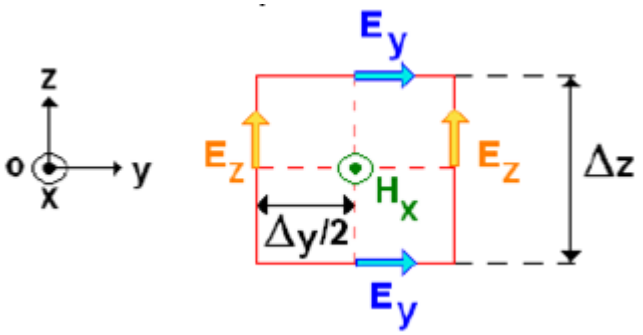

Figure 59:Circulation of the field $\vec{E}$ around $\vec{H}$

Likewise, according to equation (V.13), the point at which E_x is calculated is located at the same time:

- in the middle of a segment parallel to Oz whose two ends are points where H_y is known.

- in the middle of a segment parallel to Oy whose two ends are points where H_z is known.

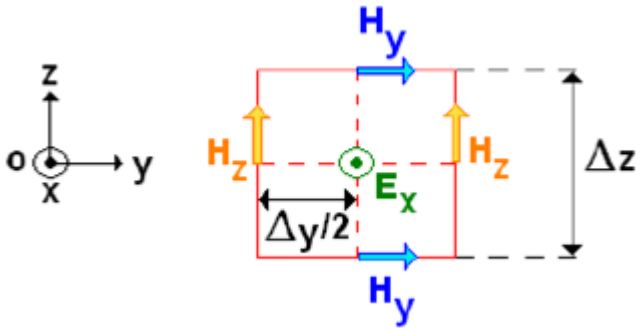

Figure 60:Circulation of the field H around E

The centered approximation of the first derivative applied to equations (V.10) to (V.15) provides conditions which taken together lead to the diagram of Yee shown in Figure .

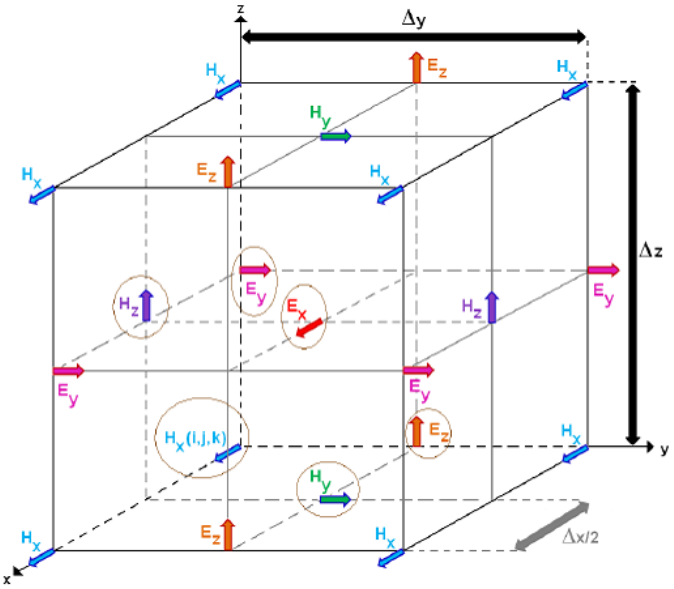

Figure 61:Position of the components of the E and H fields in the spaces in the case of 3 dimensions

The computational domain is therefore subdivided into cubic cells where the components of the electromagnetic field are "exploded". The components circled in brown in figure 61 belong to the elementary cell of Yee identified by the indices (i, j, k). Others components shown in the figure belong to the Yee cells adjacent to the cell (i, j, k).

2. 1. 3. 2. Temporal discretization:

Let's go back to equation (V.19):

$$\frac{\partial H_x}{\partial t} = \frac{1}{\mu_0}\left(\frac{\partial E_y}{\partial z} - \frac{\partial E_z}{\partial y}\right) \qquad \textbf{(V. 20)}$$

It involves in the left side, the time derivative of H_x. The right hand side is considered at time t. The principle of the centered derivative requires that the components E_y and E_z be calculated between two successive instants when H_x is calculated.

By taking into account the five other Maxwell equations (Equations (V.10) to (V.16)), we come to the conclusion that the electric field and the magnetic field cannot be calculated at the same time but at shifted times. By setting Δt the sampling step temporal, we will therefore calculate the electric field for integer multiples of Δt and the magnetic field for half-integer multiples of Δt (Figure 62).

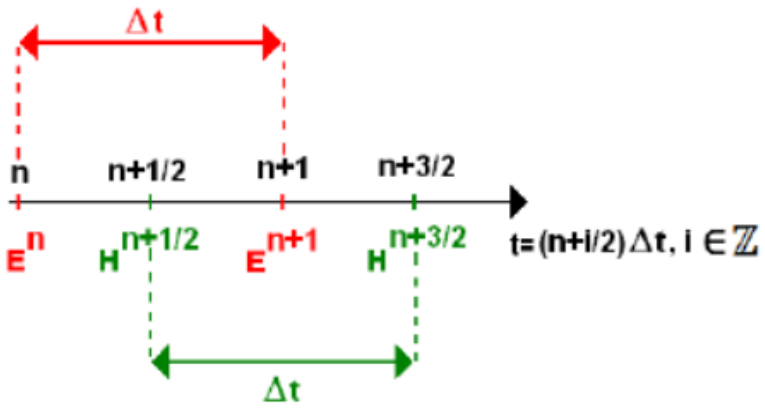

Figure 62:Temporal discretization

2. 1. 3. 3. Discretized Maxwell equations:

After discretization, the partial differential equations (V.10) to (V.16) become respectively:

$$H_x^{n+\frac{1}{2}}(i,j,k) = H_x^{n-\frac{1}{2}}(i,j,k) + \frac{\Delta t}{\mu_0}\left[\frac{E_y^n(i,j,k+1/2) - E_y^n(i,j,k-1/2)}{\Delta z} - \frac{E_z^n(i,j+1/2,k) - E_z^n(i,j-1/2,k)}{\Delta y}\right] \quad \textbf{(V. 21)}$$

$$H_y^{n+\frac{1}{2}}(i+1/2,\, j+1/2,k) = H_y^{n-\frac{1}{2}}(i+1/2,\, j+1/2,k) + \frac{\Delta t}{\mu_0}\left[\frac{E_z^n(i+1,\, j+1/2,k) - E_z^n(i,\, j+1/2,k)}{\Delta x} - \frac{E_x^n(i+1/2,\, j+1/2,k+1/2) - E_x^n(i+1/2,\, j+1/2,k-1/2)}{\Delta z}\right] \quad \textbf{(V. 22)}$$

$$H_z^{n+\frac{1}{2}}(i+1/2,\, j,k+1/2) = H_y^{n-\frac{1}{2}}(i+1/2,\, j,k+1/2) + \frac{\Delta t}{\mu_0}\left[\frac{E_x^n(i+1/2,\, j+1/2,k+1/2) - E_x^n(i+1/2,\, j-1/2,k+1/2)}{\Delta y} - \frac{E_y^n(i+1,\, j,k+1/2) - E_y^n(i,\, j,k+1/2)}{\Delta x}\right] \quad \textbf{(V. 23)}$$

$$E_x^{n+1}(i+1/2,\, j+1/2, k+1/2) = E_x^n(i+1/2,\, j+1/2, k+1/2) + \frac{\Delta t}{\varepsilon_0 \varepsilon_r}\left[\frac{H_z^{n+\frac{1}{2}}(i+1/2,\, j+1, k+1/2) - H_z^{n+\frac{1}{2}}(i+1/2,\, j, k+1/2)}{\Delta y} - \frac{H_y^{n+\frac{1}{2}}(i+1/2,\, j+1/2, k+1) - H_y^{n+\frac{1}{2}}(i+1/2,\, j+1/2, k)}{\Delta z}\right] \quad \textbf{(V. 24)}$$

$$E_y^{n+1}(i,\, j, k+1/2) = E_z^n(i,\, j, k+1/2) + \frac{\Delta t}{\varepsilon_0 \varepsilon_r}\left[\frac{H_x^{n+\frac{1}{2}}(i,\, j, k+1) - H_x^{n+\frac{1}{2}}(i,\, j, k)}{\Delta z} - \frac{H_z^{n+\frac{1}{2}}(i+1/2,\, j, k+1/2) - H_z^{n+\frac{1}{2}}(i-1/2,\, j, k+1/2)}{\Delta x}\right] \quad \textbf{(V. 25)}$$

$$E_z^{n+1}(i,\, j+1/2, k) = E_z^n(i,\, j+1/2, k) + \frac{\Delta t}{\varepsilon_0 \varepsilon_r}\left[\frac{H_y^{n+\frac{1}{2}}(i+1/2,\, j+1/2, k) - H_y^{n+\frac{1}{2}}(i-1/2,\, j+1/2, k)}{\Delta x} - \frac{H_x^{n+\frac{1}{2}}(i,\, j+1, k) - H_x^{n+\frac{1}{2}}(i,\, j, k)}{\Delta y}\right] \quad \textbf{(V. 26)}$$

Equations (V.21) to (V.26) are the updating equations for the components of the electromagnetic field. For example $E_z^{n+1}(i, j+1/2, k)$, the notation represents the value of the component of the electric field along the z axis, at the coordinate point and at time. Equation (V.26) shows that at time t, the component E_z of the electric field is calculated from:

- of the E_z component at the same point in discretized 3D space, but at the previous instant.
- time values of the four closest components of the surrounding magnetic field.

The updating of the six components of the electromagnetic field is repeated at each time sampling time. The evolution of the electromagnetic field over time is therefore deduced by an iterative calculation known as the "leapfrog" diagram:

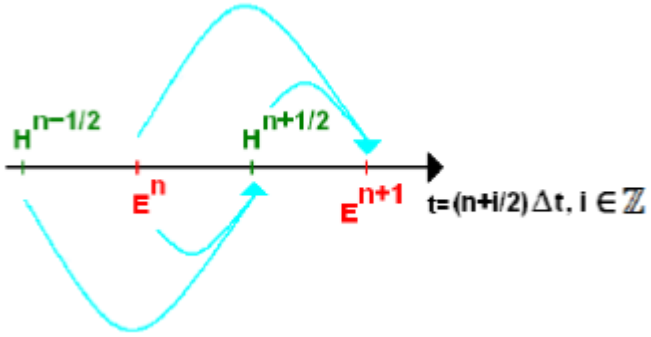

Figure 63:Iterative diagram

This way of calculating the electromagnetic field is intuitive and represents physical reality well in that a variation of the electric field generates a variation of the magnetic field which, in turn, generates a variation of the electric field and so on. We can represent the FDTD algorithm as follows:

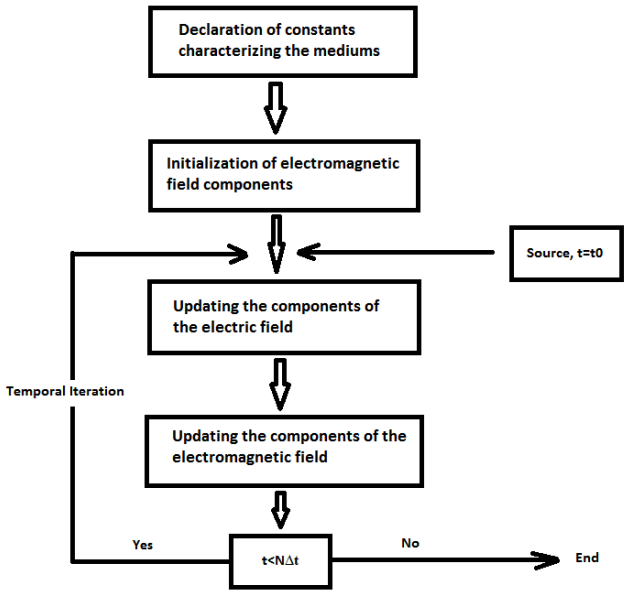

Figure 64:FDTD algorithm

2. 2. Choice of spatial and temporal steps:

The choice of spatial and temporal steps is not arbitrary. It impacts both the accuracy and the stability of the FDTD algorithm.

First, the spatial discretization must be fine enough in order to correctly describe the geometry of the objects belonging to the studied system as well as the distance between these objects. In addition, the passage of a physical problem in a continuous space-time
to a discrete problem in a sampled space-time creates a parasitic effect called digital dispersion. This effect stems from errors made in the evaluation of the wave propagation speed in the computational domain. In order to minimize the distortion of
signals due to digital dispersion, the value of the spatial steps is fixed according to the minimum wavelength present in the FDTD grid [2, 3]:

$$Max(\Delta x, \Delta y, \Delta z) \leq \frac{\lambda_{\min}}{10} \quad \textbf{(V. 27)}$$

In the case of a uniform mesh in the (Δx=Δy=Δz=Δ)

$$\Delta \leq \frac{\lambda_{\min}}{10} \quad \textbf{(V. 28)}$$

It can be seen from equation (V.28) that it is necessary to have at least 10 cells per wavelength to obtain correct results.

Second, iterative temporal algorithms like FDTD can generate an erroneous, usually exponential, increase in the values of the electromagnetic field leading to the divergence of the calculation. To overcome this problem, care must be taken when choosing the temporal increment to respect a criterion called a criterion of numerical stability or a Courant-Friedrichs-Lewy criterion [2, 4, 5]:

$$\Delta t \leq \frac{1}{c\sqrt{\frac{1}{\Delta x^2}+\frac{1}{\Delta y^2}+\frac{1}{\Delta z^2}}} \quad \textbf{(V. 29)}$$

Were c it is the speed of light in a vacuum, In the case of a uniform mesh with Δx=Δy=Δz=Δ, the inequality (V.29) is simplified and becomes:

$$\Delta t \leq \frac{\Delta}{c\sqrt{3}} \quad \textbf{(V. 30)}$$

2. 3. Results and discussions

In a first step of this simulation, we are interested in a monochromatic Gaussian plane wave source with polarized waves TM illuminates a metallic cylinder with radius r =15nm and permittivity ε2, immersed in a dielectric medium (glycerol) with the permittivity ε2 as shown in this Figure.

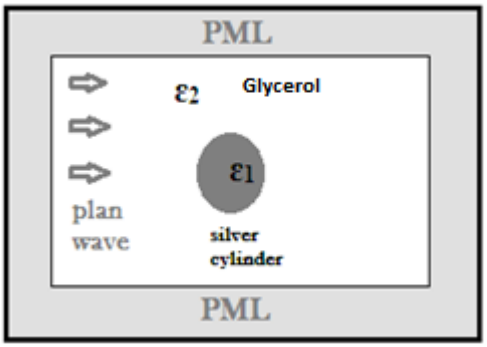

Figure 65:Nanoparticle in our medium

The operating frequency of the incident plane wave generated with a value in the visible range is f = 750 THz, which corresponds to the wavelength in free space, λ = 400 nm.

The 2D-FDTD computational domain is discretized with 200*200 Yee cells and ends with 10 cells. PMLs were used to truncate the simulation region with the condition [23]:

$$\frac{\sigma}{\varepsilon_0} = \frac{\sigma^*}{\mu_0} \qquad \textbf{(V. 31)}$$

Where ε_0 and μ_0 are the permittivity and permeability of free space, σ is the specific conductivity, σ^* is a nonphysical parameter that allows the absorption of the magnetic field to be symmetrized with respect to the absorption of the electric field.

The spatial discretization is uniform, and can be given as $\Delta x = \Delta y = 10^{-9}$ m. The time step is chosen to satisfy the Courant–Friedich–Levy (CFL) condition for FDTD algorithm as:

$$dt = \frac{dx}{\sqrt{2}c} \qquad \textbf{(V. 31)}$$

where c is the speed of light in the free space.

In each of these examples, the silver sphere was assumed to be characterized by the following Drude model parameters in [15, 19]: $\varepsilon_\infty = 1$; $\omega p = 1.256 .10^{16}$ rad/s; $vc = 5.7 . 10^{13}\ s^{-1}$

The dielectric medium (Glycerol) has been characterized by the permittivity ε_2=27.

2. 3. 1. Visualization of the FDTD-computed E_z scattered field

The following figure 66 represents the Visualization of the distribution of the electric field E_z calculated by FDTD along the x-y plane, we notice the electric field from the left hand to the right hand side and the amplitude of the electric field inside the metal is almost zero. On the other hand,

when the wave crosses the nanoparticle in the vicinity of the nanoparticle, the wave does not remain planar. the major observed phenomenon is the interference produced between the incident and scattered waves by the metal.

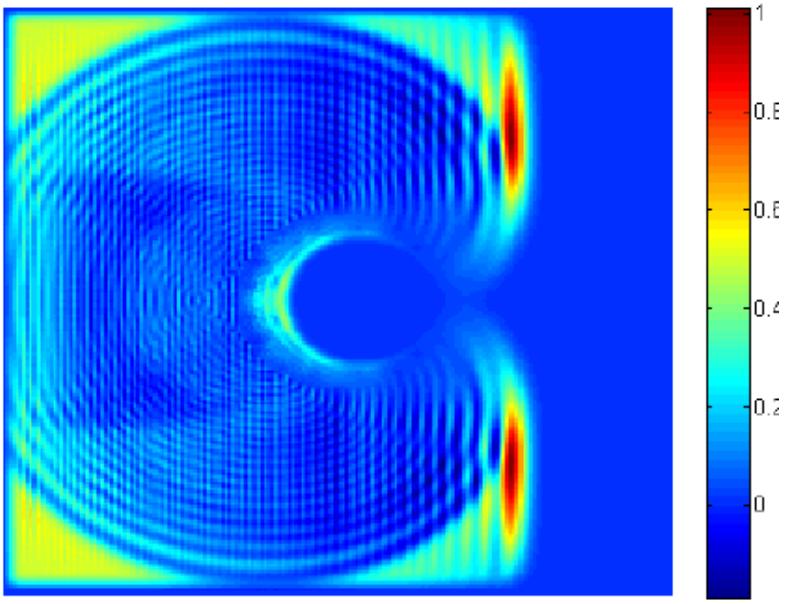

Figure 66:Visualization of the FDTD-computed Ez field distribution along the x-y planar for Silver nanoparticle in Glycerol

The electric field is intense on the surface of the metal and inexistent inside the nanoparticle, which denotes an exaltation is accompanied by the collective oscillation of the electrons free from the surface of the metal. This last phenomenon can occur when the field overlaps in the vicinity of the metal or when the incident wave has a frequency equal to the frequency of surface Plasmon resonance (SPR)

2. 3. 2. Coupling between several nanoparticles

Another method for achieving strong exaltations is to couple two or more nanostructures together. As we have seen previously, when the distance between two nanoparticles is less than a few tens of nanometers, there is the possibility of overlapping fields close to the two nanoparticles and therefore electromagnetic coupling. In this case, when the incident electric field is polarized along the coupling axis between the two nanoparticles, a very strong field is created inside the space between the nanoparticles. “Hot spots” then form, as shown by the figures (67, 68, 69) of 2,3,6 nanoparticles.

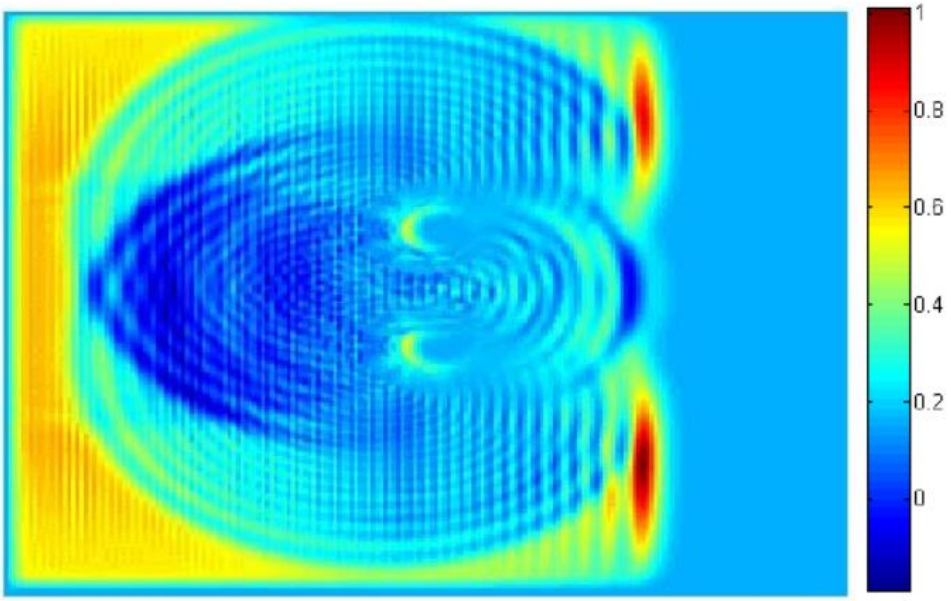

Figure 67:Visualization of the FDTD-computed Ez field distribution of Coupling between two nanoparticles

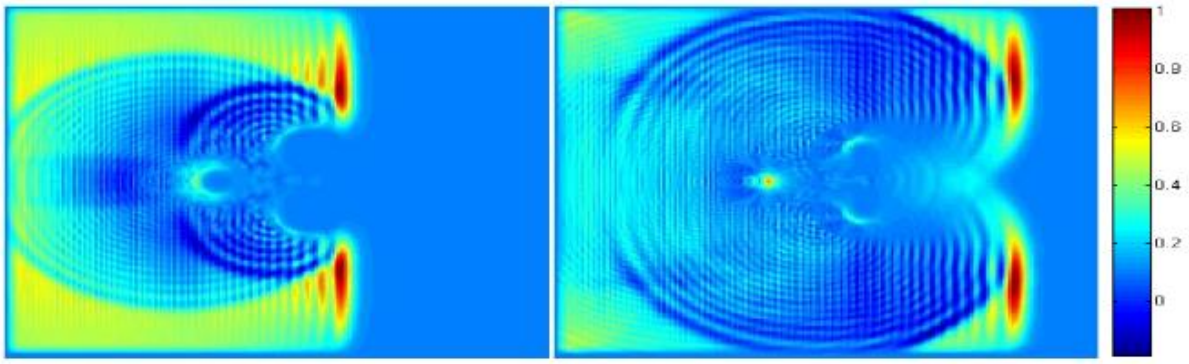

Figure 68:Visualization of the FDTD-computed Ez field distribution of Coupling between three nanoparticles

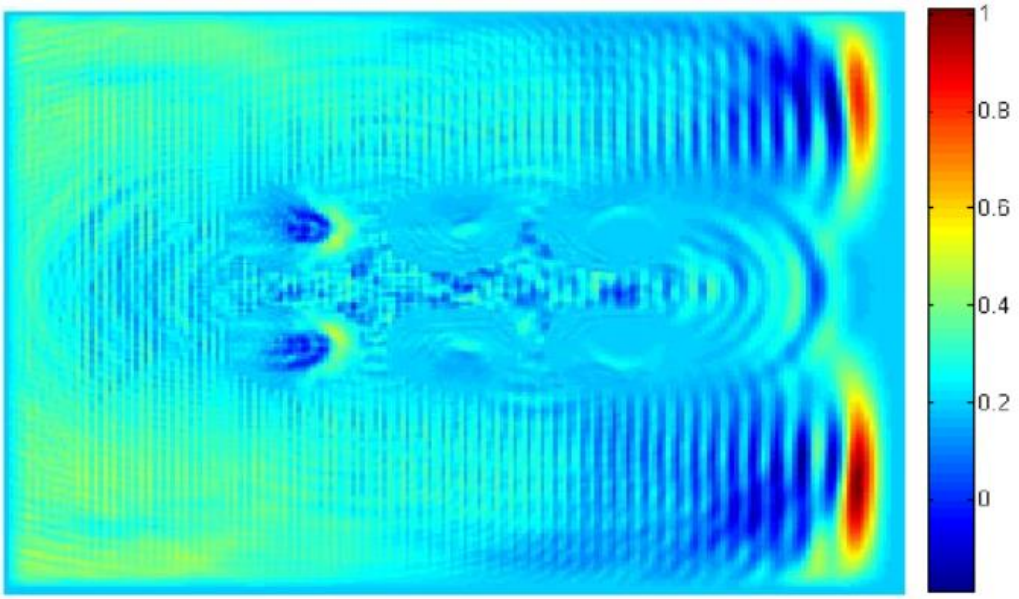

Figure 69:Visualization of the FDTD-computed Ez field distribution of six nanoparticles particles along the x-y planar

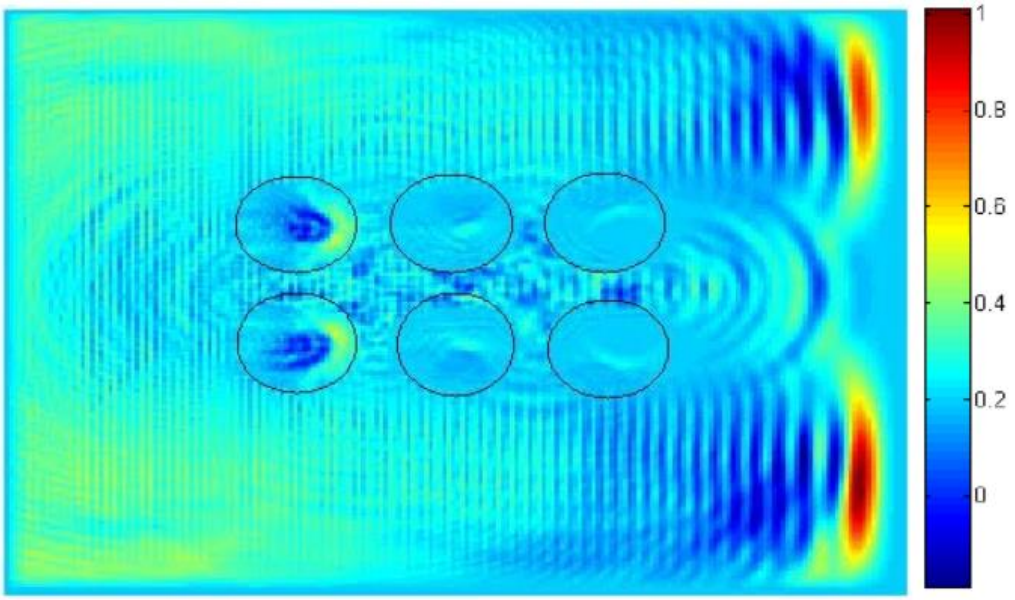

Figure 70:Visualization of the FDTD-computed Ez field distribution of coupling six Silver nanoparticles along the x-y planar

2. 3. 3. Results and Comparisons with Experiment

In this section we investigate the calculation of The cross section of the coupling nanoparticles: To model this phenomena, we used the FDTD method as numerical method by solving Maxwell's equations, which can generate the cross sections of nanoparticles networks and aggregates.

Figure 71 gives graphical representation of the cross section as function of frequency for two, three and six silver nanoparticles immersed in Glycerol medium; we note that the position of the surface plasmon resonance shifts as a function of the concentration (or volume fraction) of the nanoparticles in the matrix. For the case of a single nanoparticle we found the position of SPR corresponding to the wavelength is equal to 405nm, and for the two nanoparticles coupling we found 422.5nm, three nanoparticles is 425.5nm and for the last correspond coupling six nanoparticles at wavelength 428nm.

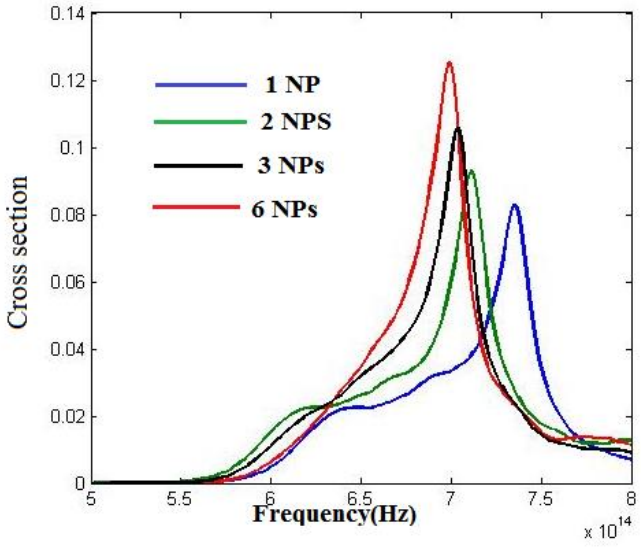

Figure 71:Cross section as function of frequency for two, three and six silver nanoparticles

On the other hand, we remark that frequencies are in the order of 10^{14} Hz (tera hertz). of particular interest of the corresponding resonance are shifted towards low frequencies (red shifted) as the volume fraction increase, and the amplitude becomes much larger. this shows that the color of the nanoparticles is strongly impacted by the number of added nanoparticles.

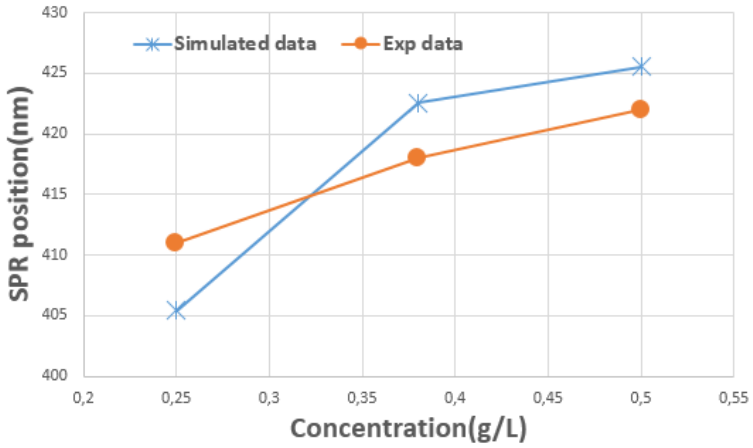

Figure 72:SPR position as function concentration

CONCLUSION

The simulation of the hot wire method under Comsol multiphysics allowed us to validate our experimental device for the calculation of thermal conductivity for pure water and pure Glycerol, which led us to measure the thermal conductivity of nanofluids. synthesized by silver nanoparticles and Glycerol (chapter 4). The value of the thermal conductivity of our simulation which is close to the value of the experiment and also for the biographical value which brings us back to give a great importance to make these three values less offset in order to use this unwinding of measure in other works.

The plasmonic properties of spherical silver nanoparticle systems with diameters of 15nm were studied with the FDTD method. Surface plasmon resonance appears in the near ultraviolet Ag domain for a single silver nanoparticle. From the simulation, we can state that the 15nm diameter was in the visible or near ultraviolet range. Therefore, the couplings of the silver nanoparticles were of the correct peak shift and peak broadening was optimal when the concentration of the nanoparticles or (Volume Fraction) increased, which is confirmed by the experimental results. Meanwhile, silver nanoparticles were applicable for different applications according to its needs. Examples of application such as biosensor, application of catalyst and therapeutic agents, without forgetting the improvement of thermal conductivity as seen in chapter III.

References

[1] Yee, K. S. Numerical Solution of Initial Boundary Value Problems Involving Maxwell's Equations in Isotropic Media; IEEE Trans. Antennas Propagat. 1966, AP-14, 302–307.
[2] Taflove, A.; Hagness, S. C. Computational Electrodynamics The Finite-Difference Time-Domain Method, 3rd ed.; Artech House, 2005.
[3] Kunz, K. S.; Luebbers, R. J. The Finite Difference Time Domain Method for Electromagnetics; CRC Press, Boca Raton, 1993.
[4] Sullivan, D. M. Electromagnetic Simulation Using the FDTD Method; New York, IEEE Press, 2000.
[5] Berenger, J. R. A perfectly matched layer for the absorption of electromagnetic waves; J. Computat. Phys. 1994, 114, 185-200.
[6] Zhao, Y.; Hao, Y. Finite-difference time-domain study of guided modes in nano-plasmonic waveguides; IEEE Trans. Antennas Propag. 2007, 55, 3070–3077.
[7] Zhao, Y.; Hao, Y. Conformal Dispersive Finite-Difference Time-Domain Simulations of Plasmonic Waveguide

CHAPTRE VI:

EFFECT OF ERBIUM AND GADOLINIUM ON OPTICAL, ELECTRICAL AND MORPHOLOGY PROPERTIES OF POLYTETRAFLUOROETHYLENE

INTRODUCTION

Conductive materials, including lanthanides are extremely dynamic because of their interesting properties; for example: Short band gap, high absorption coefficients, bonding energy, chemical stability and environmentally friendly applications, the other hand insulators such as Teflon represent a very high electrical resistivity (transverse volume resistivity> 1018Ohm.cm) and thermal (maximum operating temperature peak 300°C and thermal conductivity 23° equal 0.23W/(Km). Teflon also represents a variety of applications namely Bearings, pads, soles Electrical Insulating Joints, anticorrosion, the protection of cells solar panels [1]. Our aim is to make the material a semiconductor for use both for the protection of solar panel cells and the manufacture of photovoltaic cells (solar cells based on organic semiconductors which may be flexible and easily manufactured by printing and coating techniques [2]. Organic semiconductors have the advantage of chemical adaptation; they also have flexibility of their properties. An example of this type of solar cells is based on mixtures of poly {[2-methoxy-5 - [(3,7-dimethyloctyl) oxy] phenylene] vinylene} (MDMO-PPV) and 1- [3- (methoxycarbonyl) propyl] -1-phenyl- (6,6) -C61 (PCBM) that has been recently manufactured and extensively studied with power conversion efficiencies up to 3% [3]. In this work, polytetrafluoroethylene (PTFE) is doped by a transition element such as Erbium (Er) which is part of the lanthanides. In the following paragraph we will detail the method of development and the characterization technique of our product to determine the optical, electronic and structural parameters.

Conductive materials, which can be found in the periodic table, including the lanthanides, due to their interesting properties; for example: the absorption coefficients of UV-visible waves high in the wavelengths near UV [1], which translates bursts of very reduced gap energy [2], for this reason we thought of boosting our basic material PTFE by these Gadolinium (Gd) to have results similar to the result of a PTFE article doped with Erbium (Er) which is of the same family as Gd [3].

Chemical stability and environment-friendly applications, Teflon represents a very high electrical resistivity (transverse volume resistivity>1018□.cm), other famous physical properties such as thermal conductivity (maximum operating temperature peak) 300 °C and thermal conductivity 23 ° equal to 0.23 W/Km. Teflon also represents a variety of applications in the field of mechanics, namely bearings, skates, soles, electrical insulating seals, anticorrosion, also in the field of renewable energy such as the protection of cells solar panels [4]. Our main objective is to convert the insulating material PTFE into a semiconductor intended for the protection in the field of cells

of solar panels and for the manufacture of photovoltaic cells flexible: solar cells containing organic semiconductors which can be flexible and easily fabricated by printing and coating techniques [5, 7].

The advantages of organic semiconductors are chemical adaptation and flexibility adaptation to accommodate support forms. An example of this type of solar cell is based on mixtures of poly {[2-methoxy-5 - [(3,7-dimethyloctyl) oxy] phenylene] vinylene} (MDMO-PPV) and 1- [3-methoxycarbonyl propyl] -1-phenyl- (6,6) -C61 (PCBM) which was recently manufactured and widely studied with power conversion yields of up to 3% [6]. In this work, we doped polytetrafluoroethylene (PTFE) with a transition element such as Gd which is from a family of lanthanides. We will detail the characterization methods, namely X-ray diffraction (DRX) to determine the parameters of structure, and the characterization by FT-IR to know functions.

1. Effect of Erbium addition on optical and electrical properties of Polytetrafluoroethylene

1. 1. Experimental method of elaboration

The Teflon based semiconductor synthesis was prepared by solid state with various percent of Erbium us shown in table VI.1.

Table VI. 1:Represent teflon and teflon doped on function of various percent of erbium (Er)

	Masse	
	PTFE on (g)	Erbium on(g)
PTFE	1	0
PTFE+Er (1%)	0,9	0,01
PTFE+Er (2%)	0,98	0,02
PTFE+Er (3%)	0,97	0,03
PTFE+Er (4%)	0,96	0,04
PTFE+Er (5%)	0,95	0,05

Samples are placed in alumina burrows after 1mm grain size burring, after which they are placed in at 100°C for 45 min and we have increase the temperature oven 500°C , it's the transition of temperature of Teflon and Teflon doped by Erbium.

1. 2. Results and discussions

1. 2. 1. Characterization by UV-Visible

Our work that we have chosen concerning the electrical and optical characterizations of Teflon and Teflon doped by Erbium (Er), this study consist of effect Erbium (Er) on the electrical and

optical properties of Teflon. The samples were characterized by UV-Visible

1. 2. 1. 1. Transmittance.

The Figure 73 shows the transmission as a function of the wavelength (λ), we see five spectra with different transmission, the latter has started from the ultra violet to the infrared domain so the minimal transmission of the spectra or the common point between they took the value 5% and 250 cm^{-1}, at this point the polymer transmitted all intensities even though it doped with Erbium besides the 1% doped teflon transmission value is 65% in the visible then 60% in the ultra violet, the 2% doped Teflon transmission value is 40% in the visible and 35% in the ultra violet as well as the transmission value the Teflon doped 4% is 15% in the visible and 10% in the ultra violet, as well as the Teflon transmission value doped with 5% of Erbium is 20% in the visible range and 12% in the ultra violet field. Indeed, when the percentage of Erbium is important, the transmission decreases in the visible range and in the ultra-violet field, we also see an accelerated increase in transmission in the infrared field of around 825 cm^{-1}. This increase will continue up to 96% since teflon is much more transparent in the infrared range than glass. These differences in Erbium composition give rise to systematic changes in optical properties such as refractive index and absorption coefficient not to mention the interesting fact to note is the rapid growth of absorption towards the violet. This absorption must be even greater in the ultraviolet; Erbium also has a high transmittance in the infrared. Moreover, we see bands of the same wavelength in the transmission spectra, the width and the height of the bands are varied during doping with Erbium. We take the case of teflon doped with 5% Erbium we find three bands, one in the field of ultra violet to 375cm^{-1} and the others in the visible range of 525cm^{-1} and 650cm^{-1} corresponding transitions in the doped polymer, they are induced the values of the optical gap energy (E_{gap}^{Opt}),

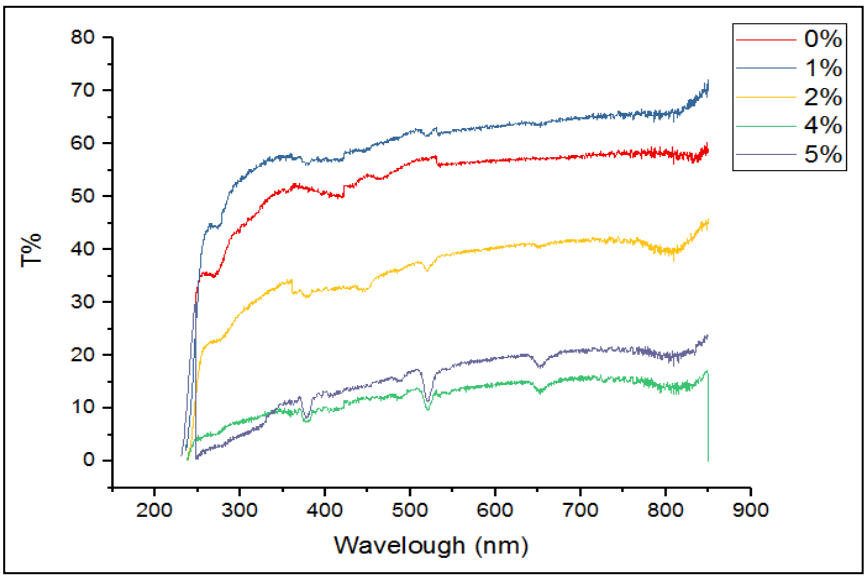

Figure 73:Tthe spectra of transmission for Teflon (C2F4)n doped by Erbium (Er)

1. 2. 1. 2. Absorbance

The Figure 74, represent the absorption spectrum as a function of the wavelength (λ), this spectrum only shows the electronic absorption, and it is measured between 200 and 850 nm in using Teflon doped with Erbium (Er) in the solid state. The ambient temperature we notice that the five compounds have a strong absorption in the region of ultra violet and against the compounds absorbs only weakly between 400 and 850 nm with different values of the absorbance of more when increasing the concentration of Erbium (Er) in teflon the absorbance decreases, we have noted that teflon is a highly coordinating polymer and may be capable of complexing on Erbium (Er^{+5}) ions and when Erbium (Er) is depleted in electrons, to promote complex formation teflon-Erbium (Er) although the uptake hardly increases anymore which indicates that the modified Teflon surface, It should be noted that no band is observed in the spectrum of Teflon.

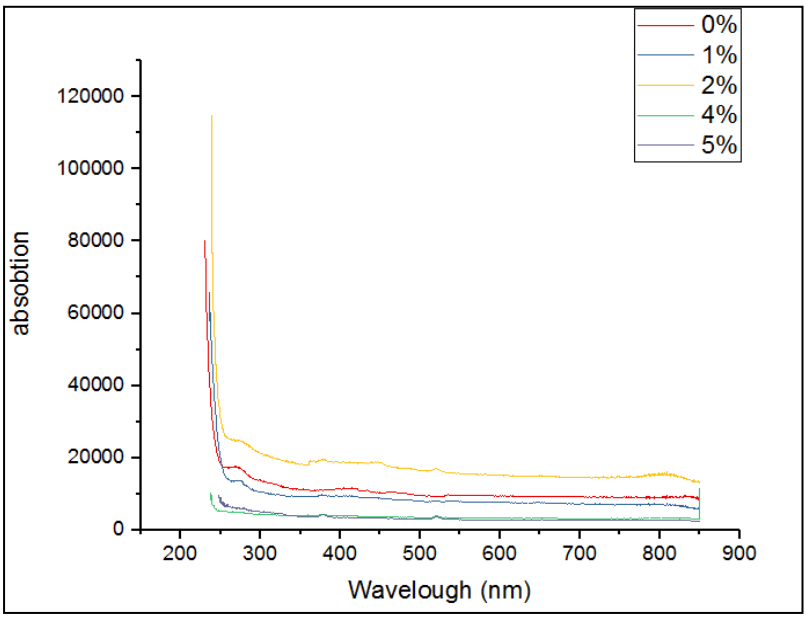

Figure 74:Absorbance of Teflon (C2F4)n doped by Erbium (Er)

1. 2. 2. Determination of Gap energy

By experiment, to determine the gap energy, Teflon doped by deferential percentage of Erbium (Er), one can plot $(\alpha h\nu)^2$ as a function of the photonic energy ($h\nu$) based on the values of the optical transmission as shown in Figure 75. We notice a straight line in a certain region. In order to obtain the value of the optical gap energy (Eg^{opt}) of Teflon doped with erbium (Er) by increasing the percentage up to 5% as shown in Table VI.1, the tangent with each curve can be traced to the intersection with the abscissa axis. The estimated values of the gap energy were written in Table VI.1. It was observed that the optical gap energy (Eg^{opt}) decreased with the increase in the percentage of Erbium (Er) in the polymer. This result showed that erbium (Er) has a significant effect on the crystal lattice, a very high electrostatic interaction. This observed trend can also be correlated with the atom distribution defects due to the average atomization energy which is increased with the addition of erbium moreover it absorbed by Teflon, so the gap band is due to the coherent diffusion of the electrons by an effective periodic potential which depends on the state in the ground state of the system, Table VI.1 illustrates the variation of the optical band gap energy (Eg) with respect to the Erbium (Er) compositions in Teflon. The relation obtained is not linear; the non-linearity of the band gap variation with the compositions has already been reported for many published works. This result confirmed that this polymer can be used as semiconductors and photovoltaic and optoelectronic devices. When certain additives are added in high concentration, a new alloy or compound is formed and a new band gap is observed. In conclusion, the gap energy

is an energy gap for the electrons in the crystal lattice that requires some kind of energy for the conduction to be done by an electric field in the semiconductors.

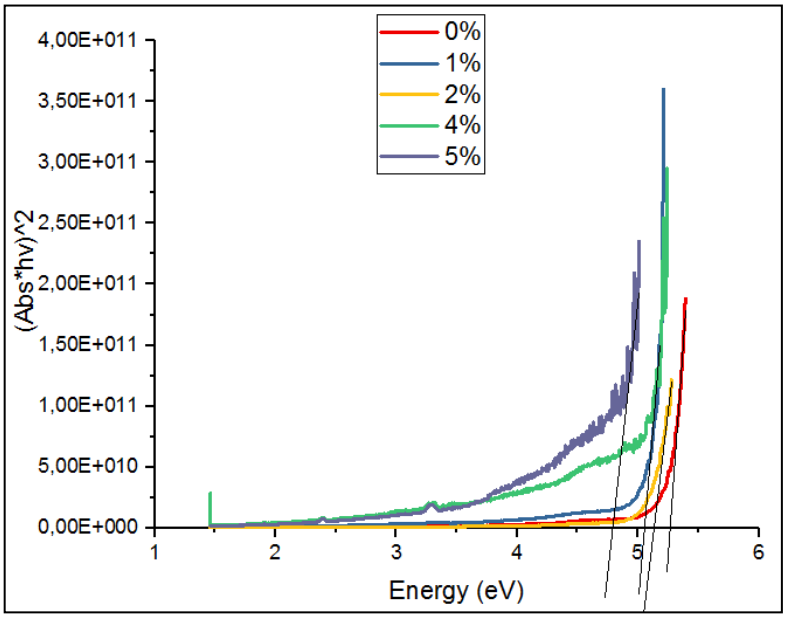

Figure 75:The variation of the dependence $(\alpha hv)^2$ as a function of photon energy (E_{ph})

Table VI. 2:Represent the gap energy (Eg) of Teflon and Teflon doped by Erbium (Er)

Percentage	Gap energy on (eV)
Téflon+(0%) d'Erbium	5,25
Téflon+(1%) d'Erbium	5,15
Téflon+(4%) d'Erbium	5,05
Téflon+(5%) d'Erbium	4,75

1. 2. 3. Determination of the Urbach energy

The Figure 76 shows the evolution of gap energy (E_g) and that of Urbach (E_u) measured on our samples according to the percentage used during the doping. The values of energy (E_g) were determined from the formula of Tauc [4] and those of Urbach (E_u) using the Urbach's law [5]. We note that the two quantities E_g and E_u evolve in strictly opposite directions. The Figure 76 us shown the next description: When one increases the other decreases, and when the first one reaches the

second reaches its minimum. This clearly confirms the very close correlation which exists between these two quantities and which is logically due to the presence of a more or less significant density of dangling bonds in the material. For low percentage values, there is a large, steady and rapid increase in the Urbach energy (Eu) as shown in Table VI.3

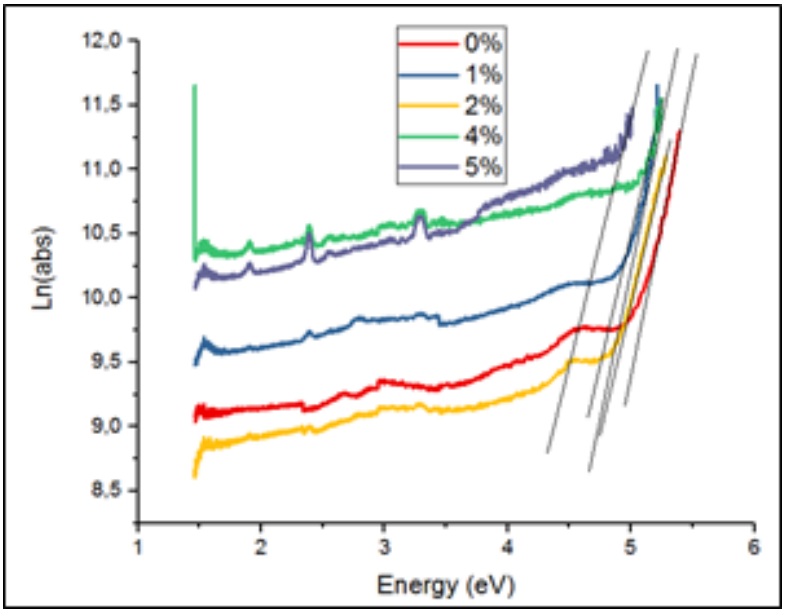

Figure 76:Variation of dependence of absorption as a function of photon energy (E_{ph})

Table VI. 3:Represent the urbach energies and teflon doped with erbium (Er)

Pourcentage	Urbach energy (eV)
Téflon+(0%) d'Erbium	0,233
Téflon+(1%) d'Erbium	0,24
Téflon+(3%) d'Erbium	0,25
Téflon+(4%) d'Erbium	0,355
Téflon+(5%) d'Erbium	0,58

The figure 77 us shown the Evolution of the optical gap (E_g) and the Urbach energy (E_u) measured on our samples according to the percentage used during the doping. The values of E_g were determined from the formula of Tauc [4] and those of E_u using Urbach's law [5]. We note that the two quantities E_g and E_u evolve in strictly opposite directions.

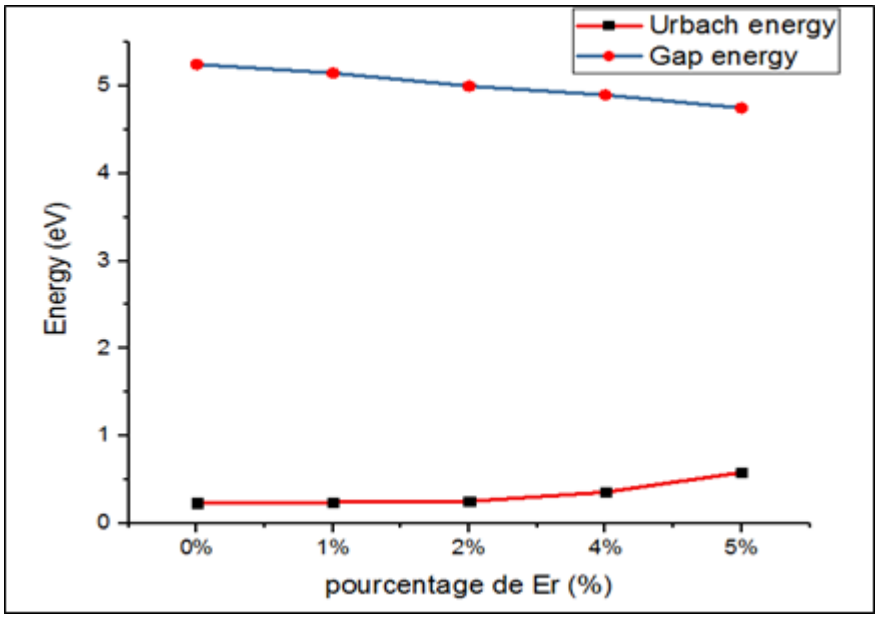

Figure 77:The evolution of the optical gap (E_g) and the Urbach energy (E_u) according to the percentage

2. Effect of Erbium addition on morphology of Polytetrafluoroethylene

2. 1. Characterization by X-ray diffraction analysis

Teflon-based compounds have been characterized by ADVANCE D8 X-Ray diffraction, we have noticed a more intense peak in the crystallized phase, this peak represents the probability of finding the phase, moreover the purity of the material as well. Other peaks appeared. The effect of the Erbium element (Er) on the studied phase gave information on the displacement of the peaks as well as the intensity, it was deduced that the erbium reacted with the Teflon. Figure 78 shows the X-ray diffraction spectra of Teflon and doped Teflon. All the reflections peaks were indexed in orthorhombic system Space group (P m m m). The parameters generated by Fullprof program as shown in table VI.4. The effect of Erbium (Er) on the Tetrafluoroethylene $(C_2F_4)_n$, such as the grains size, displacement of position and intensity, have been studied in the percentage range 1% to 5% us shown in the figure 79.

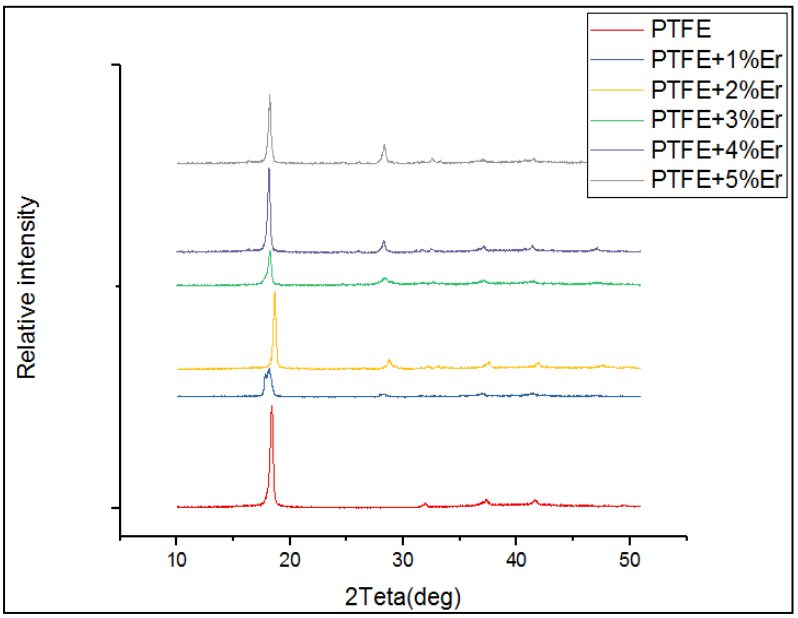

Figure 78:X-ray diffractograms of PTFE and Different percentage of Erbium (Er) doped in the Teflon material

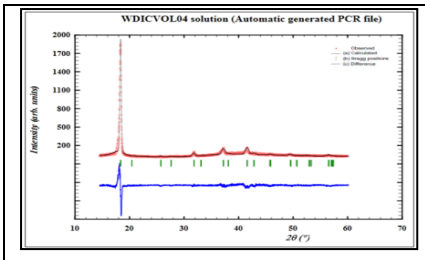

Fig. VI.7.1. Profile Matching with constant scale factor refinements on $(C_2F_4)_n$: experimental, calculated and differential spectra

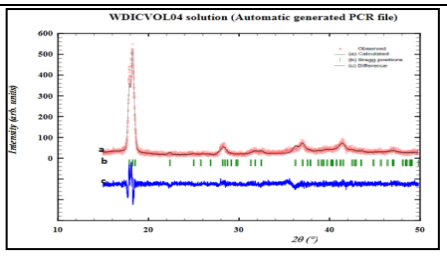

Fig. VI.7.2. Profile Matching with constant scale factor refinements on $(C_2F_4)_n$ at 1% Er: experimental, calculated and differential spectra

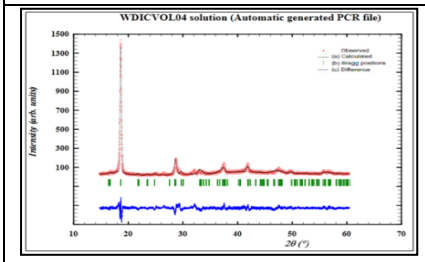

Fig. VI.7.3. Profile Matching with constant scale factor refinements on $(C_2F_4)_n$ at 2%Er: experimental, calculated and differential spectra

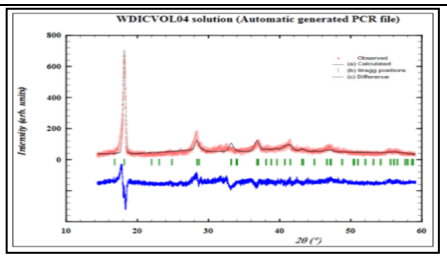

Fig. VI.7.4. Profile Matching with constant scale factor refinements on $(C_2F_4)_n$ 3%Er: experimental, calculated and differential spectra

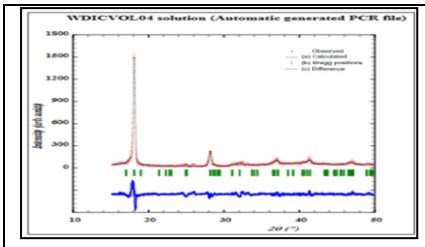

Fig. VI.7.5. Profile Matching with constant scale factor refinements on $(C_2F_4)_n$ 4%Er: experimental, calculated and differential spectra

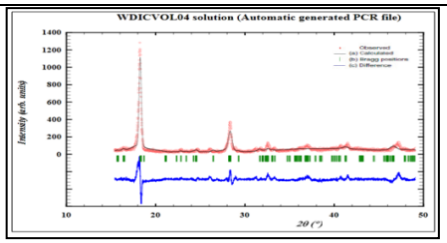

Fig. VI.7.6. Profile Matching with constant scale factor refinements on $(C_2F_4)_n$ 5%Er: experimental, calculated and differential spectra

Figure 79:The Figures of X-ray Diffractograms of various temperatures of Teflon and Teflon doped

Table VI. 4:Cell parameters extracted from full pattern refinements of various percentage of erbium

Temperature	A[Å]	B[Å]	C[Å]	V[Å³]	Space group	Crystal System
PTFE	4.8326	4.3457	3.4599	72.6615	P m m m	Orthorhombic
PTFE+1%Er	7.1251	6.9111	6.6416	327.0475	P m m m	Orthorhombic
PTFE+2%Er	10.7686	6.2683	5.3154	358.7940	P m m m	Orthorhombic
PTFE+3%Er	6.2885	5.2723	4.8830	161.8952	P m m m	Orthorhombic
PTFE+4%Er	15.6326	4.9031	3.9878	305.6577	P m m m	Orthorhombic
PTFE+5%Er	18.9923	5.6523	5.6064	601.8480	P m m m	Orthorhombic

The figure 80 shows the variation of cell parameters of tetrafluoroethylene doped by Erbium, according to the percentage. We observe an increase of the parameters (a,b and c) between 0 and 1%, then a decrease of the parameters (b,c) between 1% and 4% for returns in increase but the parameter (a) continue to increase until 2% then we observe a high an increase between 3% and 5% . These variations can give some explanation of the crystalline structure of the samples formed. The decrease of parameterizes b and c can be connected the grain size of Teflon doped, the increase or the decrease of the parameters of the cell can be bound to the elasticity of the network trained by groupings bound only by summits.

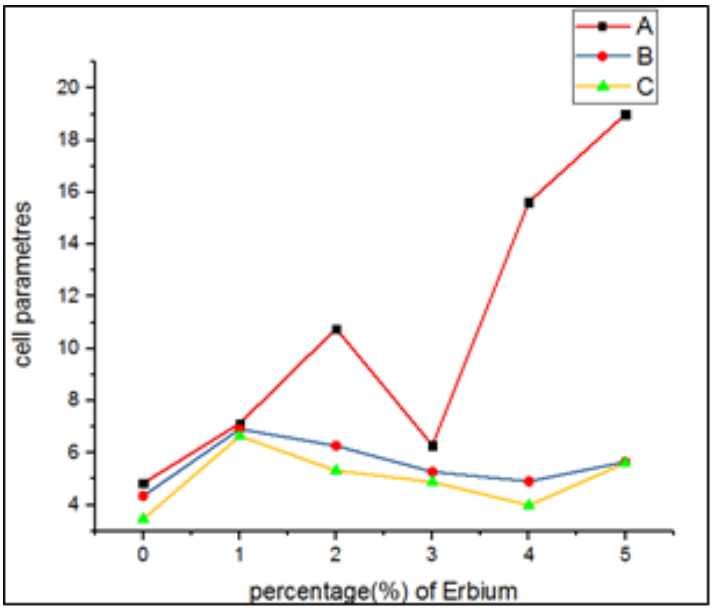

Figure 80:The variation of cell parameters of tetrafluoroethylene and tetrafluoroethylene doped by Erbium, according to the percentage.

2. 1. 1. Determination of micro structural parameters

The mechanism of X-rays Diffraction in the crystalline materials is that the X-rays scatter from crystals because their electric fields interact with the clouds of electrons of atoms in crystals. The X-rays scattered from the periodic neighboring atoms interfere and give rise to a plan of diffraction. The plan of diffraction is modulated by the function of transfer of the detector which in his turn modifies the shape of the profile of diffraction of the X-rays. So, a profile of line of diffraction is the result of the convolution of a number of independent variables contributing to the form profile to know the instrumental variables and the micro structural effects. The instrumental variable includes the width of crack of reception, the transparency of the sample, the nature of the source of X-rays, the axial difference of the incidental beam and the flat sample geometry [6]. The micro structural effects responsible for the profile of shape of the peaks of diffraction are the following ones. Size finished crystals or domains and micro strain the crystal contains defects of network. These profiles are equipped with functions of shape of adapted profile in a way that the functions asymmetric peaks and it should be so simple mathematically as possible to do the calculation of all the by products have variables

.

2. 1. 2. Crystallite size and microstrain with Wiliam-Hall

From the X-rays in the polycrystalline material is due to the presence of crystallites (effect of size) as well as the micro strain effect. The slopes of the plan W-H represent the internal average microstructure. While the opposite of the orderly at the origin of the axis $\left(\frac{\beta\cos(\theta)}{\lambda}\right)^2$ give the size of crystallites according to the relation. While the opposite of the orderly at the origin of the axis gives the size of crystallites according to the relation.

$$\left(\frac{\beta\cos(\theta)}{\lambda}\right)^2 = \frac{1}{D^2} + \left(\frac{4\varepsilon\sin(\theta)}{\lambda}\right)^2 \quad \textbf{(VII.1)}$$

Where ß = instrumental corrected extension (expressed in radians) θ = angle of diffraction of Bragg, D = crystallite seize (Å), ε = micro strain and λ= wavelength (Å) [7].

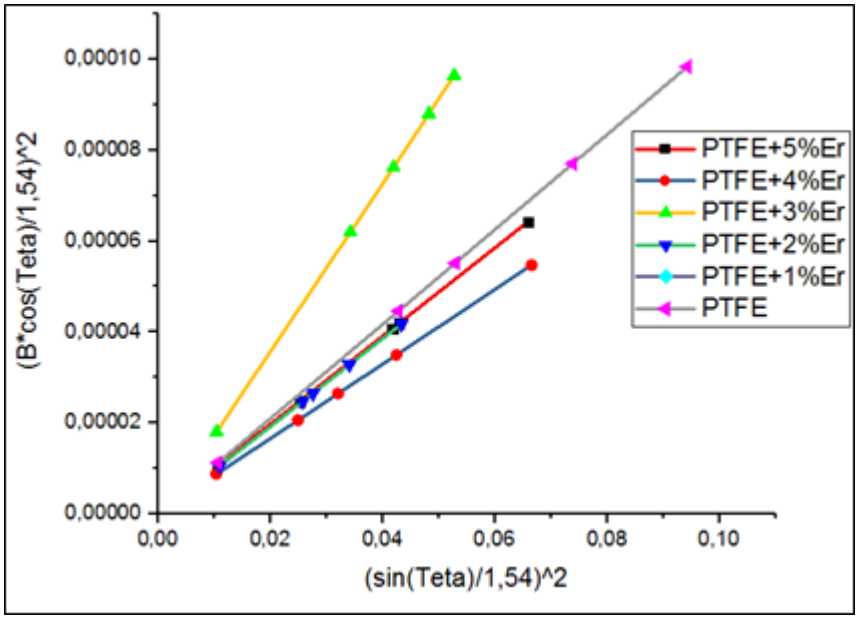

Figure 81:Williamson–Hall plots of $(\beta*\cos\theta/\lambda)^2$ and $(\sin\theta/\lambda)^2$ of PTFE alloys for different deformation percentage of Er.

Table VI. 5:Represent the grain size, micro-strain and volume of Teflon and Teflon doped

Percentage	Grain seize	Microstrain	Volume
PTFE+(0%) d'Erbium	2,1138	0,050369	72,6615
PTFE+(1%) d'Erbium	4,1348	0,047546	327,0475
PTFE+(4%) d'Erbium	4,86325	0,057477	358,794
PTFE+(3%) d'Erbium	3,69735	0,054984	161,8952
PTFE+(4%) d'Erbium	5,32972	0,0485	305,6577
PTFE+(5%) d'Erbium	2,45907	0,050636	305,6577

The figure 82 shows the variation of the grain size, micro-strain and volume of tetrafluoroethylene and tetrafluoroethylene doped by Erbium, according to the percentage. We note for each graph four parts. two parties increase and the others decreases. "parte 1 [0:2%]; parte 2 [2%:3%]; parte 3 [3%:4%]; parte 4 [4%:5%]", We observe that when the volume and the size of the grains increase the micro strain decrease also a high increase of the volume in the parte 4. So we can conclude that the materials are elastic because the properties of the grain form are sensitive to micro strain.

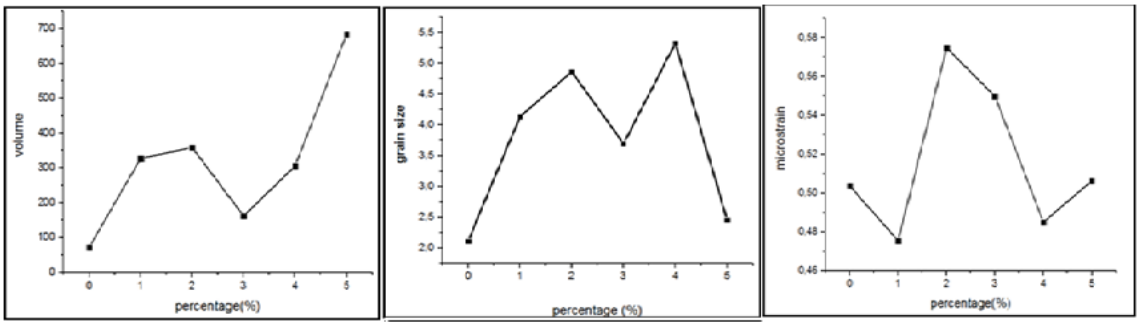

Figure 82:Variation of the grain size, micro-strain and volume of tetrafluoroethylene and tetrafluoroethylene doped by Erbium, according to the percentage

2. 2. Fourier transforms infrared spectroscopy (FTIR)

A Figure 83 shows the FTIR spectra of the pure Teflon and the Teflon doped by erbium. As Shown in Figures relatively strong twin peaks at 1200cm^{-1} and 1125 cm^{-1} corresponding to CF2 asymmetrical stretching and symmetrical stretching modes, respectively, appeared in the absorption spectra of the Teflon doped. Additionally, the weak peak of CF2 wagging mode appeared at 1000 cm^{-1},However, the weak peak of CF3 stretching mode appeared at 981 cm^{-1}, so

the very weak bands present must be due to impurities or surface contamination ,it is the effect the Erbium element. in all spectra of the Teflon and Teflon doped. As summarized in tables VI.6 and VI.7.

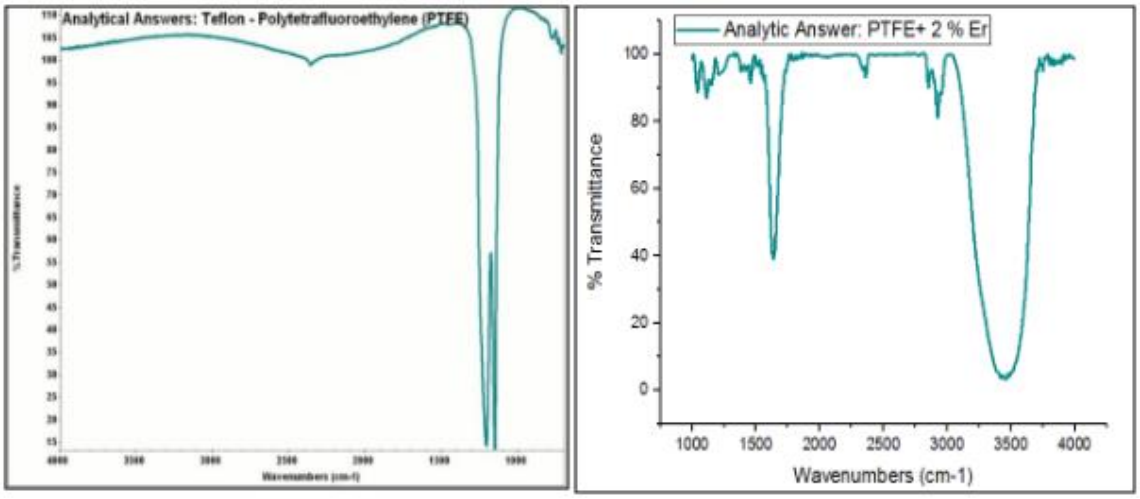

Figure 83:FT-IR Spectra of the Plytetrafluoroethylene and Teflon doped by Erbium (2%)

Table VI. 6:Represent the positions of the spectra with the form and transmittance of the polytetrafluoroethelene

Polytetrafluoroethelene		
Wavenumber (cm^{-1})	**Transmittance (%)**	**Spectral form**
1125	**13**	**delicate**
1200	**14**	**delicate**

Table VI. 7:Represent the positions of the spectra with the form and transmittance of the polytetrafluoroethylene doped by erbium (2%)

Polytetrafluoroethelene+ 2% Erbium		
Wavenumber (cm^{-1})	Transmittance (%)	Spectral form
1043,6616	84,70	delicate
1111,4911	83,85	delicate
1457,0223	88,47	delicate
1639,76	35,43	delicate
2364,34	89,89	delicate
2926,12	77,50	delicate
3460,78	0,25	wide

3. Effect of Gadolinium on microstructural of crystalline morphology

3. 1. Experimental method of elaboration

The Teflon based semiconductor synthesis was prepared by solid state with various percent of Gadolinium us shown in Table VI.8. Samples are placed in alumina burrows after 1 mm grain size burring and placed at 100 °C for 45 min. We have increased the temperature oven at 500°C up to the transition of temperature of Teflon and Teflon doped by Erbium.

Table VI. 8:Teflon and Teflon doped of various Gd percentage

	Masse	
	PTFE on (g)	Gadolinium on (g)
PTFE	1	0
PTFE+Gd (1%)	0,99	0,01
PTFE+Gd (2%)	0,98	0,02
PTFE+Gd (3%)	0,97	0,03
PTFE+Gd (4%)	0,96	0,04
PTFE+Gd (5%)	0,95	0,05

3. 2. Results and Discussion

3. 2. 1. X-Ray Fluorescence (XRF)

This search was led in center of characterization and analysis on every sample of PTFE and PTFE doped on Gadolinium by using the X-ray fluorescence (XRF) which will be analyzed the content of Gadolinium, the result can be seen in the histograms below, which consists essentially of PTFE and of Gadolinium.

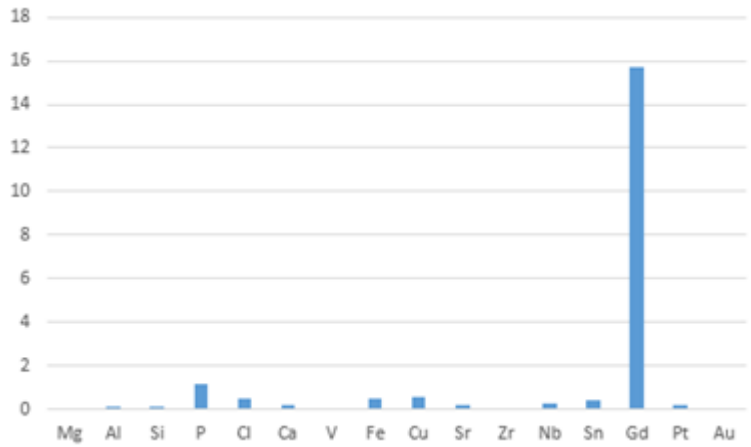

Figure 84:X-ray fluorescence (XRF) PTFE doped on 1% of Gadolinium

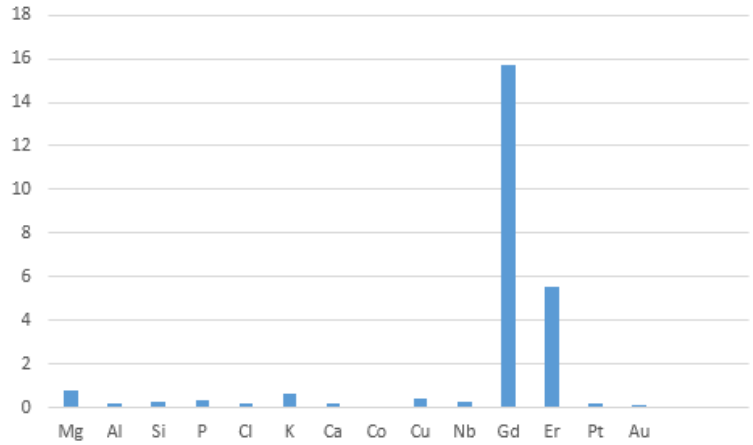

Figure 85:X-ray fluorescence (XRF) PTFE doped on 2% of Gadolinium

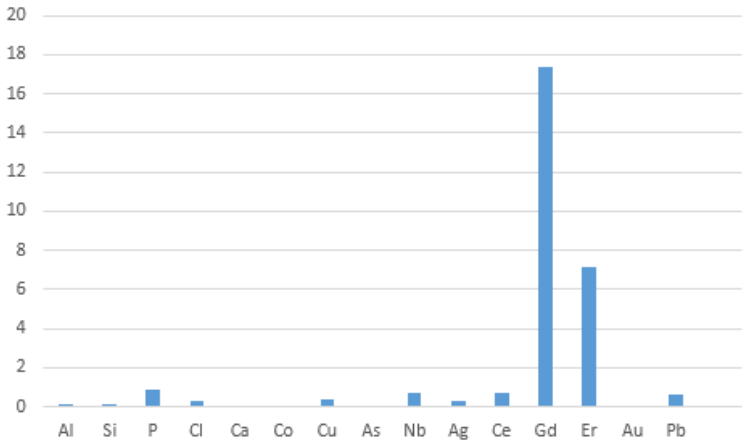

Figure 86:X-ray fluorescence (XRF) PTFE doped on 3% of Gadolinium

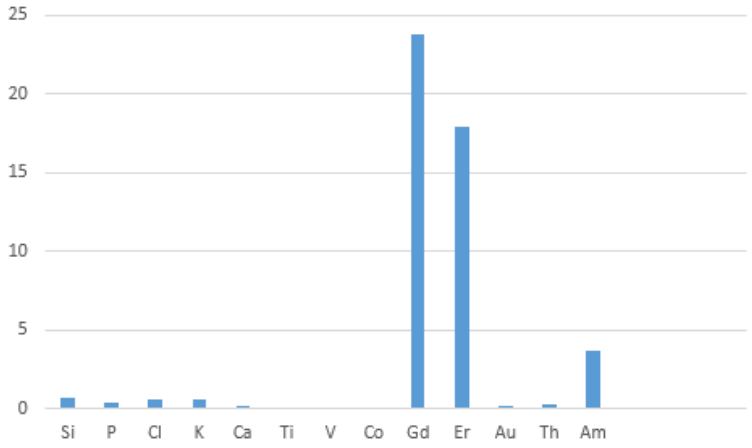

Figure 87:X-ray fluorescence (XRF) PTFE doped on 4% of Gadolinium

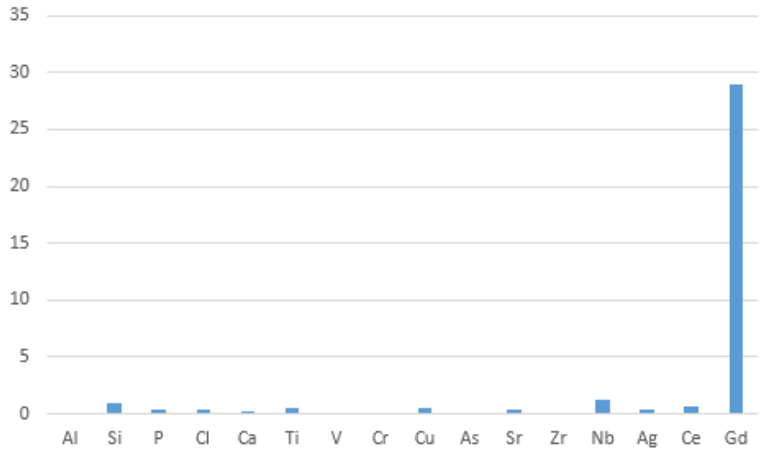

Figure 88:X-ray fluorescence (XRF) PTFE doped on 5% of Gadolinium

3. 2. 2. Fourier Transforms Infrared Spectroscopy (FTIR) of Teflon doped by Gadolinium

Infrared spectra (FTIR) of as-prepared and sintered samples were collected by Perkin-Elmer Spectrum 400 spectrophotometer in 4000 - 450 cm^{-1} range to obtained information about phase composition and bonding in our samples.

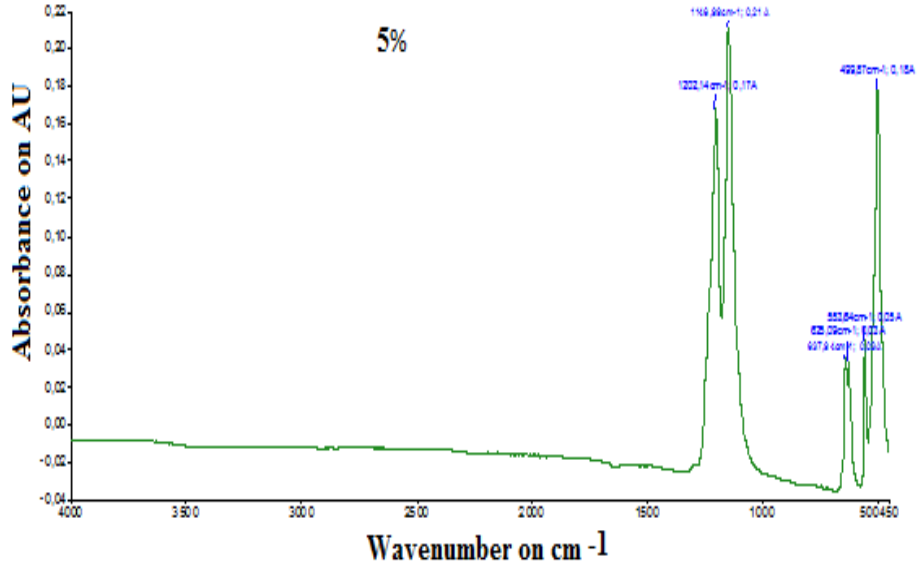

Figure 89:FT-IR spectrum of the Teflon doped by 5% of Gd

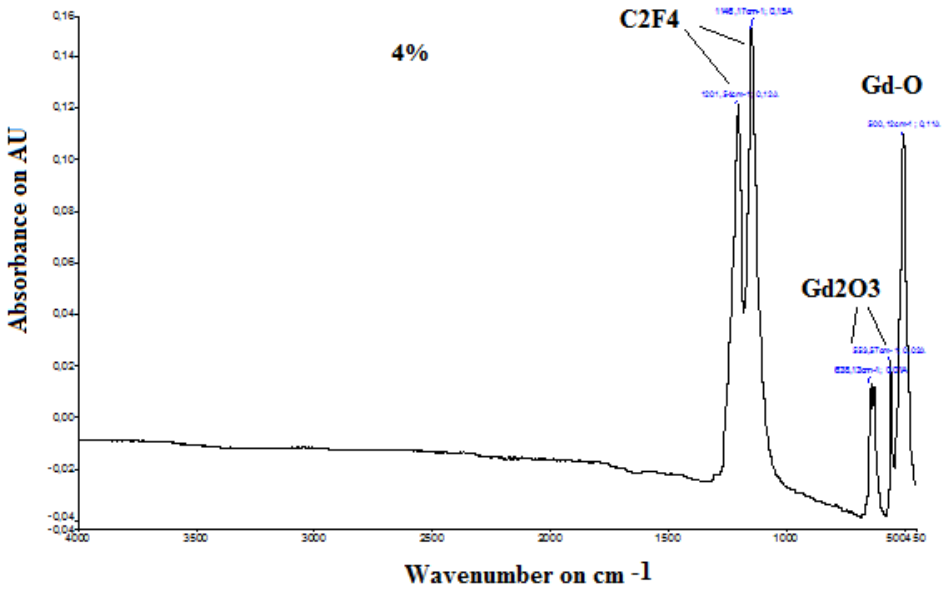

Figure 90:FT-IR spectrum of the Teflon doped by 4% of Gd

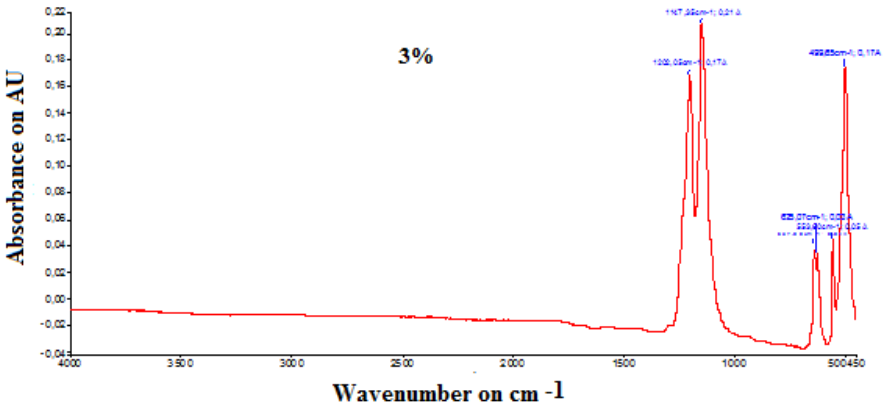

Figure 91:FT-IR spectrum of the Teflon doped by 3% of Gd

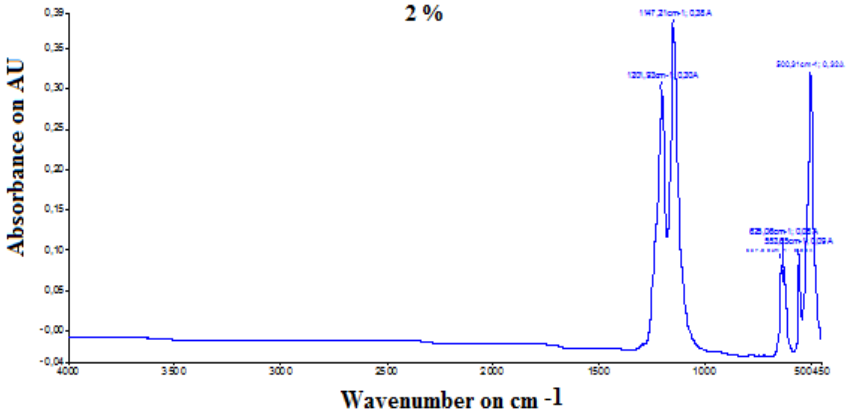

Figure 92:FT-IR spectrum of the Teflon doped by 2% of Gd

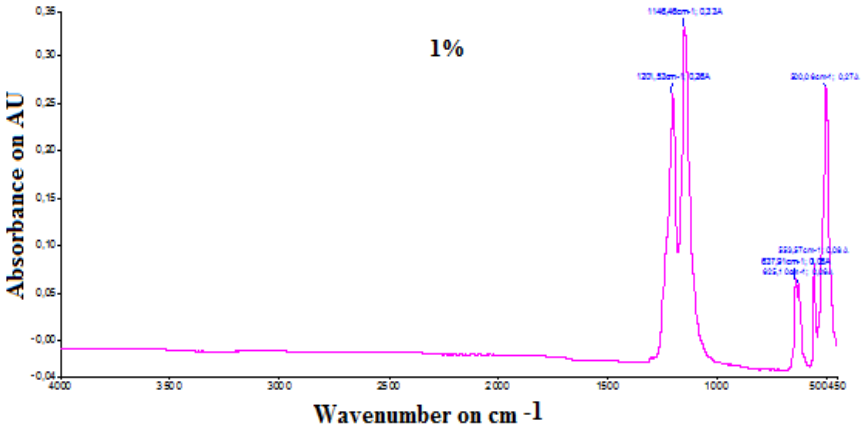

Figure 93:FT-IR spectrum of the Teflon doped by 1% of Gd

The x-axis represents the wave number in cm^{-1} while the ordinate axis is oriented upwards and represents the absorbance. According to the figures above, there are two zones to be analyzed separately: zone 1 can be defined from 500 to 1300cm^{-1} characterized by numerous bands of vibration of deformation while the zone 2 between 1300 and 4000cm^{-1} was characterized by numerous bands of vibration of elongation.

Table VI. 9:Common point visible to all spectrum

Liaison	Nature of vibration	Wave number cm-1	Intensity and form
Gd-O	Elongation	500.12	Strong, fine
Gd2O3	Elongation	638.13	Strong, fine
C2F4	Elongation	1146.17 and 1202.54	Strong, fine

3. 2. 3. Characterization by X-ray diffraction analysis

Teflon-based compounds were characterized by ADVANCE D8 X-ray diffraction showing the most intense peak that indicates the crystallized phase. This means the probability of recovering the obtained phase, as well as the purity of the material. We notice that other peaks appeared. Gadolinium element has an effect on the brain phase due to the intensity of Gd reacting with Teflon. Figure 1 shows the X-ray diffraction spectra of Teflon and Teflon doped by Gd. According to the indexation, we have found that our samples have been crystallized in the orthorhombic system with space group (Pmmm). The effect of Gd on Polytetrafluoroethylene $(C_2F_4)n$, such as grain size, position displacement, and intensity, was studied from 1% to 5% percentages range illustrated in figure 94.

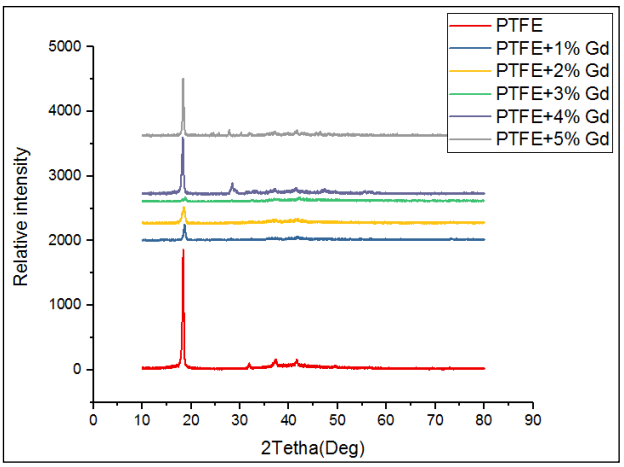

Figure 94:X-ray diffractograms of PTFE and different percentage of doping with Gd:X-ray diffractograms of PTFE and different percentage of doping with Gd

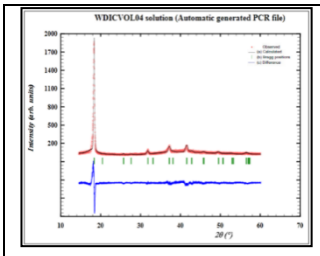

Fig. VI.2.1. Profile Matching with constant scale factor refinements on $(C_2F_4)_n$: experimental, calculated and differential spectra

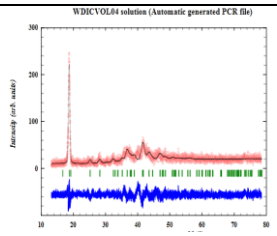

Fig. VI.2.2. Profile Matching with constant scale factor refinements on (C2F4)n at 1%Gd: experimental, calculated and differential spectra

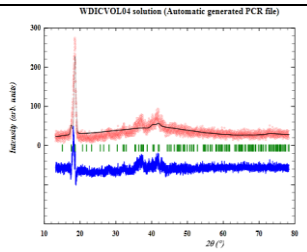

Fig.VI.2 .3.Profile Matching with constant scale factor refinements on $(C_2F_4)_n$ at 2% Gd: experimental, calculated and differential spectra

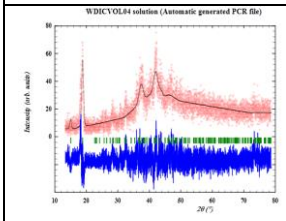

Fig. VI.2.4. Profile Matching with constant scale factor refinements on $(C_2F_4)_n$ 3% Gd: experimental, calculated and differential spectra

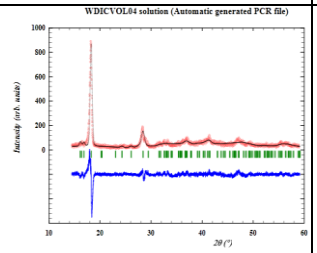

Fig. VI.2.5. Profile Matching with constant scale factor refinements on $(C_2F_4)_n$ 4% Gd: experimental, calculated and differential spectra

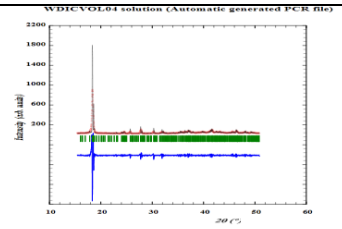

Fig. VI.2.6. Profile Matching with constant scale factor refinements on $(C_2F_4)_n$ 5% Gd: experimental, calculated and differential spectra

Figure 95:X-ray diffractograms of various temperatures of Teflon and Teflon doped

Table VI. 10:Cell parameters extracted from full pattern refinements of various percentage of gadolinium

Percentage	A[Å]	B[Å]	C[Å]	V[Å3]	Space group	Crystal System
PTFE	4.8326	4.3457	3.4599	72.6615	P m m m	Orthorhombic
PTFE+1%Gd	9.4869	5.2933	2.7605	138.6224	P m m m	Orthorhombic
PTFE+2%Gd	8.1654	5.8803	5.0560	242.7665	P m m m	Orthorhombic
PTFE+3%Gd	23.5763	3.8721	3.1514	287.6909	P m m m	Orthorhombic
PTFE+4%Gd	22.0212	5.4484	2.8244	338.8698	P m m m	Orthorhombic

The figure 96 shows the variation of cell parameters of Polytetrafluoroethylene doped by Gd according to the percentage. We observed that parameter A and B were increasing between 0 and 1% while C was decreasing in this interval. Between 1% and 2%, the parameter A decreased but the parameter B continued to increase until 2% then we observed a high decrease between 2% and 3%. These change in parameters A, B and C could be explained by the variations of crystalline structure in ours elaborated samples. The grain size of Teflon doped and the decrease of the parameters of the cell can be bound to the elasticity of the network trained by groupings bound only by summits.

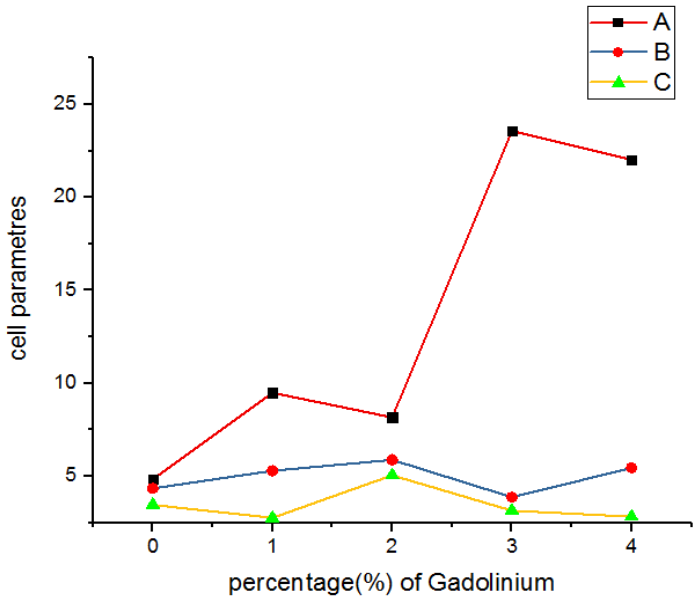

Figure 96:Variation of cell parameters of tetrafluoroethylene and tetrafluoroethylene doped by Gadolinium percentage

- Determination of microstructural parameters

The mechanism of X-rays Diffraction in the crystalline materials is that the X-rays scatter from crystals because their electric fields interact with the clouds of electrons of atoms in crystals. The X-rays scattered from the periodic neighboring atoms interfere and give rise to a plan of diffraction. Therefore, a profile of diffraction line is the result of the convolution of a number of independent variables contributing to the form profile to know the instrumental variables and the microstructural effects. The instrumental variable includes the width of crack of reception,

The transparency of the sample, the nature of the source of X-rays, the axial difference of the incidental beam and the flat sample geometry [5]. The microstructural effects responsible for the profile of shape of the peaks of diffraction are the following ones.

Size finished crystals or domains and micro strain the crystal contains defects of network. These profiles are equipped with functions of shape of adapted profile in a way that the functions asymmetric peaks and it should be so simple mathematically as possible to do the calculation of all the by products have variables

- Crystallite size and micro-strain with William-Hall

There are several methods for calculating the grains size. The most important methods handled are the Debye-Sherrer method and the William hall method. The latter has the advantage that the Debaye-Sherrer method is the double up for both the average grains size and the micro-strain.

To go up the two parameters, it is necessary to adjust the curves which will be linear of W-H with various degrees of distortion. The presence of the crystallites caused the extension of the X-ray line in the polycrystalline material as well as the effect of micro deformations. The slopes of the W-H plane represent the internal mean microstructure. Whereas the opposite of the ordinate at the origin of the axis (β*cos (θ)/λ)2 gives the size of the crystallites according to the relation.

Table VI. 11:Represent the micro-strain, volume and grain size of Teflon and Teflon doped

Percentage	Grain seize	Microstrain	Volume
PTFE+(0%) de Gadolinium	2,1138	0,50369	72,6615
PTFE+(1%) de Gadolinium	1,3380	0,47546	138.6224
PTFE+(2%) de Gadolinium	1,2883	0,57477	242.7665
PTFE+(3%) de Gadolinium	2,0960	0,54984	287.6909
PTFE+(4%) de Gadolinium	2,9320	0,485	338.8698

The figure 97 shows the variation of the grain size, micro-strain and volume of PTFE and doped PTFE by Gd, according to the percentage. We note that in grains size graph, two parts could detected: a decreasing in the range of [0:2%] and an increasing in the range of [2%:5%] while a linearity behavior in the volume graph between volume and percentage of Gd.

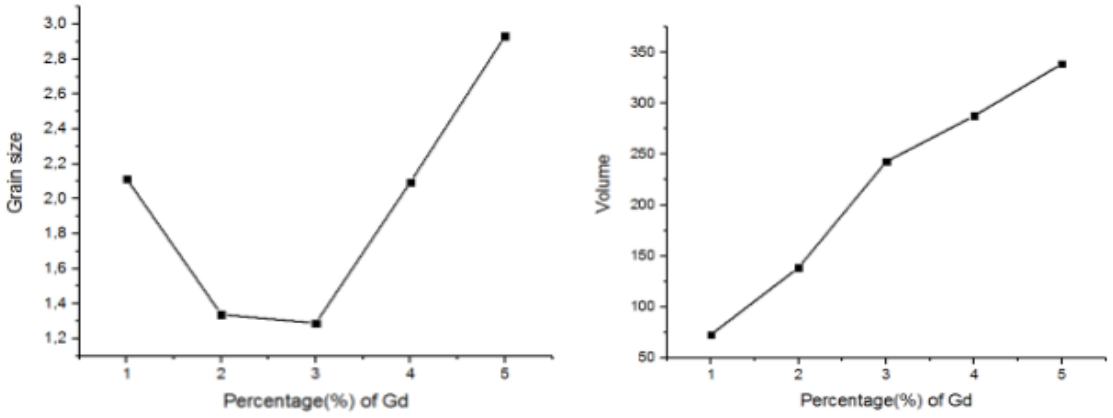

Figure 97:Variation of the grain size and volume of tetrafluoroethylene and tetrafluoroethylene doped by Gadolinium, according to the percentage

CONCLUSION

Teflon and Teflon doped have been studied to measure optical and electrical magnitudes. Various concentrations of Erbium (Er) have given a change in these properties such as gap energy, urbach energy and micro strain. Comparison of the absorbance and the adjusted Teflon Urbach absorption edge and doped Teflon suggests that the extrinsic absorbers may represent a slight increase in absorbance over what might be the intrinsic absorbance of the Teflon polymer. The X-ray diffraction line broadening analysis has been used for measuring the parameters of microstructure of Teflon and Teflon doped. FT-IR spectroscopy is a powerful tool for polymer analysis, and a range of sampling methods are available with varying degrees of sample compatibility and time requirements.

Teflon and Teflon doped have been studied to investigate the effect of the Gadolinium (Gd) on a micro-morphology. The various concentrations of Gd have given a change in these properties such as grain size, Volume of the grains and microstrain. The X-ray diffraction line broadening analysis has been used for measuring the parameters of microstructure of Teflon and Teflon doped. FT-IR spectroscopy is a powerful tool for polymer analysis, and a range of sampling methods are available with varying degrees of sample compatibility and time requirements

References

[1] C. Brabec, Sol. Energy Mater. Sol. Cells 83 (2004) 273.
[2] G. Adamopoulos, Electronic transport properties aspects and structure of polymer-fullerene based organic semiconductors for photovoltaic devices. 511 – 512 (2006) 371 – 376.
[3] L. Ouali, V.V. Krasnikov, U. Stalmach, G. Hadziioannou, Adv. Mater. 11(18) (1999) 1515.
[4] J. Tauc, in Amorphous and Liquid Semiconductors, edited by J. Tauc (Plenum Press, London and New York, (1974).
[5] F. Demichelis, G. Kanidakis, A. Tagliferro, E. Tresso, Appl. Opt. 9 (26) (1987) 1737
[6] A.A. Akl1 and A.S. Hassanien,Microstructure characterization of Al-Mg alloys by X-ray diffraction line profile analysis,International Journal of Advanced Research (2014), Volume 2, Issue 11, 1-9
[7] P. Rama Rao and T.R. Anantharaman;Z. Metallk. Vol. 54 (1963)658.
[8] S. Zanini1, R. Barni1, R. Della Pergola2 and C. Riccardi1»Modification of the PTFE wettability by oxygen plasma treatments: influence of the operating parameters

CHAPTER VII :

COMPARISON BETWEEN TEFLON DOPED BY BOTH ERBIUM AND GADOLINIUM USING XRD

INTRODUCTION

For construct a semi-conductor organic material, using a conductive material including lanthanide elements us Gadolinium oxide and Erbium oxide that are extremely dynamic because of their interesting properties [1,2]; for example: It have a short bandgap, very high absorption coefficients, bonding energy, chemical stability and environmentally friendly applications. And the Teflon with a very high electrical resistivity (transverse volume resistivity> 1018 Ohm.cm) and thermal (maximum operating temperature peak 300 ° C and thermal conductivity 23 ° equal 0.23 W / (Km). Teflon also represents a variety of applications namely Bearings, pads, soles Electrical Insulating Joints, anticorrosion, the protection of cells solar panels [3]. Our aim is to make the material a semiconductor based on organic teflon material for use both for the protection of solar panel cells and the manufacture of photovoltaic cells (solar cells based on organic semiconductors which may be very flexible and easily manufactured by coating and printing techniques [4]. Organic semiconductors have very large advantages among them, a chemical adaptation; they also have flexibility of their other properties. The first demonstration of a photovoltaic effect within an "organic" device dates back to 1958. In this initial example, two materials (magnesium phthalocyanine MgPc and N, N, N ′, N′-tetramethyl-p- phenylenediamine TMPPD oxidized in air), associated in bilayers between two electrodes, produce a photo-current under illumination[5] Subsequently, so-called mono-component solar cells, of the Schottky diode type, were mainly studied[6,7,8] In this type of architecture, the organic semiconductor (SCO) is placed between two electrodes having different outputs, one of which is metallic and the other is transparent, to allow light to pass through. Under illumination, photons are absorbed by organic molecules, going into an excited state and thus generating excitons (electron / hole pairs). These can diffuse within the material and dissociate at the interfaces with the electrodes thus generating a photo-current (Figure VII.1).

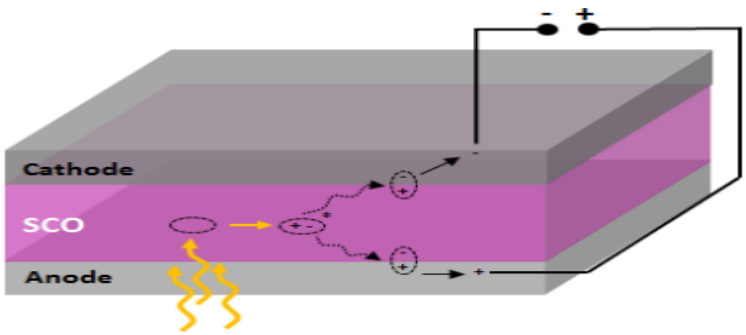

Figure 98:Architecture et fonctionnement d'une cellule de type Schottky[9]

The other examples of these types of solar cells are based on mixtures of poly {[2-methoxy-5 -[(3,7-dimethyloctyl) oxy] phenylene] vinylene} (MDMO-PPV) and 1- [3- (methoxycarbonyl) propyl] -1-phenyl- (6,6) -C61 (PCBM) that has been recently manufactured and extensively studied with power conversion efficiencies up to 3% [10].

In a work by A.El moutarajji et al [11] who doped teflon with Er found clear results to make teflon (PTFE) usable as a semi-conductor, such as the gap energy of doped Teflon reduced from 5.25eV for pure Teflon to 4.75eV for (Teflon + (5%) of Erbium) with a gap reduction of ratio is 10%.

Our main object in this paper is to characterize the structure of materials based on teflon doped with the elements of Gadolinium (Gd) and Erbium (Er). and compare the stricture parameters. in order to ensure the compatibility, use these materials in the semiconductor field.

In this work, polytetrafluoroethylene (PTFE) is doped by a transition element such as Erbium (Er) and Gadolinium (Gd) which are part of the lanthanides. In the following paragraph we will detail the method of development and the X-ray diffraction (DRX) characterization technique of our product to determine the structural parameters.

1. Characterization of Teflon doped by both Erbium and Gadolinium

1. 1. Characterization by X-ray diffraction analysis

Teflon and doped Teflon-based compounds were characterized by an ADVANCE D8 X-ray diffraction device, which gives a curve of the diffraction intesity as a function of (2teta) that shows the most intense peak in the diffraction curve indicates the crystallized phase. Which is the probability of recovering the phase obtained in our materials, as well as the purity of the material. We remark also other peaks appeared. The elements Gadolinium (Gd) and Erbium (Er) have an effect on the brain phase due to the intensity of the reaction of these elements with Teflon. Figure VII.2 shows the X-ray diffraction spectra of Teflon and Teflon doped with Gadolinium and Erbium. According to the indexing, the samples were crystallized in the orthorhombic system with a space group (Pmmm). we also found that the effect of gadolinium and Erbium on tetrafluoroethylene (C_2F_4) n, such as grain size, lattice parameters, position displacement and peak intensity, were studied in a range of percentages from 1% to 5% shown in Figure 99 .

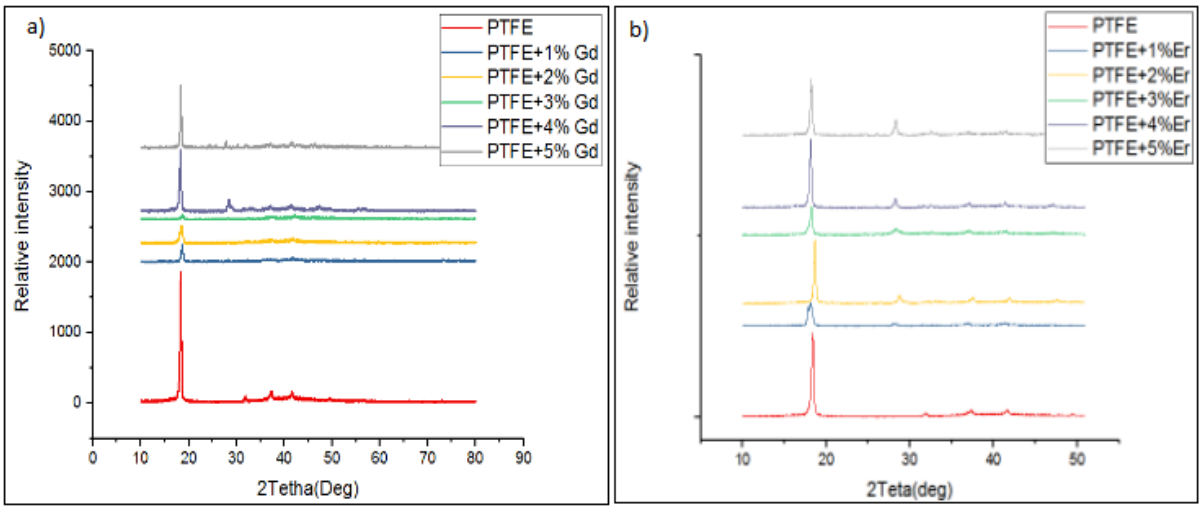

Figure 99:a)X-ray diffractograms of PTFE and Different percentage of doping with Gadolinium and b) X-ray diffractograms of PTFE and Different percentage of doping with Erbium

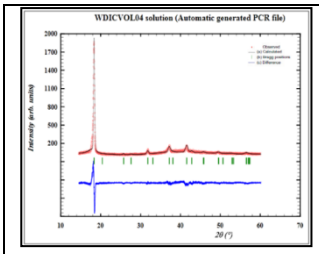

Fig. VII.3.1. Profile Matching with constant scale factor refinements on $(C_2F_4)_n$: experimental, calculated and differential spectra

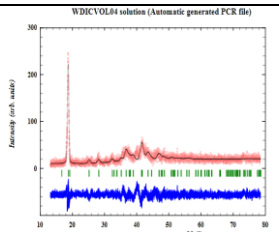

Fig. VII.3.2. Profile Matching with constant scale factor refinements on (C2F4)n at 1%Gd: experimental, calculated and differential spectra

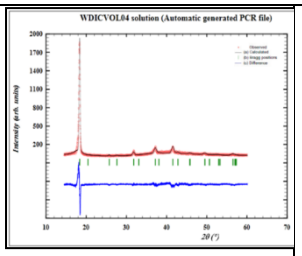

Fig. VII.3.7. Profile Matching with constant scale factor refinements on $(C_2F_4)_n$: experimental, calculated and differential spectra

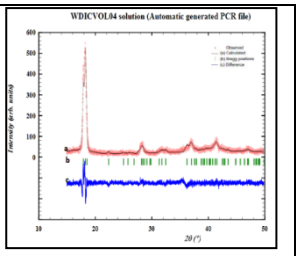

Fig. VII.3.8. Profile Matching with constant scale factor refinements on (C2F4)n at 1%Er: experimental, calculated and differential spectra

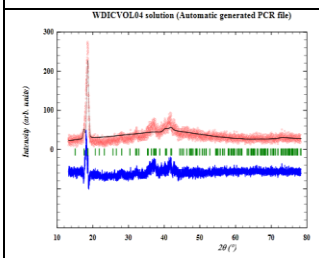

Fig. VII.3.3.Profile Matching with constant scale factor refinements on $(C_2F_4)_n$ at 2% Gd: experimental, calculated and differential spectra

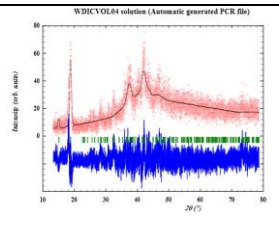

Fig. VII.3.4. Profile Matching with constant scale factor refinements on $(C_2F_4)_n$ 3% Gd: experimental, calculated and differential spectra

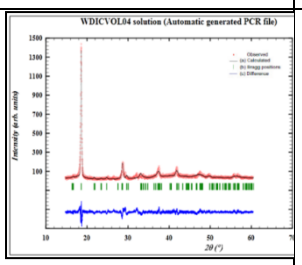

Fig. VII.3.9.Profile Matching with constant scale factor refinements on $(C_2F_4)_n$ at 2%Er: experimental, calculated and differential spectra

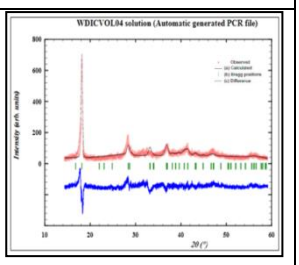

Fig. VII.3.10. Profile Matching with constant scale factor refinements on $(C_2F_4)_n$ 3%Er: experimental, calculated and differential spectra

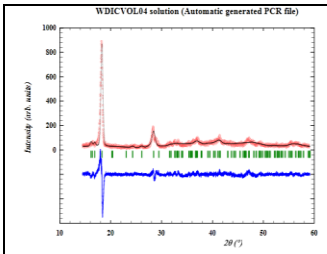

Fig. VII.3.5. Profile Matching with constant scale factor refinements on $(C_2F_4)_n$ 4% Gd: experimental, calculated and differential spectra

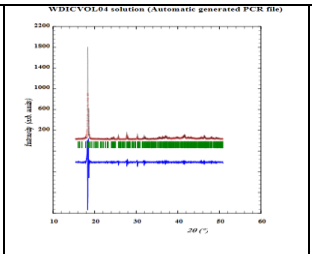

Fig. VII.3.6. Profile Matching with constant scale factor refinements on $(C_2F_4)_n$ 5% Gd: experimental, calculated and differential spectra

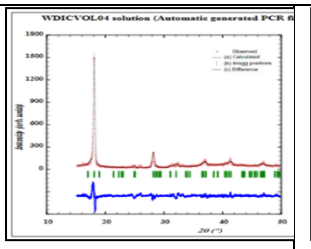

Fig. VII.3.11. Profile Matching with constant scale factor refinements on $(C_2F_4)_n$ 4%Er: experimental, calculated and differential spectra

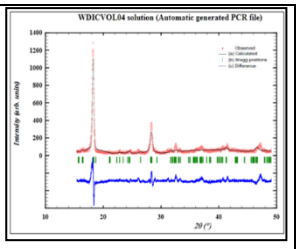

Fig. VII.3.12. Profile Matching with constant scale factor refinements on $(C_2F_4)_n$ 5%Er: experimental, calculated and differential spectra

Figure 100:X-ray Diffractograms of various percent of Teflon and Teflon doped.

Table VII. 1:Cell parameters extracted from full pattern refinements of various percentage of Gadolinium on Teflon and Teflon doped

Temperature	A[Å]	B[Å]	C[Å]	V[Å3]	Space group	Crystal System
PTFE	4.8326	4.3457	3.4599	72.6615	P m m m	Orthorhombic
PTFE+1%Gd	9.4869	5.2933	2.7605	138.6224	P m m m	Orthorhombic
PTFE+2%Gd	8.1654	5.8803	5.0560	242.7665	P m m m	Orthorhombic
PTFE+3%Gd	23.5763	3.8721	3.1514	287.6909	P m m m	Orthorhombic
PTFE+4%Gd	22.0212	5.4484	2.8244	338.8698	P m m m	Orthorhombic
PTFE+5%Gd	####	####	####	####	####	####

Table VII. 2:Cell parameters extracted from full pattern refinements of various percentage of Erbium on Teflon and Teflon doped [11]

Temperature	A[Å]	B[Å]	C[Å]	V[Å^3]	Space group	Crystal System
PTFE	4.8326	4.3457	3.4599	72.6615	P m m m	Orthorhombic
PTFE+1%Er	7.1251	6.9111	6.6416	327.0475	P m m m	Orthorhombic
PTFE+2%Er	10.7686	6.2683	5.3154	358.7940	P m m m	Orthorhombic
PTFE+3%Er	6.2885	5.2723	4.8830	161.8952	P m m m	Orthorhombic
PTFE+4%Er	15.6326	4.9031	3.9878	305.6577	P m m m	Orthorhombic
PTFE+5%Er	18.9923	5.6523	5.6064	601.8480	P m m m	Orthorhombic

The Figure 101 (a) shows the variation of cell parameters of polytetrafluoroethylene material and polytetrafluoroethylene material doped by Gadolinium, according to the percentage. We observe an increase of the cell parameters (a,b) in the range between 0 and 1%, But we remark the decrease

of parameter (c) in the range between this interval then we show a decrease of the parameters (a) between the range from of 1% to 2% then it returns in high increase, but the other parameter (b) continue to increase until the percent 2% then we observe a high decrease of parameters (b,c) between 2% and 3% then the parameters (a,c) finish with an increase.

However, the figure 101 (b) shows the variation of cell parameters of polytetrafluoroethylene doped by Erbium (Er), according to the percentage. We observe an increase of all the parameters (a,b and c) in the range between 0 and 1%, then a decrease of the two parameters (b,c) from of 1% to 4% then returns in increase, but the parameter (a) is clearly continue to increase until the value 2% then we remark a high increase between a range from of 3% to 5%, finally we observe in the two material whether it was Teflon and Teflon doped with Gadolinium or Teflon and Teflon doped with Erbium the parameter (a) greater than (b) and (b) greater than c.

These variations of these parameters can we give some explanation of the crystalline structure of our samples formed. And can be connected with the grain size of Teflon doped, that we go to explain in the paragraph fellow.

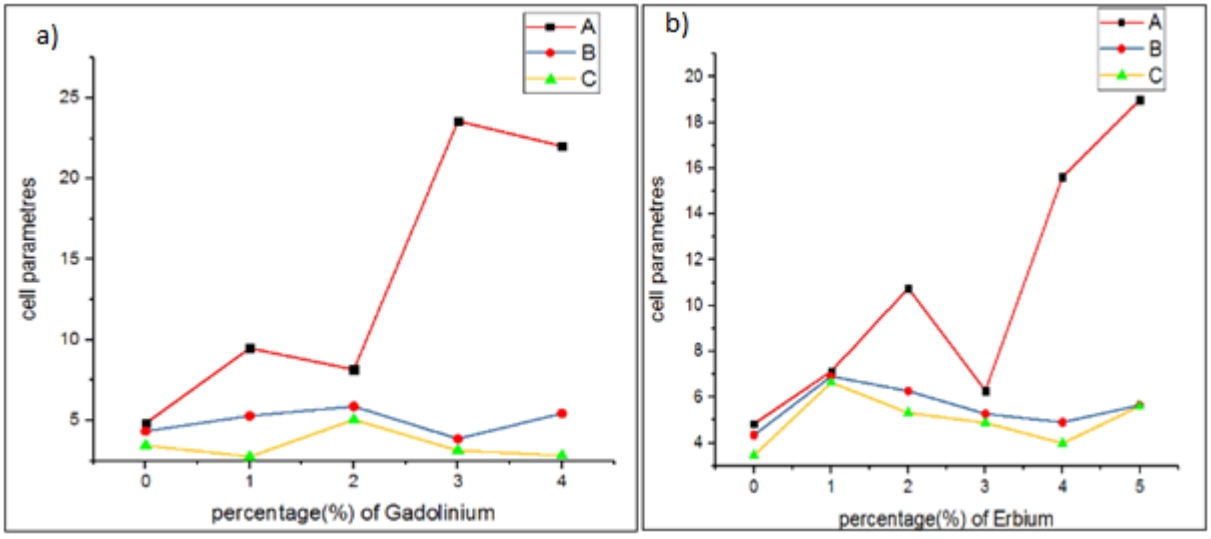

Figure 101:a) Variation of cell parameters of tetrafluoroethylene and tetrafluoroethylene doped by Gadolinium and according to the percentage. b) Variation of cell parameters of tetrafluoroethylene and tetrafluoroethylene doped by Gadoliniumand according to perce

1. 1. 1. Determination of microstructural parameters

The principal mechanism of X-rays Diffraction device in the crystalline materials that is the scatter X-rays from crystals, because there is the interaction of the electric fields with the clouds of electrons of atoms in crystals. The scattered of X-rays from the periodic neighboring atoms of sample interfere and give a to plan of diffraction. This plan of diffraction can be modulated with

the function transfer of the detector, which has the role of modifying the shape of the X-ray diffraction profile. So, the result of the convolution represented by a diffraction line profile, of a number of independent variables contributing to this shape profile to give knowledge of the instrumental variables and the microstructural effects. this instrumental variable includes the width of the receiving crack,

The transparency sample, the nature X-rays source, the axial of the incidental beam and finally the flat sample geometry the microstructural effects responsible for the profile of shape of the peaks of diffraction are the following ones.

1. 1. 2. Crystallite size and microstrain with Wiliam-Hall

There are several methods can we use to calculate the grains size, the most famouse methods are the Debye-Sherrer method and the William hall method. the latter method has the advantage that the Debaye-Sherrer method, because the William hall methode have the double up for both, the micro-strain and the average grains size.

To go up these two parameters it is necessary to make adjust the curves, which will be laniary of W-H with various degrees (2teta) of distortion. The presence of crystallites caused the extension of the X line in the crystalline material as well as the effect of micro deformations. The slopes of W-H represent the average internal microstructure. While the size of the crystallites is given by the opposite of the y-intercept of the object $(\beta * \cos(\theta) / \lambda)^2$ as a function of the relation.

Crystallite size and microstrain with Wiliam-Hall

“From the linear adjustment of curves W-H in various degrees of distortion, was confirmed that the extension of the line of the X-rays in the polycrystalline material is due to the presence of crystallites (effect of size) as well as the micro strain effect. The slopes of the plan W-H represent the internal average microstructure. While the opposite of the orderly at the origin of the axis $(\beta*\cos(\theta)/\lambda)2$ give the size of cristallites according to the relation. While the opposite of the orderly at the origin of the axis gives the size of cristallites according to the relation.

$$\left(\frac{\beta\cos(\theta)}{\lambda}\right)^2 = \frac{1}{D^2} + \left(\frac{4\varepsilon\sin(\theta)}{\lambda}\right)^2 \qquad (1)$$

Where ß = instrumental corrected extension (expressed in radians) θ = angle of diffraction of Bragg, D = crystallite seize (Å), ε = micro-trainés and λ= wavelength (Å) [7].” [11]

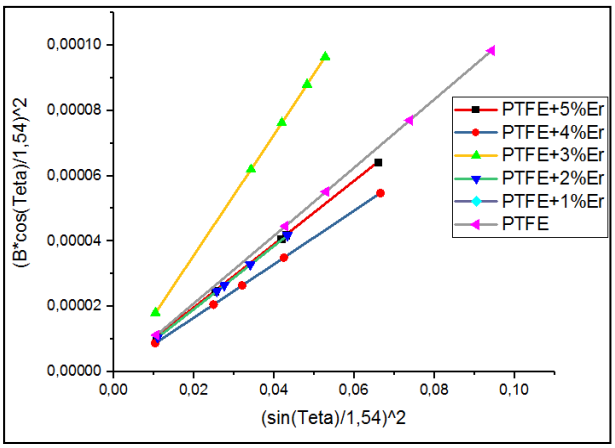

Figure 102:Williamson–Hall plots of $(\beta \cos\theta/\lambda)^2$ and $(\sin\theta / \lambda)^2$ of PTFE alloys for different deformation percentage of Er [11]

Table VII. 3:Represent the grain size, micro-strain and volume of the teflon and teflon doped with Gadolinium

Percentage	Grain seize	Micro-strain	Volume
PTFE+(0%) de Gadolinium	2,1138	####	72,6615
PTFE+(1%) de Gadolinium	1,3380	####	138.6224
PTFE+(2%) de Gadolinium	1,2883	####	242.7665
PTFE+(3%) de Gadolinium	2,0960	####	287.6909
PTFE+(4%) de Gadolinium	2,9320	####	338.8698

Table VII. 4:Represent the Grain size, micro-strain and volume of Teflon and Teflon doped with Erbium [11]

Percentage	Grain seize	Micro-strain	Volume
PTFE+(0%) d’ Erbium	2,1138	0,50369	72,6615
PTFE+(1%) d’ Erbium	4,1348	0,47546	327,0475
PTFE+(4%) d’ Erbium	4,86325	0,57477	358,794
PTFE+(3%) d’ Erbium	3,69735	0,54984	161,8952
PTFE+(4%) d’ Erbium	5,32972	0,485	305,6577
PTFE+(5%) d’ Erbium	2,45907	0,50636	305,6577

2. Comparison, results and discussions

The Figure 103 (a) shows the variation of the grain size of polytetrafluoroethylene and polytetrafluoroethylene doped by Gadolinium, according to the percentage. We can note for grains size graph two parts, one of these parts decreases in the range [0 to 2%] and the other an increase in the range [2% to 4%]. And we remark also the crystallite size value included between 1,2nm and 3nm. While the Figure 103 (b) shows the variation of the grain size of polytetrafluoroethylene and polytetrafluoroethylene doped by Erbium shows the opposite and the crystallite size value included between 2nm and 5.5nm.

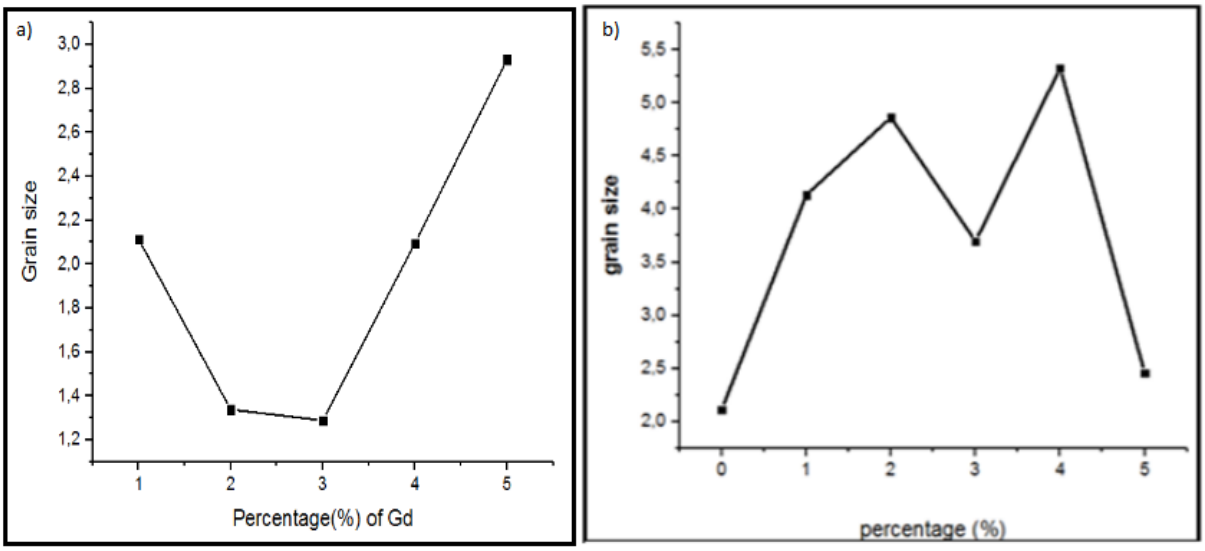

Figure 103 :a)Variation of the grain size on (nm) of tetrafluoroethylene and tetrafluoroethylene doped by Gadolinium, according to the percentage : b)Variation of the grain size on (nm) of tetrafluoroethylene and tetrafluoroethylene doped by Er, according to the percentage

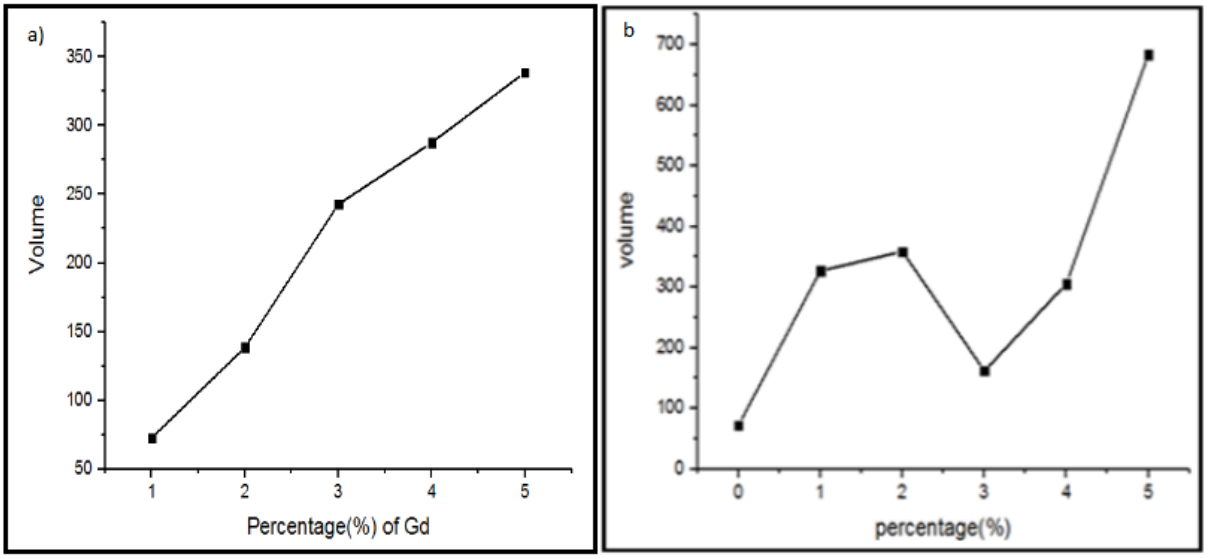

Figure 104:a) Variation of the volume of tetrafluoroethylene and tetrafluoroethylene doped by Gadolinium , according to the percentage :b) Variation of the volume of tetrafluoroethylene and tetrafluoroethylene doped by Erbium , according to the percentage

CONCLUSION

Teflon and teflon doped have been studied for show the effect of the the Gadolinium and Erbium on a micro-morphology. The various concentrations of Gadolinium (Gd) and various concentration of Erbium (Er) have given a change in these properties, such as grain size, volume of the grains and microstrain. The X-ray diffraction line broadening analysis has been used for measuring the parameters of microstructure of Teflon and Teflon doped. So we have already done the UV-visible characterization of Teflon doped with Erbium that we talked about in this paper, we still have to do the UV-visible characterization for the Teflon doped by Gadolinium

References

[1] X. Zhou, W. Huebner. Microstructure and Grain-Boundary Effect on Electrical Properties of Gadolinium-Doped Ceria. 10.1111/j.1151-2916.2002.tb00349.x.

[2] S. Roy, D.Das, T.K.Roy. Influence of sintering temperature on microstructure and electrical properties of Er2O3 added ZnO-V2O5-MnO2-Nb2O5 varistor ceramics. 10.1016/j.jallcom.2018.03.302.

[3] C. Brabec, Sol. Energy Mater. Sol. Cells 83 (2004) 273.

[4] G. Adamopoulos, Electronic transport properties aspects and structure of polymer-fullerene based organic semiconductors for photovoltaic devices. 511 – 512 (2006) 371 – 376.

[5] Kearns, D.; Calvin, M., Chem Phys. 1958, 29, 950-951

[6] G. A. Chamberlain, Sol Cells, 1983, 8, 47-83.

[7] D. Wöhrle, D. Meissner, Adv Mater, 1991, 3, 129-138.

[8] Peumans, P.; Yakimov, A.; Forrest, S. R. J Appl Phys 2003, 93, 3693.

[9] Antoine Labrunie. Matériaux “ uniques ” pour cellules solaires organiques mono-composant. Chimie organique. Université d’Angers, 2017. Français. ffNNT : 2017ANGE0044ff. fftel-01794537f

[10] L. Ouali, V.V. Krasnikov, U. Stalmach, G. Hadziioannou, Adv. Mater. 11(18) (1999) 1515.

[11] A. El Moutarajji, B. Tbib, and Khalil El-Hami. Effect of Erbium Addition on Optical and Electrical Properties of Polytetrafluoroethylene. AI2SD 2018, AISC 912, pp. 97–110, 2019. https://doi.org/10.1007/978-3-030-12065-8_10

GENERAL CONCLUSION

The work presented in this thesis focuses on the synthesis and thermal and rheological characterizations of a type of nanofluid that has never been studied to our knowledge on the whole method of synthesis of silver nanoparticles: The Silver/Glycerol nanofluid. The characterization is made as a function of the solid volume fraction of the nanoparticles in suspension and of the temperature.

This work required the synthesis of nanoparticles and nanofluids by an appropriate method, the design and production of a thermal characterization device using the hot wire method and finally the rheological and thermal characterization of these samples.

We synthesized silver nanoparticles (Ag) 15nm in diameter by microwave irradiation from the silver nitrate salt and in a humid medium which is Ethanol. The size and the dispersion of the nanoparticles thus obtained were controlled using appropriate surfactants (latex). We used these nanoparticles to prepare the Silver/Glycerol nanofluids studied in this work.

The experimental study of the effect of nanoparticles of silver (Ag) on the viscosity of glycerol shows that at the low volume fractions that we tested, the behavior of viscosity as a function of temperature is dominated by Glycerol. the decrease in viscosity with the volume fraction originates from the size of the nanoparticles as the polymer used.

We have observed that the concentration and the size of the nanoparticles are key parameters of the behavior of the effective thermal conductivity of the Ag/Glycerol nanofluid. Our measurements allowed us to deduce the predominance of modifications of the surface of nanoparticles on Brownian motion in nanoparticle/host fluid heat transfers. We suggested proposed a model of effective thermal conductivity inspired by the work of Bruggmen.

On the other hand, good stability of the mixture makes it possible to avoid the agglomeration of particles and thus to maintain homogeneous thermal properties. The results obtained with this new material are interesting because the increase in thermal conductivity reaches significant values. These results are completely comparable with those obtained for certain nanofluids based on carbon nanotubes.

We propose to continue this work carried out at the macroscopic scale by a study at the molecular scale of the influence of nanoparticles on the dynamics of the molecules of the host fluid. Since

Glycerol is a model liquid for the study of glass transitions, it seems interesting to study the influence of nanoparticles on this type of transition.

Finally, we are developing a device for the absolute characterization of the exchanges between a nanofluid and a solid wall, based on the quasi-transient method applied hot wire method.

The doped Teflon and Teflon have been studied to show the effect of Gadolinium and Erbium on a micro-morphology. the various concentrations of gadolinium (Gd) and various concentrations of erbium (Er) gave a change in these properties, such as grain size, grain volume and microstrain. X-ray diffraction line broadening analysis was used to measure Teflon and doped Teflon microstructure parameters. We have therefore already carried out the UV-visible characterization of Teflon doped with Erbium which we spoke about in this paragraph, it remains for us to do the UV-visible characterization of Teflon doped with Gadolinium to have a good comparison.

On the other hand, we worked on doping with low fraction, the results of the gap energy were weakly reduced, because the desired gap energy is of the order of 2eV.

To know more information of electrical behavior it is necessary to work in large fractions such as 1%, 2%, 3%, 4% and 5% to be 10% up to 20%.